David Taylor Research Center

Bethesda, MD 20084–5000

AD-A235 638

Fracture Behavior of Ultra-Low-Carbon Steel Plate and Heat-Affected-Zone

by
M. G. Vassilaros

DTIC
ELECTE
MAY 23 1991
S
B
D

91-00276

91 5 21 074

MAJOR DTRC-TECHNICAL COMPONENTS

CODE 011   DIRECTOR OF TECHNOLOGY, PLANS AND ASSESSMENT

       12   SHIP SYSTEMS INTEGRATION DEPARTMENT

       14   SHIP ELECTROMAGNETIC SIGNATURES DEPARTMENT

       15   SHIP HYDROMECHANICS DEPARTMENT

       16   AVIATION DEPARTMENT

       17   SHIP STRUCTURES AND PROTECTION DEPARTMENT

       18   COMPUTATION, MATHEMATICS & LOGISTICS DEPARTMENT

       19   SHIP ACOUSTICS DEPARTMENT

       27   PROPULSION AND AUXILIARY SYSTEMS DEPARTMENT

       28   SHIP MATERIALS ENGINEERING DEPARTMENT

DTRC ISSUES THREE TYPES OF REPORTS:

1. **DTRC reports, a formal series,** contain information of permanent technical value. They carry a consecutive numerical identification regardless of their classification or the originating department.

2. **Departmental reports, a semiformal series,** contain information of a preliminary, temporary. or proprietary nature or of limited interest or significance. They carry a departmental alphanumerical identification.

3. **Technical memoranda, an informal series,** contain technical documentation of limited use and interest. They are primarily working papers intended for internal use. They carry an identifying number which indicates their type and the numerical code of the originating department. Any distribution outside DTRC must be approved by the head of the originating department on a case-by-case basis.

David Taylor Research Center

Fracture Behavior of Ultra-Low-Carbon Steel Plate and Heat-Affected-Zone

by

M. G. Vassilaros

CONTENTS

FIGURES

TABLES

ABBREVIATIONS

a	crack length
C_o	carbide thickness
d	grain diameter
DBTT	ductile-to-brittle transition temperature
E'	effective mode
EDS	energy dispersive spectrometer
G	strain energy release rate
k	Hall-Petch parameter
K	stress intensity parameter
M	bending moment
M-A	martensite-austenite
Q	stress multiplication factor
r	radius of carbide
R	stress intensity ratio
RKR	Ritchie-Knott-Rice
γ_c	surface energy of carbide
γ_e	effective surface energy
γ_f	surface energy of ferrite
T_i	internal shear stress, lattice friction stress
T_y	shear yield stress
ULCB	ultra-low-carbon bainitic
σ_f	cleavage fracture stress
σ_y	tensile yield stress
θ	included notch angle

ABSTRACT

This report describes research carried out to investigate the fracture behavior of ultra-low-carbon bainitic steels. Eight materials have been evaluated using notched-bar bend tests, tensile tests and Charpy V-notch impact tests, which were performed over a range of temperatures from $-196°C$ to $+100°C$. These tests measured the cleavage fracture strength and the ductile-to-brittle transition temperature (DBTT) under impact loading. The materials evaluated had carbon levels of less than 0.03%, manganese level from 1 to 2%, and microalloying additions of niobium, titanium and boron. Some alloys also contained molybdenum and nickel. Some of the materials were subjected to simulated heat-affected-zone (HAZ) thermal cycle and other thermal- mechanical treatments. The fracture surfaces of the specimens were examined using the scanning electron microscope (SEM) and energy dispersive x-ray analysis. The results of the fracture tests and analyses indicate that the cleavage fracture strength of these materials can vary from 1650 to 2300 MPa. High cleavage fracture strength may be achieved with either a polygonal ferrite or an acicular/bainitic structure, but the high cleavage fracture strength of the polygonal ferrite structure material was reduced as a result of a simulated thermal HAZ cycle. The materials with high cleavage fracture strengths are characterized by a low DBTT, fracture surfaces with small quasi-cleavage facets, and no observable (in SEM) initiation sites. Materials with low cleavage fracture strengths are characterized by high DBTT, fracture surfaces with larger quasicleavage facets, and initiation sites associated with titanium nitride (TiN) cubes. Although these cubes appear to be present in both the low and high toughness materials, they are active initiation sites only in the low toughness material. The nature of the relationship between the low cleavage strength and the TiN cubes at the initiation sites is not understood and requires more investigation to characterize.

ADMINISTRATIVE INFORMATION

INTRODUCTION

The steels used in ship construction must have certain properties which are necessary for the integrity and durability of the ship. Second only to strength, the fracture toughness of the construction steel is of utmost importance, especially when considering combatant vessels. Such steels not only need to be strong enough to support the loads generated by the weight and movement of the ship but must continue to function after large amounts of deformation These properties have been needed since the mid-19th century with the armor-clad ships of the American Civil War (1). Such plates fastened with rivets were used up to the time of the World War II. At that time the riveting technique was being replaced with new welding processes for ship construction [1]. The utilization of these new fabrication techniques allowed ships to be produced more eco-

nomically with improved integrity. The initial application of such technology produced mixed results, the most notorious of which was the failures of the "Liberty Ships" [1]. These assembly-line constructed ships were welded with poor attention to structural details using steel of poor toughness. Of the more than 2500 Liberty ships built, 408 had very large cracks in their hulls which were not the results of adverse conditions but, rather, normal operating conditions [1]. The application of welding technology to the construction of combatant ships was performed with greater caution, which prevented a repetition of the Liberty Ship problems. This was accomplished by modifying the steels and adjusting the welding techniques. The best example of improved steel with high strength is HY–80 [2]. This steel was developed from a late nineteenth century German armor steel developed by the Krupp Company. The steel chemistry was modified to mitigate the loss of toughness in the weld-heat-affected zone. The welding process was restricted to the use of low hydrogen (non-cellulose) electrodes and a minimum preheat of 250°F (121°C) to reduce the level of hydrogen in the weld. Additionally, the heat input rate was initially limited to 55 kJ/in (22 kJ/cm) in order to assure the retention of the martensitic microstructure [3, 4]. These changes restricted the use of this steel to critical applications only, because of the high welding cost involved.

Although HY–80 steel has been used for critical application since the mid-1950's the alloy is not universally accepted as being totally weldable. When Litton Industries was contracted by the U.S. Navy to build a new class of surface ships using steel with a yield strength of 80 ksi (560 MPa) it was suggested that HY–80 not be used due to the high construction cost. The steel that was accepted by the U.S. Navy for use in place of HY–80 for non-critical applications was a modified ASTM Grade A710 steel. This steel was designated HSLA–80 by the U.S. Navy [5]. The steel was originally developed as a line pipe fitting steel by International Nickel Company and was called IN 787. It is a low carbon-manganese steel strengthened with a fine precipitate of copper in a ferrite matrix [6]. The steel is weldable without the need for any preheat and has toughness comparable to that of HY–80. This steel was not developed as a modified version of a pre-existing steel as was HY–80 but was the result of the application of modern metallurgical principles and the up-to-date steel making techniques of the 1970's. The U.S. Navy's acceptance of IN 787 as a new ship construction steel has kindled an increase in research of steel metallurgy. The goal of this new research is to apply the latest in steelmaking technology and metallurgical understanding to develop steels which are optimized for strength, toughness, and weldability.

The purpose of this research is to investigate some of these modern steels and try to understand the metallurgical interactions which control the strength, toughness and weldability. The ultimate goal of the overall research program, of which this investigation is part, is to aid the development and production of high strength, weldable steel with superior fracture toughness while keeping the steel production and ship fabrication costs to a minimum.

BACKGROUND

LOW CARBON STEEL

The primary considerations for a structural steel used in ship construction are listed as follows:

1. High strength – in the range of 65 to 100 ksi (450 to 700 MPa);

2. Toughness: ductile-to-brittle transition temperatures should be very low (below the lowest assumed service temperature);

3. Weldability: should be weldable without preheat and with minimal loss of properties in the heat-affected-zone (HAZ);

4. Cost: Should not exceed the current price of HY–80 steel.

This range of required properties is not easily achieved in commercial steels, especially in light of the required plate thicknesses of over 1-inch (>25 mm). The indicated strength range cannot be easily produced with polygonal ferrite steels. However, structures of bainite or quenched and tempered (Q+T) martensite can be produced with such strength level. The Q+T martensite structure, as in HY–80 steel, has two inherent drawbacks. First, the cooling rates needed to produce martensite in the heat affected zone (HAZ) of the weld would usually limit the maximum heat input to about 55 kJ/in. (22kJ/cm) [3], which is below the 60 to 150 KJ/in (24–60 kJ/cm) range of normal industrial practice. The second drawback to Q+T steel is the added cost resulting from the thermal energy needed to quench and temper. One approach is that the plate material should have a bainite structure which resulted from air cooling. The focus of this research is to investigate such material; to understand the factors that control the fracture toughness of bainitic steel.

In 1965, Irvine and Pickering [7] published the results of their research on high carbon bainitic steels. The composition of the steels ranged from 0.10 to 1.06% carbon with 0.5% molybdenum and some boron. The structures were all produced by air cooling and had strengths in the range of 60 to 150 ksi (400 to 1000 MPa) yield strength. The authors were able to identify two forms of bainite; "upper bainite", which had carbon rejected between the bainite lathes, and "lower bainite", which had carbon precipitated within the lath structure. The austenite to bainite transformation temperature was controlled by the chemical composition of the steel which in turn controlled the strength (Fig. 1). These air cooled structures were mainly the result of the use of boron as an alloying element. Boron is extremely effective in increasing hardenability by suppressing the nucleation of polygonal ferrite. This effect on the transformation kinetics of steel is shown in Fig. 2. This alloying addition, however, has experienced minimal use since its commercial introduction in 1938 at the Wisconsin Steel Works.

A study by Irani and Tither [8] investigated steels with carbon levels from 0.03 to 0.095% carbon. These steels were quenched to produce bainite or (when the carbon was low) acicular ferrite. The steels had yield strength levels in the range of 40 to 80 ksi (280 to 560 MPa). The acicular ferrite structure had impact toughness properties which were superior to those of the bainitic structures. This study verified some earlier work by Irvine and Pickering [9] which had shown that low-carbon lower bainite had improved impact toughness transition (ITT) temperature compared with the low carbon upper bainites (Fig. 3). It also appears that the distinction between low carbon lower bainite and acicular ferrite is not clear.

During this same period of time, work by McEvily and co-workers [10, 11] at Ford Research Laboratory produced an alloy which was both air cooled and low in carbon, with an acicular/bainitic structure. The alloy was composed of 0.03–C, 3Mo, 3–Ni, 0.7–Mn, 0.3–Si, and 0.5–Nb and had a yield strength of over 100 ksi (700 MPa) with ex-

cellent low temperature impact toughness (Fig. 4). McEvily and co-workers, in order to increase hardenability, substituted significant alloying additions instead of the small boron additions of the Irvine and Pickering work [7]. The Ford alloy also had very low carbon to improve resistance to cleavage cracking. This effect was also reported in the previous work of other investigators [7, 8]. The toughness of this alloy was significantly enhanced with the addition of nickel.

Nickel is one of a few alloying additions which has the effect of increasing strength and lowering the impact toughness transition (ITT) temperature as reported by Gensamer [12] in 1959. He reported that a 3.4% addition to low carbon iron could lower the ITT temperature by approximately 60°F (33°C). This effect was reported to be the result of alloy softening (reduction in yield strength) at low temperature. Later, in 1968, Jolley [13] reported a similar effect of 3.28% Ni in low carbon iron and concluded that the improvement in low temperature fracture properties was due to a change in slip behavior and a reduced strain rate effect on low temperature strength. In a larger study, Leslie and coworkers[14] reported the results of the effects of the alloying additions Ni, Cr, Mn, and Si on the impact toughness of low-carbon iron. Their study concluded that only Ni clearly improved strength and impact toughness. The lower ITT temperature obtained with nickel additions was believed to be the result of enhanced cross slip at low temperatures making cleavage propagation difficult, and that alloy softening was not a significant factor. Further studies by Floreen and co-workers[15], Norstrom and Vingsbo [16] and Hilderbrandt and Dickenscheid [17] investigated the effect of nickel on the ITT temperature of low-carbon steel, with similar findings. Hilderbrandt and Dickenscheid concluded that nickel modifies the lattice structure, increasing the number of active slip planes at the lower temperatures. This effect produces more ductility, alloy softening, and less strain rate dependence at low temperatures.

Although the properties of the Ford alloy developed by McEvily and co-workers were very impressive even by today's standards, the alloy was expensive and difficult to produce. The expense resulted from the 6% of Ni and Mo present which are very costly alloy additions. The difficulty resulted from the very low carbon level needed for good toughness, namely 0.03%. This level was very difficult for steel mills of the 1970's to achieve. Otherwise the alloy fulfilled all the requirements of a modern ship construction steel. It exceeded strength goals with a very low ITT temperature, and with the low carbon level (0.03%) good weldability is expected. This good weldability is suggested from the results of the Graville [18] investigation of cold cracking susceptibility in HSLA (high strength low alloy) steels. These results indicated that all of the carbon equivalent (CE) equations, based on alloy hardenability and used to measure the base plate resistance to hydrogen cracking from welding, may be meaningless for alloys with less than 0.10% carbon. These low carbon alloys were all resistant to cold cracking regardless of the value of the CE equation as shown in Fig. 5. Therefore the idea of a low carbon acicular/bainitic air cooled steel was still attractive and only needed a more economical alloy system.

Another approach to this alloy design was being reported by investigators at the Climax Molybdenum Laboratory. This work by Smith, Coldren, Cryderman and Semchyshen[19, 20, 21] was to develop a new high toughness, weldable alloy for use in high strength pipelines. The investigation was conducted with available steel making practice in mind. The results of their work produced a steel with a composition of

0.5%–C, 1.6%–Mn, 0.25%–Mo, and 0.05%–Nb, which is one of a family of low–carbon manganese-molybdenum-niobium steels. The commercial spray–cooled heat of this steel produced a yield strength of 70 ksi (490 MPa) with a Charpy V-notch ITT of –76°F (–60°C).

The design philosophy used for this alloy required that the steel be low carbon with a nearly 100% acicular ferrite structure, allowing for some fine ferrite. Since the final plate thickness required was 1/2 inch (13mm), spray cooling could be employed to reduce the transformation temperature, rather than alloying alone. Although other alloy systems which used boron to replace some of the molybdenum and manganese were investigated, [19] the alloy containing Mn–Mo–Nb was finally chosen. The advantages of a low-carbon manganese steel have been reported by previous investigators. Josefsson [22] had reported that reducing the carbon level in a carbon manganese steel would reduce the ITT temperature. However there appeared to be some optimum carbon level between 0.002% and 0.05% which would maximize toughness. Allen and co-workers [23] also reported on their work with carbon manganese alloys. They found for alloys with 0.05% carbon or less, that additions of up to 2% manganese would both increase the strength and reduce the ITT temperature of the alloy. Similar results were reported by Reinbolt and Harris [24]. The beneficial effects of manganese are not as direct as those of nickel because it was shown by Roberts [25] that the main effect of manganese on ITT temperature is to reduce the final grain size of the transformed structure. This is the result of the ability of manganese to reduce the transformation temperature of the austenite-to-ferrite reaction. Roberts [25] reported that, discounting the grain refinement, manganese had very little effect on the ITT temperature. However, this is still a good attribute of manganese since it is a useful alloy for increasing strength without reducing toughness.

The grain refining effect mentioned above is very much like the effect produced by nickel additions. By refining the grain size, the alloy will experience both an increase in strength and a decrease in ITT temperature, as reported by Petch [26, 27]. It was also shown by Low [28] that refining the grain size of steel increases the cleavage fracture stress. Modern steelmaking often utilizes grain refining for property enhancement. The process is performed either through the deformation and recrystallization of the austenite with Nb(C,N) during hot working, or by controlling austenite decomposition reactions to maximize the nucleation rate of new grains, or by a mixture of both mechanisms. In order to successfully use grain refining, careful alloy design and proper thermo–mechanical processing must be employed.

The design philosophy used at Climax Molybdenum was also being employed in the early 1970's by McCutcheon and co-workers in Canada [29], Tanaka and co-workers in Japan [30], and others to develop low-carbon high manganese steel with some microalloying. These steels developed microstructures of fine austenite grain size with nearly 100% acicular ferrite, yield strengths over 70 ksi (490 Mpa), and low ITT temperatures often less than –80°F (–62°C).

In 1981, Lander and co-workers [31] suggested that the addition of a small amount of titanium (0.012 to 0016%) would increase the strength-toughness balance of steels with either an acicular ferrite or mixed microstructures. The advantages of titanium in the form of TiN is that it is stable to higher temperatures than Nb(C,N), thus increasing the temperature range for austenite grain refinement from hot working. This microalloy-

ing tool was used by Nippon Steel Corp. to develop a family of steels called "Ultra-Low-Carbon Bainitic Steel." ULCB steel, as reported by Nakasugi and co-workers[32, 33].

The ULCB steels are based on a very low carbon steel with 2% manganese and microalloying additions of Nb, Ti, B, and Al. The chemical compositions of the X–65, X–70 and X–80 grades of ULCB steel are listed in Table 1. These steels are modern extensions of the older low-carbon manganese-molybdenum-niobium steels developed by Climax Molybdenum. However, Nippon Steel has included the use of boron to increase hardenability, as demonstrated by Irvine and Pickering [9] and hence to permit air cooling. These steels also had the very low carbon levels of the Ford alloy [10, 11]. In addition, titanium was used to protect the boron from nitrogen by forming fine TiN which promotes austenite grain refining during hot working. It appears that every component of these alloys was designed with the goal of optimizing strength and low temperature toughness. The mechanical properties and Charpy V-notch toughness are listed in Table 2. The properties of these steels appear to be attractive; however, there are drawbacks. The 0.02% carbon level can be achieved in many modern steelmaking facilities throughout the world but only with the use of expensive electrolytic manganese and not (carbon-bearing) ferro-manganese. An additional drawback is the need for high quality steelmaking practices since the composition limits and processing procedures are very stringent. However, this problem is likely to diminish in the near future as steel producers modernize their facilities.

The microstructures and the properties of these ULCB steels and other developing steels of similar types are the subject of the present investigation. In order to control the fracture behavior of these modern low-carbon steels, the metallurgist must identify and understand the fracture-controlling mechanisms which operate in both the base plate and the heat affected zone. This is pursued in the research by employing fracture mechanics and the concept of the cleavage fracture stress and associated toughness parameters to the microstructure.

BACKGROUND

FRACTURE MECHANICS

The field of fracture and fracture mechanics attempts to understand and describe the behavior of materials in the presence of a crack or a flaw. This knowledge is crucial for the proper use of modern high strength steel. Not only are these steels as flaw-sensitive as other materials, such as high strength aluminum or titanium, but they also display a large variation in fracture behavior due to temperature-sensitive fracture-mode changes. This ductile-to-brittle-transition can cause a tough structural steel to behave more like a brittle glass. Since toughness and strength are required of materials used in most critical structures, it is necessary that the full range of fracture behavior be understood and controlled. This section will review the history and state of the science of the fracture of steels.

The first significant development in the understanding of the ductile-to-brittle transition in steels was contributed by Orowan in 1945 [34]. He developed a model to explain the observed notch behavior of steel. This behavior was such that above a certain temperature both smooth and notched specimens of a given steel were ductile and failed as the result of significant loads and plastic deformation. As the temperature was lowered, however, the notched bar first displayed brittle fracture occurring with little or no

observed plastic deformation while the smooth bar remained ductile, and at a lower temperature still both the smooth and notch bars failed in a brittle fashion. Orowan postulated that there was a single, brittle fracture stress for each material that was not strongly dependent upon temperature. When the applied stress in the steel exceeded this brittle fracture stress, the metal would fail by brittle cleavage. The temperature dependence of this event was the result of the fact that the yield strength of the metal would increase as the temperature was decreased. Therefore, above a certain temperature, the steel would yield before it could sustain the stress needed to cause cleavage fracture. The difference in temperature dependence of the smooth and notched bars was due to the stress elevation known to occur in the vicinity of a notch. Orowan calculated this stress intensification factor with the use of slip line fields for a bar with two co-planar surface cracks. The value of the maximum stress below the notch was 2.57 times the yield strength. In this way, the notched bar could generate the high stresses needed to initiate cleavage while the yield stress of the steel was still less than that of the cleavage fracture stress. This is shown schematically in Fig. 6. Although this concept explained the observed behavior, there was no experimental data to prove the model, nor did the model give any indication of what in the metal controlled the cleavage fracture stress.

An earlier attempt to model crack extension from a flaw in a brittle material was presented by Griffith in 1920 [35]. This model was based on a thermodynamic approach which equated the change in stored elastic energy to the energy needed to create the new surfaces of the growing crack. The model assumed complete linear elasticity and produced the following equation for a crack in a tensile stress field:

$$(\sigma^2 \pi a)/E' = 2\gamma_e \qquad (1)$$

where s   = applied stress

a   = 1/2 total crack length

γ_e = surface energy

E   = effective modulus

= E in plane stress, or $E/(1-\nu)$ in plane stress

ν = Poisson's ratio

The equation can be used to predict the fracture stress (σ_f) of brittle materials when in the following form:

$$(\sigma_f) = ((2\ E'\ \gamma_e)/(\pi\ a))^{1/2} \qquad (2)$$

Although the applicability of the equation was limited to only very brittle materials, it did demonstrate that a global parameter like stress could be related to the crack tip behavior without exact knowledge of the crack tip processes. This concept led to the development of the energy release rate parameter G. This parameter measured the change in the stored elastic energy of a specimen as a function of crack extension.

The acceptance and strength of a critical value of G as a fracture toughness parameter was the result of Irwin's [36, 37] demonstration that the value of the energy release rate could be related to the stress field near the crack tip. These stress field equations were generated using the Westergaard solutions [38] for the equations describing the contact stresses for two plates in compression, with reversed loading conditions. Analysis

and inspection of the stress field equations lead to the stress intensity parameter K, which is defined for a crack in an infinite body as:

$$K = \sigma \ (\pi \ a)^{1/2} \qquad (3)$$

It was demonstrated that these K stress intensity fields could be used to calculate the strain energy release rate G. The proof requires the integration of the stresses and displacements at the crack tip needed to close it an amount da. This energy is then equated to G. The results were as follows:

$$Gda = (\sigma^2 \pi a / E') \ da \qquad (4)$$

And substituting equation 3 the solution produces:

$$G = K^2 / E' \qquad (5)$$

Thus the global parameters used to calculate the energy release rate could be related to crack tip processes.

The stress intensity factor K as a fracture mechanics parameter has received wide acceptance and is used to measure the resistance of high strength steels to crack extension. However, there is a significant limitation to the use of this concept. The limitation is imposed by the use of linear elasticity to describe the material behavior. The stress intensity solutions describe the stresses as approaching an infinite value close to the crack tip as shown in Fig 7. Since real metals have finite yield strengths, the K solution cannot properly describe the stress field near the crack tip where yielding and plasticity occur. To mitigate this problem, linear elastic fracture mechanics (LEFM) could only be applied when the plastic zone was very small compared to the specimen or crack size. The actual stress field at a crack tip can now be modeled using a combination of LEFM, finite element analysis and actual material properties. However, the calculation of the Orowan cleavage fracture stress from K values is difficult, as will be discussed below.

The cleavage fracture stress can be measured using notched specimens which do not have the stress singularity at the tip. This method as described by Knott and Cottrell [29] uses the results of a slip line field analysis to calculate the stress multiplication factor (Q) for a notch [40] in a material at general yield. This Q factor at the point of general yield can be calculated from the notch angle θ (Fig. 8) as follows:

$$Q = 1.15 \ \sigma_y \ (1 + \pi/2 - \theta/2) \qquad (6)$$

Knott then reported that this technique could measure the brittle fracture stress in steels and that these values were temperature independent for a given steel [41], as shown in Fig. 9. This cleavage fracture stress was the maximum stress generated below the notch and was therefore associated with the process of cleavage propagation. The technique of using notched bars to measure the cleavage fracture stress was improved with the published finite element solution of near notch tip stresses by Griffiths and Owen [43]. This solution was based on a real steel with a hardening coefficient of 0.1, rather than the assumed perfectly-plastic material behavior of the slip line-field solution. A comparison of the two solutions is shown in Fig. 10. With this tool researchers can measure the stress of a micro-mechanical process in various materials.

When examining the fracture surface or microstructure under the fracture surfaces of a steel specimen it is often difficult to identify the actual initiation site of the cleavage fracture. However, some careful studies of steel microscopically examined after various level of interrupted deformation have been of help. The results of McMahon and Cohen [44] revealed that plastic deformation can cause grain boundary carbides to crack and initiate a transgranular crack. In addition, it was observed that these cracks could arrest at discontinuities such as grain boundaries and remain benign. Such evidence indicates that plastic deformation is a necessary but not sufficient event for cleavage fracture. This agrees with the observations reported by Low [45] that the cleavage fracture stress in tension was the same as the yield stress in compression of steel tested at various temperatures, as shown in Fig. 11.

The effects of the observed cracked carbides on the cleavage fracture process were modeled by Smith [46] using dislocation theory. The resulting equations for the effective shear stress needed to crack a grain boundary carbide or grow a crack from a grain boundary are given below:

$$T_s = (T_y - T_i) > ((4E'\ \gamma_c)/(\pi\ d)) \tag{7}$$

$$T_s = (T_y - T_i) > ((4E'\ \gamma_f)/(\pi\ d)) \tag{8}$$

where T_s = effective shear stress

T_y = applied shear stress

T_i = internal shear stress

γ_c = surface energy of carbide

γ_f = surface energy of ferrite matrix

d = grain size

The model which linked the concept of the Orowan's cleavage fracture stress to the Irwin stress intensity factor K was published by Ritchie, Knott, and Rice [47], and is known as the RKR model. This model assumed that cleavage fracture would occur if the cleavage fracture stress was applied over a microstructural component controlling the initiation of the cleavage failure. The size of the microstructural feature which is active in the fracture process was called the characteristic distance or length. Since the cleavage fracture stress and the microstructure do not change as a function of the fracture test temperature, the variation in KIc with temperature was felt to be due to the change in yield strength. The RKR model used the Smith [46] approach to relate the microstructure to a cleavage fracture stress and an elastic-plastic stress distribution for a sharp crack [48] to relate the cleavage stress within the plastic zone to the applied stress intensity level. The feature of the microstructure controlling cleavage for a mild steel was assumed to be a function of the grain size. This assumption was based on the well established relationship between cleavage toughness and grain size in mild steel. The results of this analysis for two assumed multiples of grain size are shown in Fig. 12. The best fit was accomplished when the microstructural controlling feature or characteristic distance was assumed to be twice the grain size of the steel. The value of two grain sizes was not believed to be a universal factor but the RKR model was accepted as the description of the interaction of microstructure and measured cleavage fracture toughness.

Using the RKR model, Curry and Knott [49] investigated the cleavage fracture resistance of mild steel as a function of grain sizes from 12 to 85 μm. Their results showed that there was no characteristic distance that was a fixed multiple of the grain size. These results are reproduced in Fig. 13. Since the ratio of the characteristic distance to grain size increased as the grain size decreased, the controlling mechanism could be related to the carbide size and distribution. After further investigation Curry and Knott reported [50] that the critical cleavage fracture stress could be related to the largest (top 5%) carbides in the microstructure. They proposed a relationship between these carbides and the fracture stress using a modification of the Smith model [46]. Their expression substituted the Hall-Petch relation for the grain size. The resulting equation is shown below:

$$\sigma_f + (k^2/C_o)(1 + (4T_i \ C_o^{1/2})/\pi)^2 > 4E' \ \gamma_e/\pi \ C_o \quad (9)$$

where σ_f = fracture stress

      k = Hall-Petch parameter for grain size to yield strength

      C_o = carbide thickness

      T_i = lattice friction stress

      γ_e = effective surface energy

      E' = effective modulus

Curry and Knott showed this linear relationship between the fracture stress and the largest carbides (Fig. 14). They also reported that the data could be fitted with a modified Griffith expression for a penny-shaped crack in a tensile stress field (Eq. 10) and an assumed *effective surface energy of 14 J/m*.

$$\sigma_f = ((\pi \ E' \ \gamma_e)/(2r))^{1/2} \quad (10)$$

r = radius

σ_f = critical fracture stress

The fracture stress measurements plotted in Fig. 14 were obtained using a notch bend test where the maximum tensile stress is produced over an area which is large compared with the carbide spacing. The stress distribution created by a sharp crack is very different. The maximum stress can be much greater and the stress gradient is much steeper. Therefore it would be possible for a smaller carbide (less than the largest 5%) to be in a region of the plastic zone with a stress higher than the fracture stress measured by notch bend tests. This smaller carbide could conceivably initiate the cleavage fracture process if a larger carbide was not in a highly stressed region. Curry and Knott [51] suggested a statistical approach would be needed to model the cleavage fracture process from a sharp crack. The model must take into account the carbide distribution, the stress distribution and the probability that a cracked carbide would be in a volume stressed sufficiently to grow the crack into the ferrite matrix. The carbide distribution needed to support this model would only need to consider particles from about 0.02 μm in size and greater. Carbides smaller than this size would require cleavage fracture stresses that are much greater than those generated in the plastic zone of a sharp crack. In steels with a fine carbide precipitate due to low carbon level or microstructure control, the cleavage controlling microstructural features may not be carbides but large non-metallic inclusions

as was shown by Tweed and Knott [52, 53] and later by McRobie and Knott [54]. These non-carbide crack starters obeyed the same laws as the carbides and could be modeled using Eq. 10. It appears that a proper understanding of the cleavage fracture process in steels requires a knowledge of the size, shape, and distribution of the possible crack starters such as carbides and non-metallic inclusions. It is also necessary to know some bulk material properties such as modulus, yield strength, and the effective surface energy of the steel. Additionally, a description of the stress field of interest is needed, whether it is that of a sharp crack or a notch. And finally, a statistical model is needed to assess the probability that enough likely crack starters will be present in highly stressed regions of the plastic zone to initiate the propagation of a cleavage crack.

In summary, the cleavage fracture behavior of carbon steels has been the subject of considerable research in revealing the micro-mechanics of cleavage fracture. The developing family of ULCB steels have shown very promising mechanical properties which could lead to the development of many new high strength, tough, weldable steels. In order to facilitate this development, more research is needed to uncover the fracture controlling mechanisms responsible for the toughness of ULCB steel. The objective of the research described in this report was to investigate the cleavage fracture behavior of several ultra-low-carbon-bainitic steels and identify the features which control, or contribute to, the fracture behavior of the steel. Such an understanding would help lead to improved toughness in future ULCB steels.

MATERIALS

The materials used in this investigation represent a range of ultra-low carbon steels which all share a carbon level of less than 0.03%. These steels include a commercially produced plate of 1.6Mn–B–Ti, ULCB X–65 (Nippon Steel), a similar laboratory heat of 2Mn–B–Ti, ULCB X–70 (United States Steel), and two experimental chemistries of new ULCB type steels The two experimental steels are the result of a ULCB steel alloy development program being performed at the University of Pittsburgh.

The chemical compositions of the subject steel plates are give in Table 3 together with the assigned DTRC material code and source of each plate. The common features of all these steels, in addition to low carbon, are the alloying elements titanium, boron, and manganese. Table 4 is a short summary of the casting and rolling history of these plates. The six plates of 1 Mn–Mo–Ni steels designated GHB, GHD, GHG, GHC, GHE, and GHH were the result of a rolling reheat temperature variations study of two plate chemistry compositions. This study was performed at the University of Pittsburgh. The room temperature tensile mechanical properties of the subject plates are listed in Table 5. All the materials displayed good ductility, and all but one plate had yield strengths over 70 ksi (500 MPa).

The optical microstructures of the steels are shown in Figs. 15 through 22. The metallographic specimens were all hand polished with a series of abrasives down to a size of 1 μm. The typical etch used to reveal the microstructure was 15 seconds in 2% Nital followed by about 1 minute in 2% Picral, unless otherwise stated. All of the plate materials had clean microstructures with very few large inclusions since they were to be representative of modern clean steelmaking processes.

In Fig. 15, there are two photomicrographs of the 1.6Mn–B–Ti, ULCB steel from Nippon Steel (GEM). The structure here is not bainitic but appears to be polygonal ferrite with fine elongated grains. The typical grain size is 3 to 6 μm high and 5 to 15 μm long. The structure most likely resulted from extensive rolling above the bai·te start temperature taking advantage of the "bay" created by the effect of boron as shown in Fig. 2. At the X–65 strength level, this structure of the fine ferrite produced the required strength with excellent toughness.

Figure 16 presents the photomicrographs of the high manganese (1.9 Mn–B–Ti) ULCB steel plate (GCZ). This material has an acicular/bainitic structure which requires the use of transmission electron microscope analysis to provide full description. Within the structure there appear to be small islands of retained austenite or M–A constituent [55]. The microstructure does not appear to have any significant grain elongation indicating that the plate did not receive any significant rolling reduction in the low temperature range.

The microstructure in Figs. 17 (GHB), 18 (GHD), and 19 (GHG) are from the three plates of the same chemistry; 0.02%–C, 1–Mn, 0.5–Mo, 0.5–Ni. The microstructure is mainly acicular/bainitie, possibly with some polygonal ferrite. The structure appears to be elongated as a result of the austenite deformation without recrystallization. This 'pancake' structure is inherited by the transformed structure. The elongated grains have approximate dimensions of 10 by 20 μm. The microstructure which appears to have the largest grain size was plate GHG which was rolled after a reheat treatment of 1250°C.

Figures 20 (GHC), 21 (GHE), and 22 (GHH) are from the heat of steel containing 0.02%–C, 1–Mn, 1–Mo, 1–Ni. These steels appear very similar to the leaner steels discussed above. However, a reduction in grain size is evident with these more highly alloyed plates having a finer structure of elongated grains. This may reflect an increase in the recrystallization temperature of the steel with increased molybdenum content.

EXPERIMENTAL METHODS

This investigation was designed to measure and analyze the fracture toughness of ULCB steel plates. This was performed using quasi-static and dynamic notch bend tests. The test specimens were machined in the TL orientation following ASTM E399–78. This orientation will apply the maximum tensile load across the rolling direction with the notch pointing along the rolling direction. The quasi-static notch bend test used a 1/2 inch (12.7 mm) square bar with a minimum length of 3–1/4 inches (85 mm). The specimen was machined with a 45 degree notch cut to a depth of 1/3 the thickness with a root radius of 0.010 inch (0.25 mm) as shown in Fig. 23. These notch bend specimens were tested under four point bend loading in a screw driven Instron test machine with a 5000 Kg capacity. The tests were performed with a cross head speed of approximately 2 mm/minute. The length of the specimen containing the notch (approximately 12 mm) had an iron-constantan thermocouple held near the notch with several layers of masking tape, which also insulated the specimen to reduce thermal fluctuations. The specimen and four point bending fixture were placed in a thermally insulated bath containing liquid nitrogen. The level of the liquid nitrogen varied with the required test temperature. Before each test the specimen and loading fixture were given time to thermally equilibrate, which resulted in temperature variations during each test of less than 3°C. After each test

the specimens were removed from the bath and immersed in alcohol until they warmed to room temperature. The fracture surfaces of the notched bar specimens were cut off and saved for scanning electron microscopy (SEM) analysis. The remaining portions of the specimens were machined into round tensile specimens. The fracture load was taken from the plot of load versus cross head deflection.

The fracture load from each notch bend test was used to calculate the nominal bending stress using the expression:

$$\sigma_m = 6M/(Bb^2) \qquad \qquad (11)$$

M = bending moment

B = thickness

b = remaining ligament under the notch

This nominal bending stress was divided by the yield stress of the steel at the test temperature (to be described). This ratio was used to obtain the stress intensification factor R plotted in Fig. 10. The maximum stress below the notch was calculated by multiplying the yield stress by the stress intensification factor (R). If the specimen had undergone significant plastic deformation and the R value was higher than 2.5, then the analysis yields a value below the actual stress. The calculated stresses in these cases were plotted with an arrow.

The tensile specimens were tested in a screw driven Mand tensile machine of 50 KN capacity. The temperature of the tensile specimens was controlled in a manner similar to that for the notch bend specimens described above. The specimens were tested with a cross–head rate of approximately 2 mm/minute. The 0.2% offset yield load was calculated using a 0.2% deflection offset from a plot of load versus cross–head deflection. This procedure assumed that change in deflection due to elastic strain changes in the loading train were linear with load and that all the plastic deflection occurred in the gage length of the specimen. The temperature variation during the tensile tests was less than 3°C.

The impact notch bend test were performed using a standard Charpy V-notch specimen and a full size Charpy impact machine. The specimens were tested with iron-constantan thermocouples attached. The specimens were chilled in a cooling bath before test and inserted into the machine with a temperature less than the test temperature. The impact hammer was dropped when the specimen had warmed to the test temperature. The absorbed impact energy was read directly from the impact machine.

RESULTS AND DISCUSSION

MATERIAL GEM 0.02–C, 1.6–MN, 0.001–B, 0.02–TI

The results of the notched bend bar tests are given in Fig. 24. The yield strength of the steel as a function of temperature is shown in Fig. 25. The critical fracture stress to initiate cleavage appears to be 295 ksi (2050 MPa), and also appears to be temperature independent below – 150°C. Although this material is called a bainitic steel by its pro-

ducer, the metallographic results shown in Fig. 15 indicate that the microstructure is polygonal ferrite and appears more like a controlled–rolled steel. Evensen and co-workers [56] reported cleavage fracture stress measurements for a series of low-carbon (0.05% C) manganese molybdenum controlled–rolled steels. Their fracture stress values were a function of the reheat temperature used for controlled rolling. Their critical fracture stress values were 312 ksi (2170 MPa), 358 ksi (2490 MPa), and 377 ksi (2620 MPa) for the reheat temperatures of 1175°C, 1140°C and 1130°C, respectively. These steels had yields strengths similar to that of material GEM but the notched bend specimens used by Evensen and co-workers had smaller dimensions than the specimens used in this study with less than 1/4 the cross sectional area. The smaller specimens may have elevated the fracture stress results which have values slightly above the stress found form material GEM. Evensen and co-workers also reported that the observed fracture stress was very similar for both the polygonal and acicular structures.

Cleavage fracture stress measurements for low-carbon bainitic steels have been reported by Brozzo and co-workers [57]. Their critical stress values appeared to correlate with the inverse square root of bainite packet size and ranged from 243 ksi (1690) MPa) to 386 ksi (2680 MPa). These values encompass the value for the GEM plate and the Evensen data.

The fracture surfaces of the low temperature notch-bend specimens were examined using a scanning electron microscope (SEM). The fracture surface appeared to have quasi-cleavage facet sizes on the order of the grain size of material GEM (Fig. 26). SEM examination of all the GEM fracture surfaces did not indicate any identifiable cleavage initiation sites. Splitting of the fracture surfaces was evident on all the specimens, even on those which did not fracture from the notch. The splits always occurred before the final fracture from the notch. One notched bend specimen which split but was removed from test after reaching maximum load was sectioned to reveal the fracture surface of the split, and an SEM photograph is shown in Fig. 27. The figure shows the notch root with some shear crack extending from the root. The figure also shows the origin of the split to be in a region 100 to 300 μm below the notch. Closer examination of the region found no apparent crack initiation site. One of the specimens tested at –196°C appears to have failed as a result of the split initiating the final cleavage crack.

Splits in low-carbon HSLA steels have been studied by Baldi and Buzzichelli [58]. They reported that splits appeared to initiate at small manganese sulphide inclusions which produced a lower fracture stress in the thickness direction. They also showed that the material texturing produced by controlled-rolling gave rise to anisotropic plastic deformation stresses during the notch bend test. The stress in the thickness direction could reach the critical fracture stress for splitting before the longitudinal stress reached the critical cleavage stress for crack growth in the TL orientation. If the splits are influencing the cleavage initiation process in the TL orientation, then the measured critical stress of 295 ksi (2050 MPa) may be below the actual cleavage fracture stress. In either case the fracture stress is high enough to give this material excellent impact fracture toughness with a ductile-to-brittle-transition temperature (DBTT) of less than –75°C, as shown in the Charpy V-Notch specimen results (Fig. 28.)

Since the weldability of these steels is very important, four Charpy specimens with simulated HAZ were tested. These specimens were prepared from blanks that were heat

14

treated in the David Taylor Research Center Gleeble Thermal Simulator to reproduce the same thermal history as experienced in the coarse grain HAZ. The generated thermal cycle was developed for a 3/4-inch (19 mm) plate weld with 80 KJ/in. (31.5 KJ/cm) with a peak temperature of 1315°C and a cooling time of 70 seconds between 800°C and 500°C. The corse grained HAZ structure can produce poor toughness in steels [29]. The results of the impact tests performed on these four specimens are plotted in Fig. 29 together with the results for the "as received" plate. Although the results are few, they do indicate an increase in the impact DBTT of at least 50°C, since the specimens tested at −52°C appeared to be on the lower shelf.

There was also a significant change in the microstructure of the plate as shown in Fig. 30. The new microstructure had large bainite packets within equiaxed prior austenite grains of 30 to 40 μm in size. There also appeared to be some islands of martensite/austenite (M–A) constituent along some grain boundaries. The increase in grain size and the complete loss of the pancake structure indicates that the grains recrystallized at some temperature at or below the peak temperature of 1315°C. Studies of the effects of titanium on the grain coarsening temperatures reported that these temperatures were above 1300°C [59] and above 1400°C [60]. The grain growth observed in the current study had a driving force sufficiently great to overcome the grain boundary pinning action of the Ti(C,N) and the Nb(C,N) particles. A significant portion of the driving force was probably the result of the controlled rolling of the ferrite grains.

The SEM analysis of the fracture surfaces of the Gleeble-treated impact specimens showed that the surfaces were quasi–cleavage. The analysis also revealed three changes in the fracture surfaces compared to the fracture surfaces of the "as received" specimens. First, the cleavage facet size had increased to the size of the new prior austenite grain size (30–40 μm), as seen in Figs. 31 and 32. Secondly, the fracture surface appeared to have areas of secondary cracking along prior austenite grains (Fig. 31). Finally, the SEM analysis revealed possible cleavage crack initiation sites as shown in Fig. 32. When the region shown in Fig. 32 was examined using a stereographic pair of photographs, there appeared to be a flat sided cubic depression measuring about 2 μm in the initiation site together with a small round inclusion. The depression may have been caused by a TiN cube which was lost and the small inclusion may have been manganese sulphide.

Although the Gleeble thermal cycle affected the austenite grain size, the peak temperature of 1315°C was too low to affect the large TiN particles which are precipitated at much higher temperatures [59]. This loss of cleavage fracture resistance cannot be associated only with the presence of the TiN cubes since they were existing in the "as received" plate but in a benign state.

In order to further investigate the effects of changes in microstructure on the cleavage fracture of this steel, specimen blanks were heated to 1000°C for 25 minutes and oil-quenched. These blanks were then aged for 24 hours at 500°C in an attempt to precipitate all the niobium and develop the same yield strength as the initial plate. The resultant microstructure is shown in Fig. 33. This microstructure is similar to the Gleeble treated material with a slightly smaller austenite grain size of about 20 microns, and without any apparent M–A constituent. The yield strength of the heat treated (HT) material, 1.6 Mn–B–Ti ULCB (GEM), (Fig. 34) was very similar to the initial material with only a

small increase in the room temperature properties and nearly identical yield strength at the lower temperatures, as observed by comparing Figs. 34 and 25.

A series of notch bend tests were performed using the HT 1.6Mn–B–Ti ULCB material (GEM). The test results were plotted in Fig. 35, together with the results for "as received" material. At the test temperatures above –196°C, there appears to be a significant reduction in the critical fracture stress from 295 ksi (2050 MPa) to about 250 ksi (1750 MPa). The fracture surfaces of the specimen tested at –196°C appear similar to the specimens tested at higher temperatures with no indication of a change in fracture mode. This effect could be the result of the small plastic zone not sampling any large (TiN) crack nucleation site, so that fracture was initiated from some smaller sites at a high local stress level.

The results of an SEM study of the fracture surfaces revealed the features similar to those observed on the Gleeble treated specimens shown in Figs. 31 and 32. These results for the HT 1.6Mn–B–Ti ULCB material(GEM) appear in Figs. 36 and 37. The facet size and intergranular cracking are shown in Fig. 36. and a typical initiation site is shown in Fig. 37.

The effect of the reduced critical fracture stress on the impact toughness of this material is a shift in the DBTT of nearly 150°C as shown in Fig. 38. An estimate of this shift in the impact toughness transition curve from the critical fracture stress data would be possible if a dynamic yield stress versus temperature curve was available. Superimposing such a curve onto Fig. 36, with the correct stress intensification factor for a Charpy specimen, would indicate the ductile and brittle temperature ranges as shown in Fig. 6. The critical fracture stress could be assumed not to change with strain rate as reported by Oates [61] and by Hendrickson and co-workers [62]. The HT 1.6 Mn– B–Ti ULCB (GEM) specimens appear to have a microstructure similar to that in the coarse grained HAZ (CGHAZ) sample and therefore indicate that the CGHAZ of a weld of this steel would have a brittle region with low resistance to cleavage fracture.

This CGHAZ region with it low toughness would be particularly vulnerable to cleavage in a structure because the strength of the CG HAZ is not higher than the base plate. This condition would lead to early yielding in the CG HAZ due to the notch effect caused by the weld cap or the possible higher yield strength of the weld metal causing a metallurgical notch. In either case, the CG HAZ could experience high stresses and possible cleavage fracture.

In summary, it appears that this material, with a fine polygonal ferrite microstructure, has excellent base metal toughness. However, the recrystallized HAZ has a large grained bainite structure with lower resistance to cleavage fracture. The initiation of the cleavage fracture appears to be associated with the pre-existing TiN cubes.

MATERIAL 0.02–C, 1.9–MN, 0.001–B, 0.02–TI ULCB STEEL

This 1.9 Mn–B–Ti steel (code GCZ) was chosen as an example of the X–80 grade ULCB steel. The critical fracture stress measurements for this material are plotted in Fig. 39 and the yield strength values are shown in Fig. 40. The cleavage fracture stress ranges from 230 ksi to 250 ksi (1600 MPa to 1700 MPa) and appears to be temperature independent down to – 175°C. At a temperature of –196°C the critical fracture stress values increase to 280 ksi (1950 MPa). This curve is very similar to, but slightly lower than, the

results shown in Fig. 35 for the heat treated 1.6 Mn–B–Ti ULCB steel (GEM). In addition the two materials have very similar yield strength versus temperature curves (Fig. 40 and 25) and the low critical fracture stress of material 1.9 Mn–B–Ti ULCB (GCZ) produced a high impact transition temperature of about 0°C as shown in Fig. 41, which is a plot of the Charpy impact toughness results. The fact that GCZ has a lower DBTT than the heat treated GEM with a slightly lower cleavage fracture stress may be a function of the difference in the tensile strain rate dependence of the materials. The photomicrographs in Fig. 16 appear to show some islands of M–A constituent. If these islands are contributing to the low toughness as has been suggested [55], then perhaps the toughness would improve if the hard regions were tempered. Two temperatures, 350°C and 450°C, were chosen to temper the martensite without changing the yield strength of the bainite matrix. Speich [63] reported significant tempering of low-carbon martensite by heating for one hour at 350°C. Several notched bar specimens were tempered for one hour at either 350 or 450°C. The change is hardness for both groups of specimens was from an original value of 225 DPH to 235 DPH, an increase of less than 5%. The small increase in hardness was probably the result of an increase in $Nb(C,N)$ precipitation. The results of the notch bend tests for the two groups of tempered 1.9 Mn–B–Ti (GCZ) specimens are plotted in Fig. 42 (350°C temper) and Fig. 43 (450°C temper). The two sets of results are the same as the results for the "as received" GCZ material. These results indicate that either the M–A phase was not present in the material or that the M–A phase has little to do with the cleavage fracture process in this material.

It had been reported by Nakasugi and co-workers [32, 33] that these ULCB steels need significant plate reduction below 1100°C in order to develop the fracture toughness. This plate had not been subjected to any deformation below 1200°C. A 4 in. by 6 in. (100 x 150 mm) section of 1.9 Mn–B–Ti ULCB (GCZ) was heated to 1000°C for 1 hour and then received a single reduction in a rolling mill from 0.78 inch (20 mm) to 0.5 inch (12.7 mm). The results of the thermomechanical processing on the cleavage fracture strength of material GCZ are shown in Fig. 44 and the yield strength results are shown in Fig. 45. These results indicate that the reduction produced essentially no change in the cleavage fracture resistance of the material GCZ. There was also no change apparent in the impact toughness of the material as shown in Fig. 46. This may have been the result of insufficient reduction below 1100°C.

The SEM analyses of all the fracture specimens of the 1.9 Mn–B–Ti material, GCZ, were similar in appearance, regardless of the tempering or reduction performed. The fracture surfaces were all quasi-cleavage with some regions of possible intergranular secondary cracks as shown in Fig. 47. The other feature observed on all GCZ fracture surface was the presence of TiN cubes associated with cleavage crack initiation sites as shown in Fig. 48. This figure shows an SEM photograph of the upper surfaces of the TiN cube immediately adjacent to a cleavage initiation site. The figure also has a SEM photograph in the back scattered mode which clearly shows the cubic nature of the inclusion. All of the inclusions at these initiation sites were approximately 2 μm in size. There were generally two to six such sites observed on a single fracture surface. All of the sites were calculated to be within the plastic zone generated by the notch loading. At other initiation sites the TiN cube was attached to MnS inclusion as shown in Fig. 49. The results of stereographic photography of this area indicated that the TiN cube was absent and that

only a cubic hole in the material, which was adjacent to the MnS inclusion,remained. Occasionally, TiN cubes were observed the were not near an initiation site as shown in Fig. 50. In this SEM photograph of a pair of inclusions, it can be seen that one of the inclusions is cracked.

The inclusion identification was performed with an energy-dispersive spectrometer called EDS on the SEM. Although an accurate quantitative analysis on a fracture surface is not possible, a qualitative analysis is useful. Figures 51 and 52 show the results of such an analysis. The two figures show the mating area of the two fracture surfaces of one notched bend specimen. It can be seen that a pair of TiN cubes have been pulled out of one surface and remained attached to the other. Again the inclusions are in a cleavage fracture initiation site. Also on the figures are the results of EDS analysis performed on the center of the large cube in each SEM photograph. The analysis used the 'spot mode' on the SEM. The EDS results indicate that the titanium-rich inclusion remained intact while an aluminum-rich part of the inclusion broke off and remained in the cubic hole.

An EDS analysis performed on a further initiation site, shown in Fig. 53, is given in Fig. 54. In this case, two EDS analyses were performed. In one, (Fig. 54A) the spot was placed on the small round portion of the inclusion attached to the upper portion of the cube shown in the back scatter SEM photograph (Fig. 53). The second EDS analysis (Fig. 54B) used an electron beam placed on the center of the cube in Fig. 53. The results indicate that the TiN cube has a MnS inclusion attached to it.

The titanium additions in these ULCB steels are used to form $Ti(C,N)$ which will keep the nitrogen from the boron and form a grain boundary pinning precipitate. For this precipitate to be effective, it must be less than 0.05 μm in size [60]. The 2 μm TiN cubes observed in this 1.9 Mn–B–Ti material (GCZ) and the 1.6 Mn–B–Ti ULCB material (GEM) are much too large to be effective for grain refining. These large TiN cubes are believed to be formed in all steels which have more than 0.01% Ti, as reported by Houghton and co-workers [59]. The particles form in the liquid steel with sizes ranging from 2 to 10 μm [64]; and their population can be reduced by fast cooling to the solid state, as in continuous casting. Once the TiN particles have been formed they cannot be removed or dissolved without remelting the steel [64]. The TiN cube can react with niobium and become coated with a niobium skin [59]. Additionally, the TiN cubes can react with and harden sulphides in steel [65]. This combination of high thermal stability and high chemical reactivity of the TiN cubes may prove difficult if not properly controlled.

The detrimental effects of such TiN cubes have been reported in the literature. Floreen and co-workers reported finding cracked $Ti(C,N)$ at the fracture initiation sites of 0.1%–C Fe–Ni alloys which were killed with aluminum and 0.012% titanium [66]. Smith and co-workers [20] reported that the addition of 0.015% Ti to a low-carbon-manganese-molybdenum steel caused an increase in the DBTT. However, it cannot be assumed that the presence of these TiN cubes always causes detrimental effects on the cleavage fracture resistance of steels. If that were true then the TiN bearing steel, 1.6 Mn–B–Ti (GEM), discussed earlier in this report would not have displayed such excellent impact toughness results.

It may be that the effective use of titanium in steel requires the production of some particular environment around the large TiN cubes which is a function of the thermo-mechanical processing. The cracked inclusions shown in Fig. 50 and the EDS results

18

reported in Fig. 54 indicate that there may be a weak bond between the TiN and other attached inclusions. This bond is already under stress caused by the difference in the thermal expansion coefficient of the TiN, Al2O3, and MnS, as they are cooled from the melt [67]. The rolling below 1100°C may break and separate these particles thus blunting the small cracks. This theory would not completely account for the low toughness of the recrystallized 1.6 Mn–B–Ti material (GEM), since the rejoining of inclusions as a result of recrystallization is hard to imagine. For the positive effects of the thermo-mechanical processing to be reversible, as the data suggest, there may be some embrittling effect in operation affecting the bonding of the large TiN cubes to the matrix. This must be investigated with high resolution analysis such as that on a scanning transmission electron microscope (STEM) with either EDS or electron energy loss spectrum (EELS) analysis. If some modification of the TiN bond lowers the bond strength, then cracking of the bonds may cause the same effects as the cracking of grain boundary carbides, as described in the RKR model [47]. The proof of the inclusion-embrittlement theory requires further investigation.

MATERIAL – 0.02–C, 1–MN, NI, MO STEELS

These steels were the result of the first stage of a ULCB steel development program conducted at the University of Pittsburgh. The six 1Mn–Mo–Ni steels were produced from two chemistries with three different rolling reheat temperatures as shown in Tables 3 through 5. Notch bend tests and tensile test were performed on all six materials. However, only one material, 1–Mn–1Mo–1–Ni ULCB reheated at 1100°C (GHE), was available in sufficient quantity to provide enough specimens to perform a reasonable fracture stress evaluation. The results of the other five plates will be compared to the results of material GHE.

The fracture stress measurements and the yield strength measurements for material 1–Mn–1–Mo–1–Ni ULCB (GHE) were plotted in Figs. 55 and 56. The results shown in Fig. 55 indicate that the cleavage fracture stress may be at 300 ksi (2300 MPa). The lower limit of test temperature was –196°C and, therefore, the temperature independence of this cleavage fracture stress measurement could not be verified. Nevertheless, it appears that the cleavage fracture stress for this material was the highest of all the results of this investigation. These results indicate that a material with an acicular/bainitic structure can have a higher cleavage fracture stress than a material with a fine polygonal ferrite structure. This material had a reheat temperature of 1100°C, which means that all the final rolling was performed at or below that temperature. The results for this material would seem to agree with the work of Nakasugi and co-workers, [32, 33] which reported that rolling below 1100°C was needed to produced good toughness. However, the few available results of the other two plates of 1–Mn–1–Mo–1–Ni ULCB steels rehaeted at 950°C (GHC) and 1250°C (GHH) of this chemistry shown in Figs. 57 and 58, seem to indicate that high toughness can be obtained with reheat temperatures as high as 1250°C. This high cleavage fracture resistance may have been the result of the use of 1% nickel. Floreen and co–workers reported a continual increase in the cleavage fracture stress with nickel additions up to 3.9% in a 0.010%C Fe–Ni alloy system [66].

The three plates of 1Mn–1/2Mo–1/2Ni steel reheated at 950°C (GHB), 1100°C (GHD), and 1250°C (GHG) rolled from the steel of leaner chemistry appeared to have

cleavage fracture strength for the X–65 ULCB steel shown in Fig. 24. These results seem to indicate that the 1–Mn–Mo–Ni alloys should have low ductile to brittle transition temperatures. The Charpy impact toughness results for the six steels agree with the measured cleavage fracture strengths. The impact transition curves were plotted in Figs. 61 and 62 from the data produced by the researchers at the University of Pittsburgh.

The fracture surfaces of the notched bend bars were examined in the SEM. The fracture mode in all cases was quasi-cleavage as shown in Fig. 63. The fracture surface contained very small cleavage facets similar to those in the 1.6 Mn–B–Ti ULCB material (GEM). No cleavage initiation sites could be identified, and no TiN cubes were observed. This would indicate that either no large cubes were formed or they were placed into a benign condition, as was the case of the material GEM in the "as received" condition. This material requires further study to document the distribution of TiN cubes and their surroundings. In addition, notched bars of this material will be subjected to Gleeble HAZ simulations in order to measure the effect of welding on the cleavage fracture stress in the HAZ.

It is believed that this group of materials should not suffer any significant loss of resistance to cleavage fracture in the HAZ as compared with the 1.6–Mn–B–Ti ULCB material (GEM) described earlier. The acicular /bainitic structure in these materials was produced after rolling during air-cooling and should be the same structure produced as the result of a simulated HAZ thermal cycle. Also, the original austenite grain structure of this material should not suffer significant recrystallization since very little grain coarsening was observed for the material reheated to 1250°C. If the HAZ toughness approaches the base metal properties, then the material will be near achieving the original goals of the overall program. However, it is still necessary to understand what controls the cleavage fracture resistance, especially in titanium treated steels.

CONCLUSIONS

The purpose of this study was to investigate the cleavage fracture of several ultra-low-carbon-bainitic (ULCB) steels, and identify and understand the features of these steels which contribute to or controls their cleavage behavior.

Eight different ULCB plates were subjected to slow notched bend, uniaxial tension, and Charpy impact test. The results of these test indicate that it is possible to produce a steel with a yield strength above 70 ksi (500 MPa) with a high cleavage fracture resistance and low impact transition temperature. This can be achieved with an ultra-low carbon steel (0.02% C) in either a polygonal ferrite or acicular/bainitic microstructure. The polygonal ferrite microstructure was not stable when subjected to a simulated HAZ thermal cycle, and the loss in cleavage fracture strength was associated with initiation sites surrounding TiN cubes. The cubes were 2 μm in size and had been formed in the liquid steel. The low cleavage fracture toughness was also accompanied by large cleavage facets and high impact toughness transition temperature.

High cleavage fracture strength occurred in steels that displayed small cleavage facets, low impact transition temperature and unresolvable cleavage initiation sites. The mechanism that causes the TiN cubes to be initiation sites in low toughness steels, while remaining benign in high toughness steels, is unknown, but may be associated with some embrittlement mechanism. Further work is needed to describe and understand the mechanism.

Table 4. Material processing history.

Material Name	Material Code	Casting Method	Reheat Temperature Final Rolling
1.6Mn–B–Ti	GEM	Continuous	<1100°C
2Mn–B–Ti	GCZ	INGOT	>1250°C
1Mn–0.5Mo–0.5Ni	GHB	INGOT	950°C
1Mn–0.5Mo–0.5Ni	GHD	INGOT	1110°C
1Mn–0.5Mo–0.5Ni	GHG	INGOT	1250°C
1Mn–1Mo–1Ni	GHC	INGOT	950°C
1Mn–1Mo–1Ni	GHE	INGOT	1100°C
1Mn–1Mo–1Ni	GHH	INGOT	1250°C

Table 5. Mechanical properties at room temperature.
transverse orientation (TL).

Material Name	Material Code	Yield Strength ksi (MPa)	Ultimate Tensile ksi (MPa)	Elongation %	Reduction in Area %
1.6Mn–B–Ti	GEM	72.5 (503)	85.2 (591)	33	78
2Mn–B–Ti	GCZ	75.2 (521)	96.1 (667)	34	74
1Mn–0.5Mo–0.5Ni	GHB	76.0 (527)	82.8 (575)	34	75
1Mn–0.5Mo–0.5Ni	GHD	80.2 (556)	86.3 (599)	33	74
1Mn–0.5Mo–0.5Ni	GHG	74.5 (577)	83.0 (576)	32	74
1Mn–1Mo–1Ni	GHC	55.3 (384)	79.1 (549)	41	74
1Mn–1Mo–1Ni	GHE	74.1 (514)	97.3 (675)	32	71
1Mn–1Mo–1Ni	GHH	71.4 (495)	91.2 (633)	36	75

Table 1. Chemical compositions of ULCB Steels.

Grade	C	Mn	P	S	Ni	Nb	Ti	B	Al
X–65	0.02	1.60	0.02	0.003	–	0.05	0.016	0.001	0.04
X–70	0.02	1.89	0.02	0.003	–	0.05	0.016	0.001	0.04
X–80	0.02	2.01	0.02	0.003	0.03	0.05	0.018	0.001	0.04

Table 2. Tensile and impact toughness properties.

Grade	Yield Strength MPa (ksi)	Tensile Strength MPa (ksi)	Uniform Elongation %	Charpy Energy at –20°C (–45°C) J (ft-lb)
X–65	490 (70)	580 (84)	45	340 (240)
X–70	520 (75)	630 (91)	38	141 (104)
X–80	591 (86)	716 (104)	35	131 (97)

Table 3. Chemical composition of steels.
(in weight percent)

Material Code, and Source	GEM Nippon Steel	GZC USS	GHB, GHD GHG USS	GHC, GHE GHH USS
Element	2Mn–B–Ti	1.6Mn–B–Ti	1Mn–0.5Mo–0.5Ni	1Mn–1Mo–Ni
C	0.020	0.021	0.018	0.018
Mn	1.59	1.87	0.98	0.93
Mo	–	–	0.52	0.97
Ni	0.02	–	0.53	1.03
S	0.003	0.003	0.003	0.003
P	0.016	0.01	0.005	0.005
Si	0.14	0.15	0.15	0.15
Al	0.0021	0.047	*	*
Nb	0.04	0.10	0.05	0.05
Ti	0.02	0.021	0.016	0.016
N	0.0045	0.003	0.005	0.004
B	0.001	0.001	0.001	0.001

– not analyzed

* addition made but not analyzed
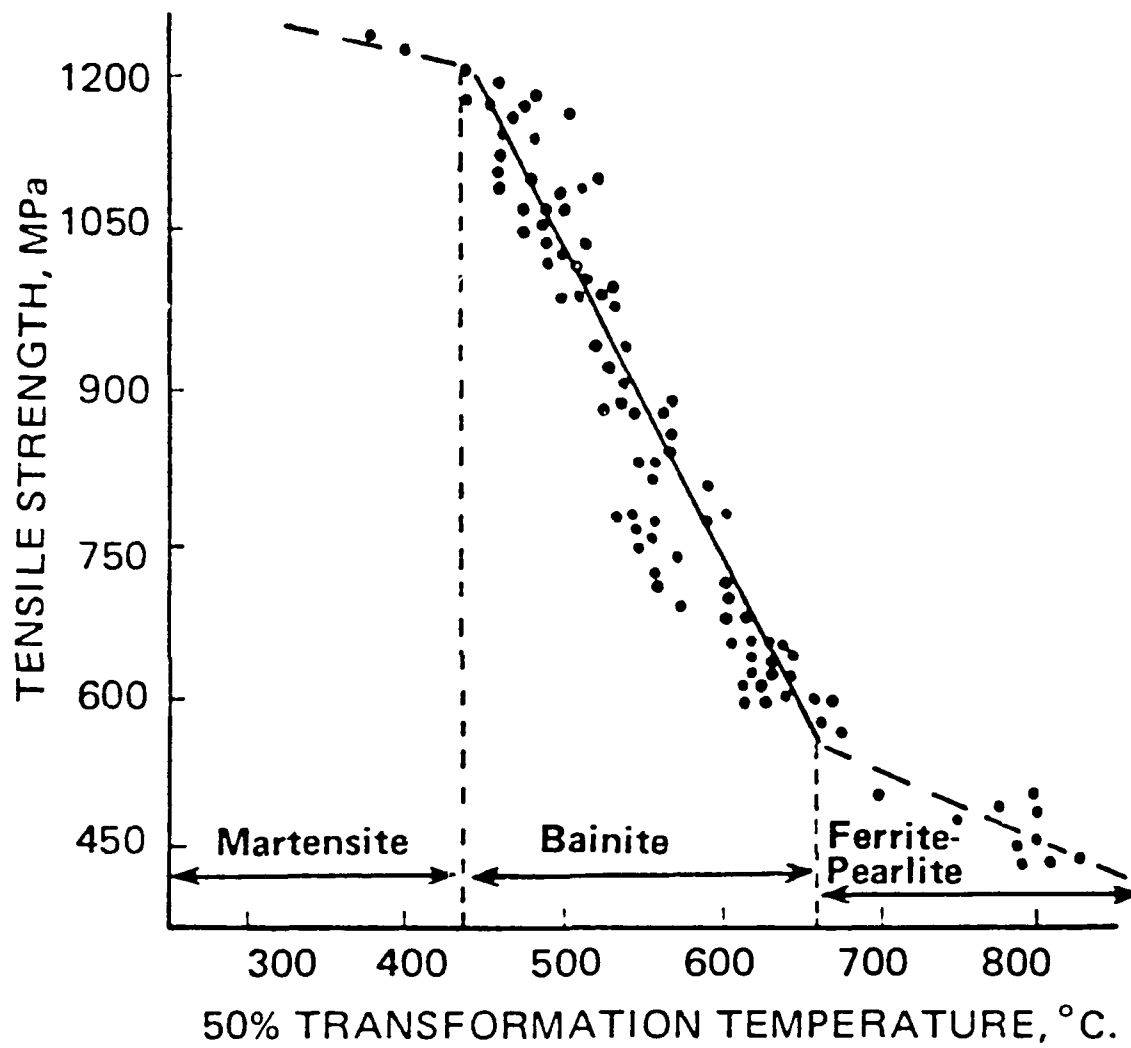
Fig. 1. Effect of 50% transformation temperature on
tensile strength of bainitic steels [7].
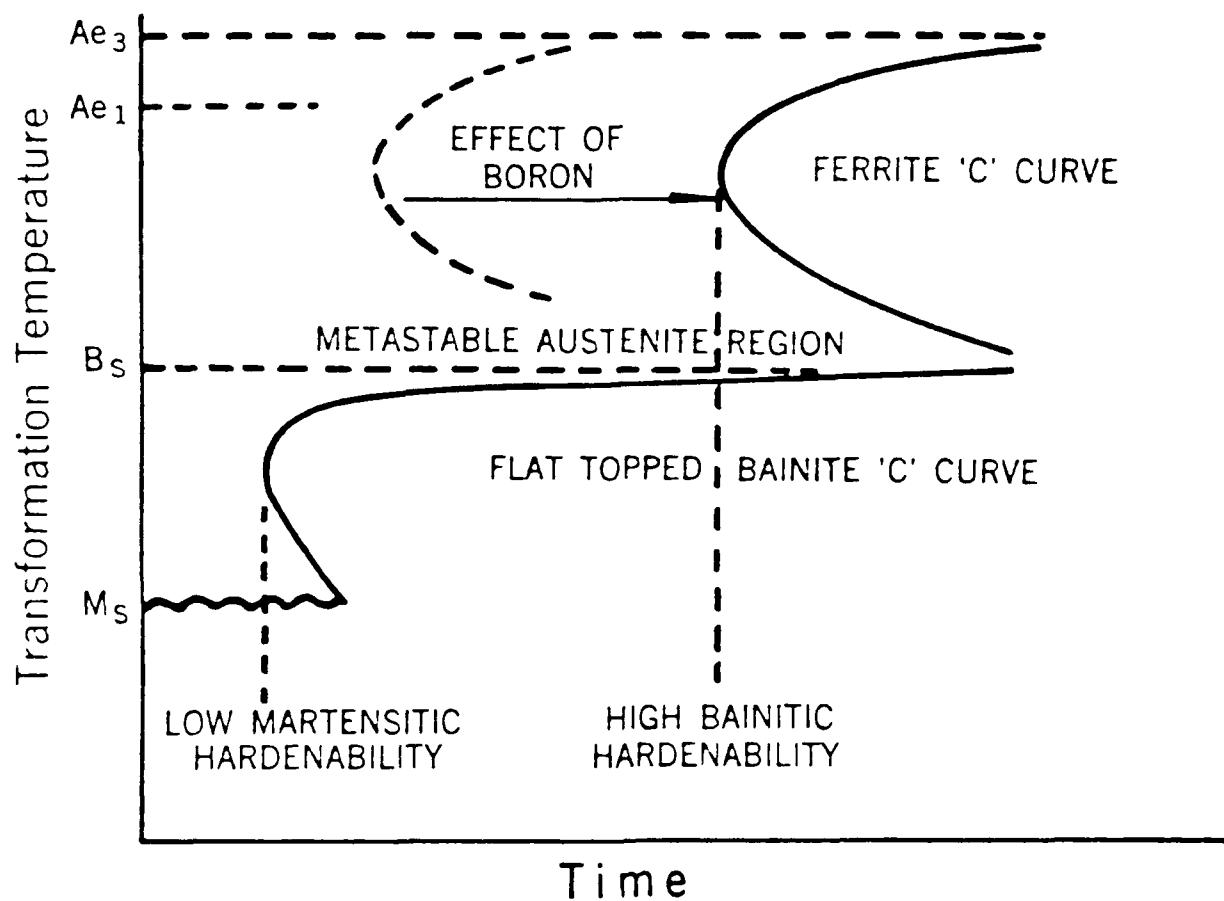
Fig. 2. Schematic diagram of the effect of boron on transformation characteristics of steel [7].
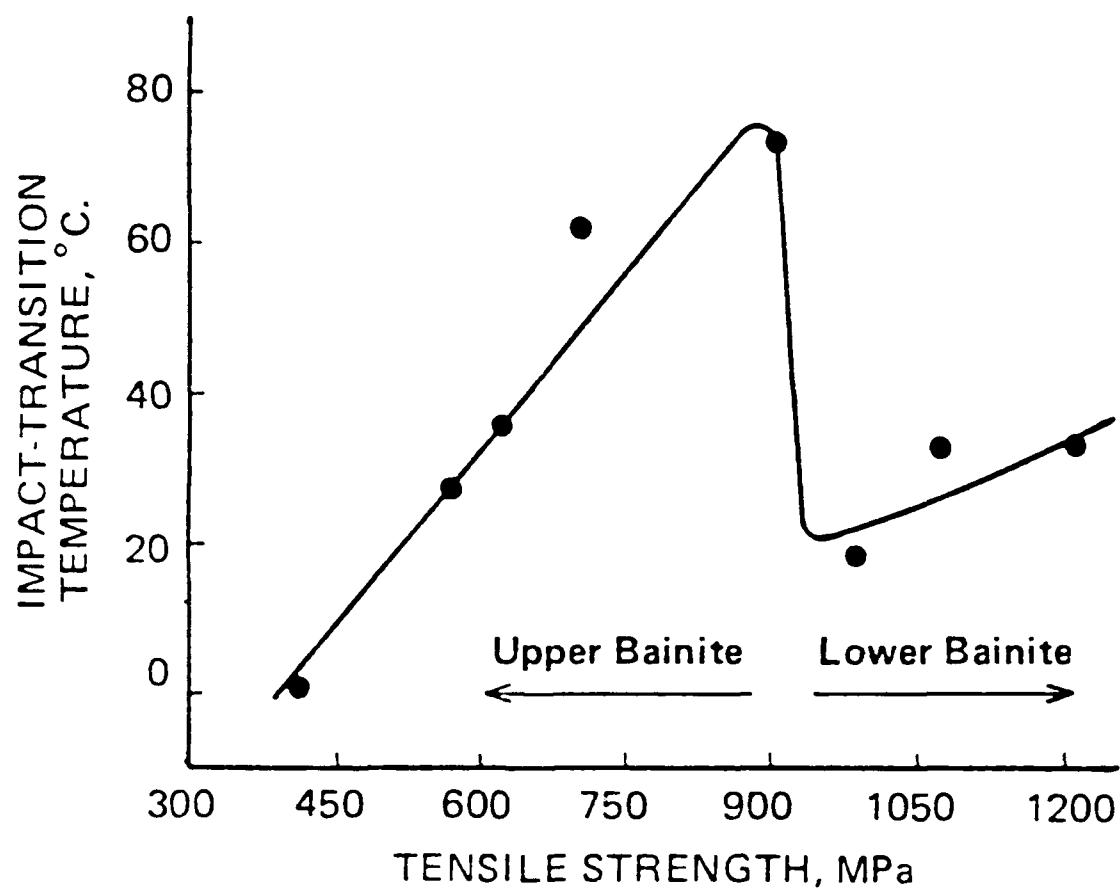
Fig. 3.   Effect of bainitic structure on strength–toughness
relatioinship of low carbon steel [9].
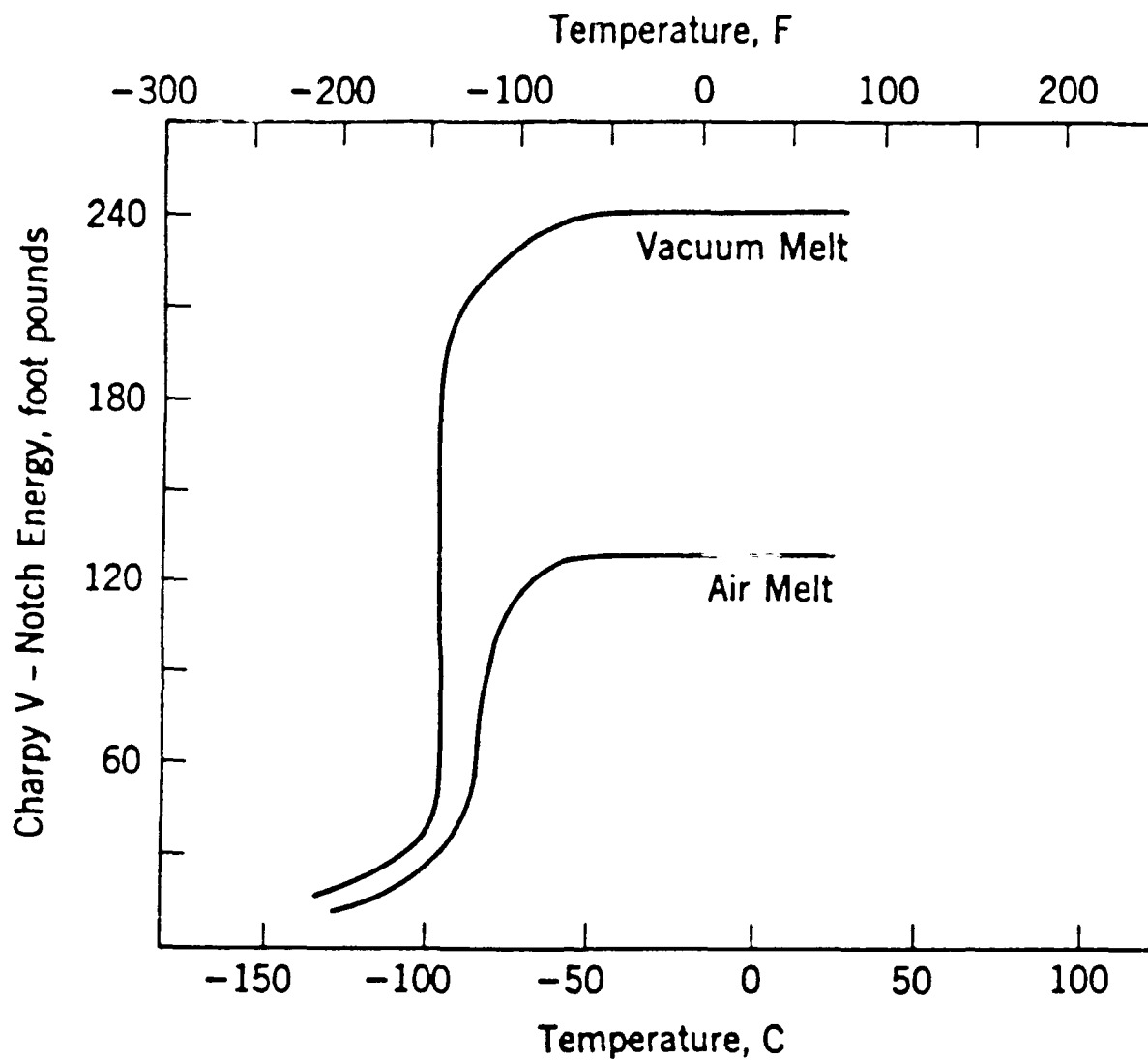
Fig. 4. Impact toughness properties of 3% Ni – 3% Mo steel [10].
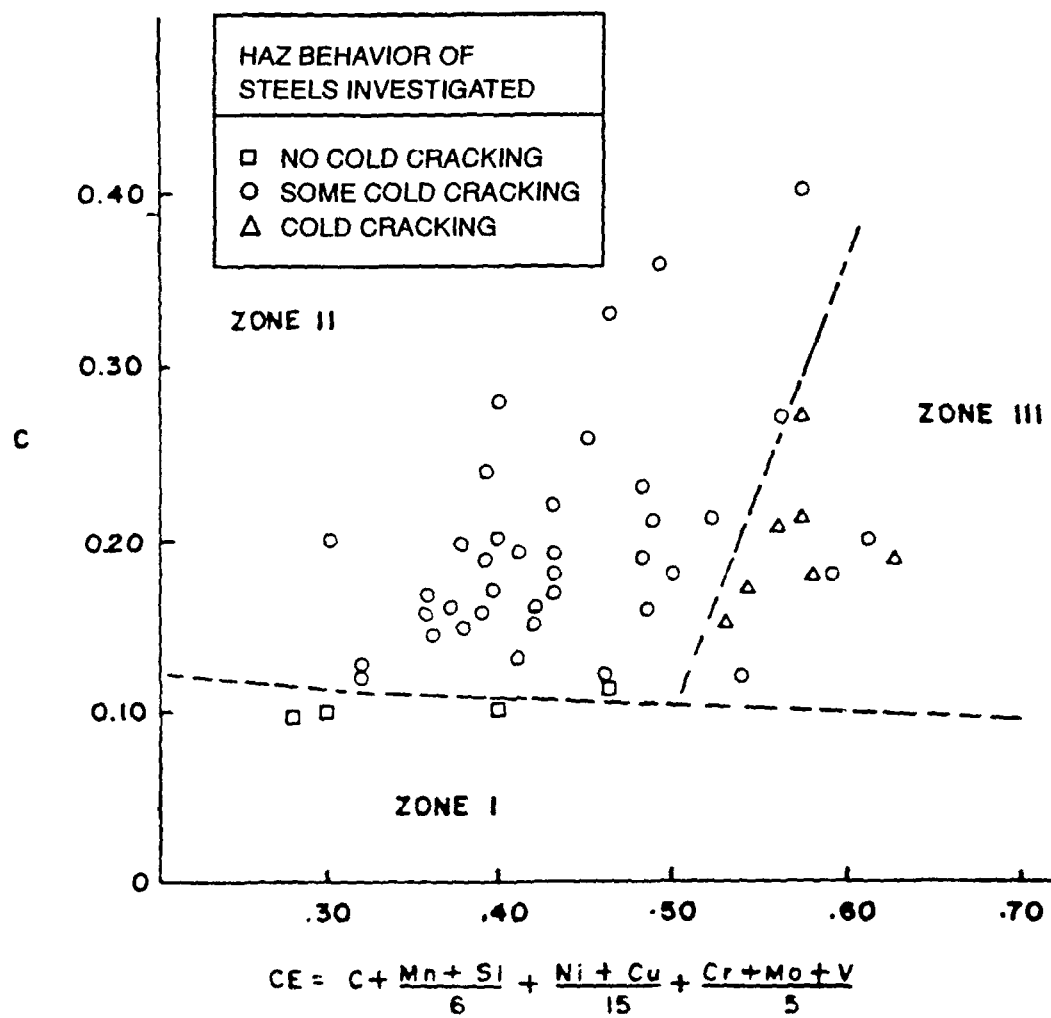
Fig. 5. Classification of the cold cracking resistance of steel [18].

□ ZONE I — No cold cracking —easily welded
○ ZONE II — Some cold cracking — weldable
△ ZONE III — Cold cracking — not weldable

$$CE = C + \frac{Mn + Si}{6} + \frac{Ni + Cu}{15} + \frac{Cr + Mo + V}{5}$$
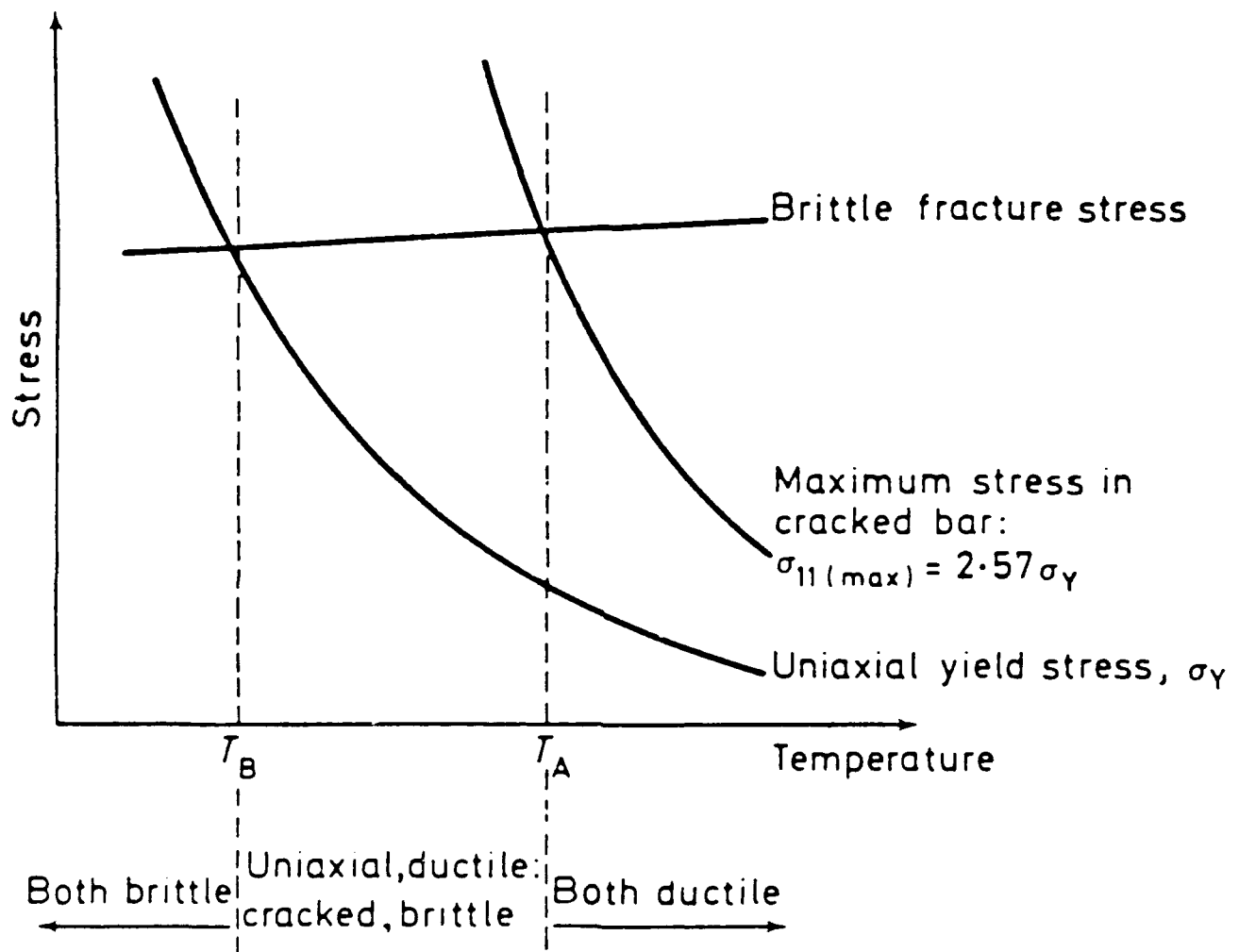
Fig. 6.   Schematic of Orowan's theory of brittle fracture [42].
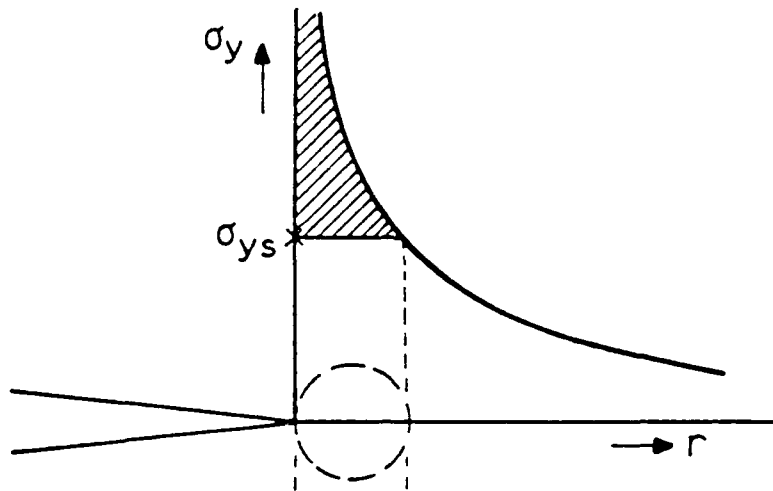
Fig. 7.   Schematic of stress field in front of a sharp crack
with estimated plastic region.
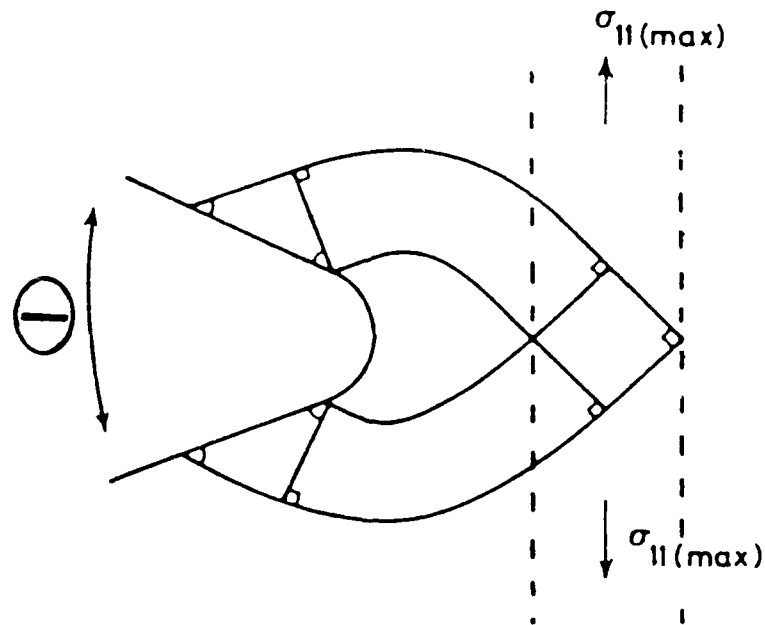
Fig. 8.   Slip line field for notch and notch angle [39].
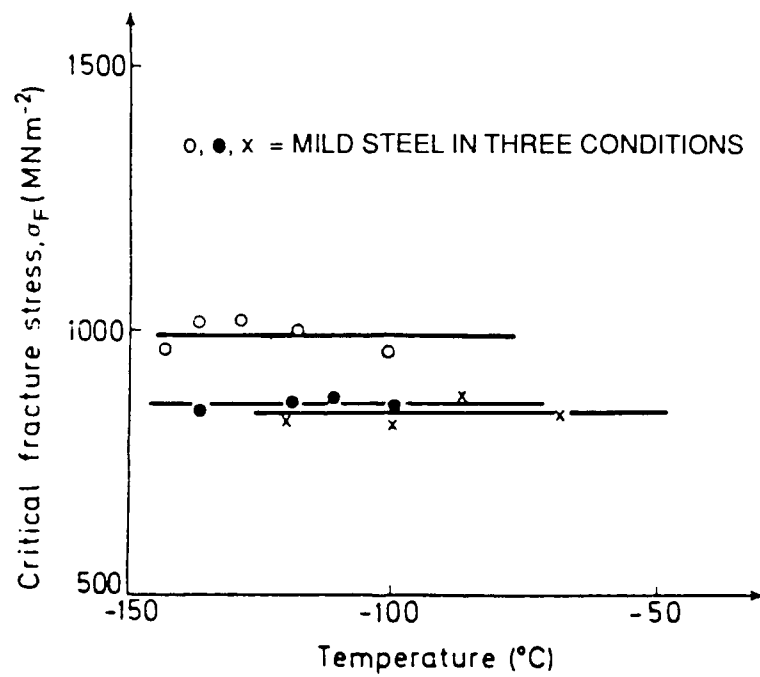
Fig. 9. Critical fracture stress measurements for mild stress [41].
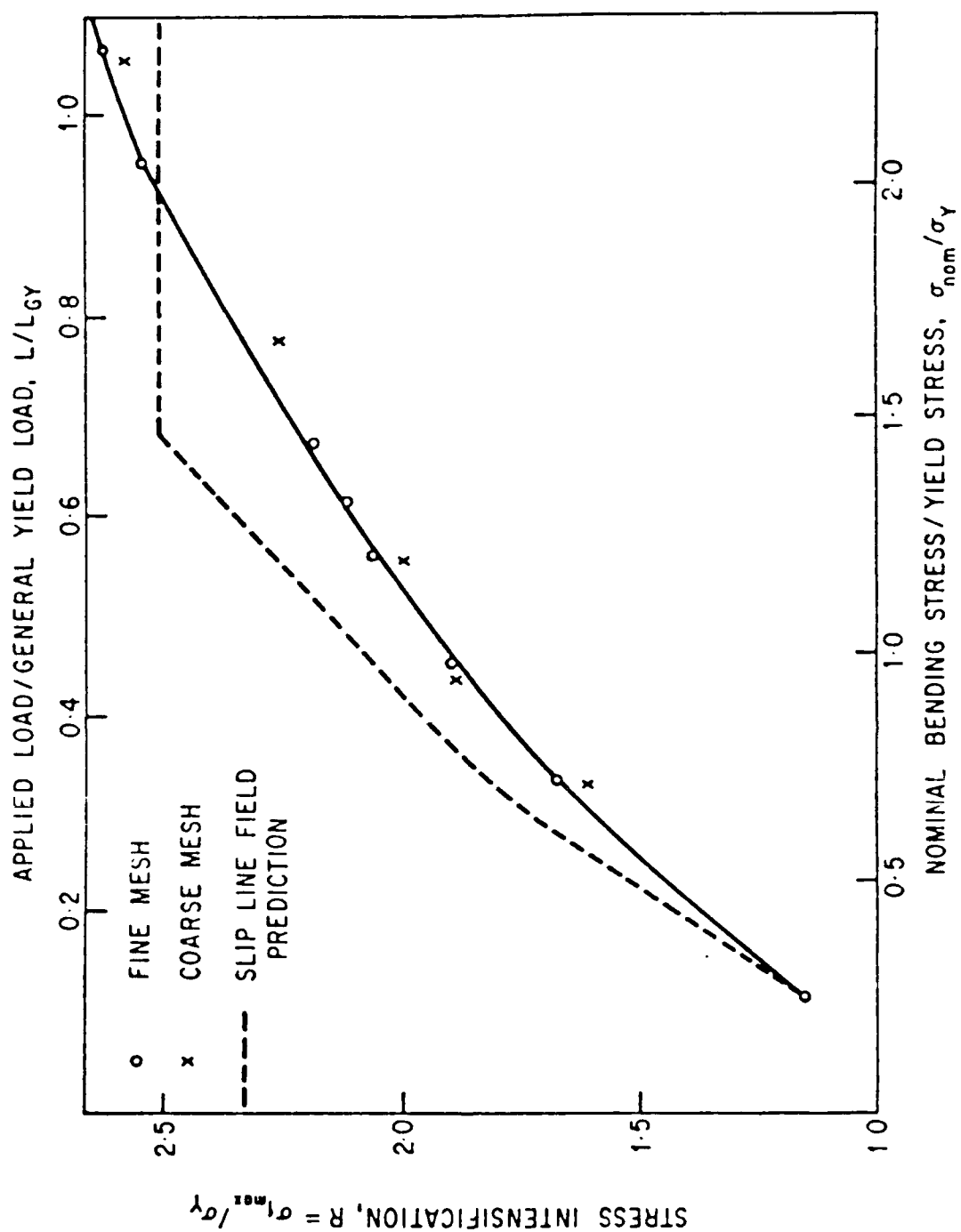
Fig. 10. Variation of stress intensification under a notch with applied load [43].
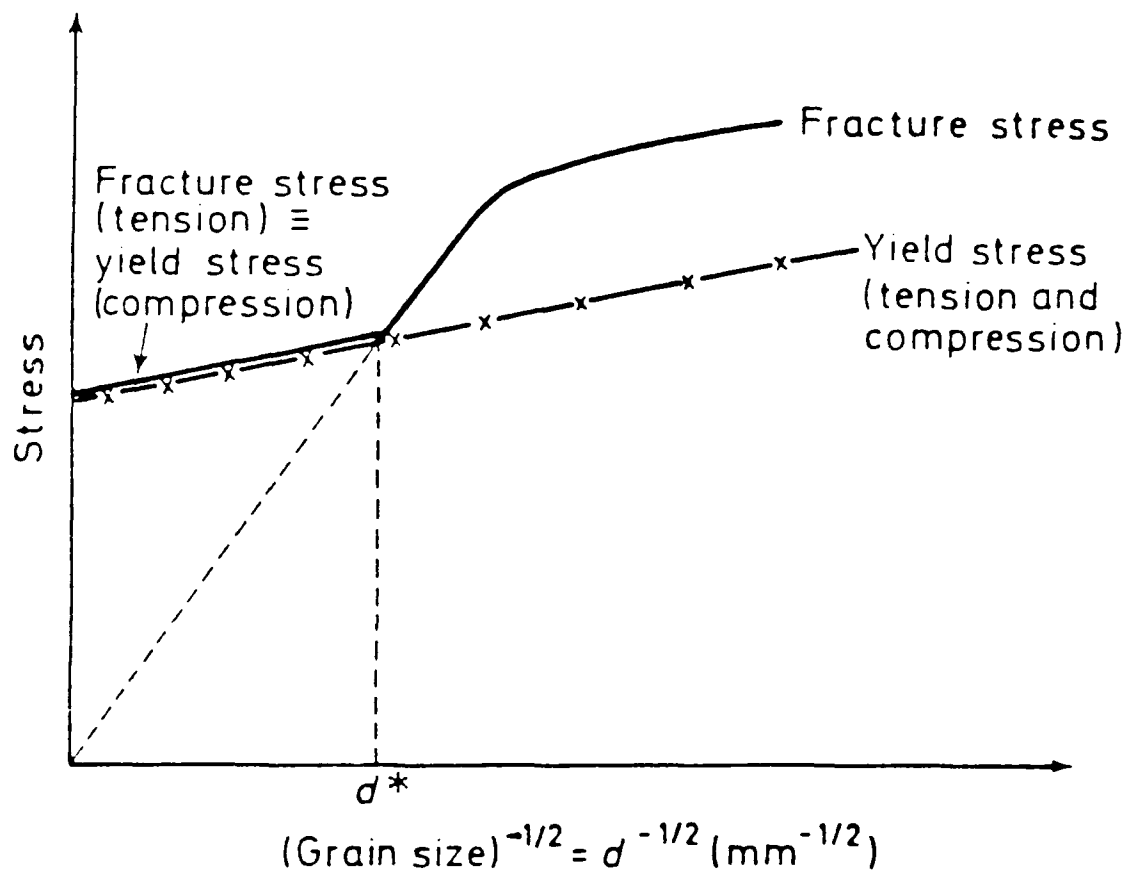
Fig. 11.   Schematic variation of yield and fracture stresses with grain size for mild steel [45] reproduced from Reference 42.
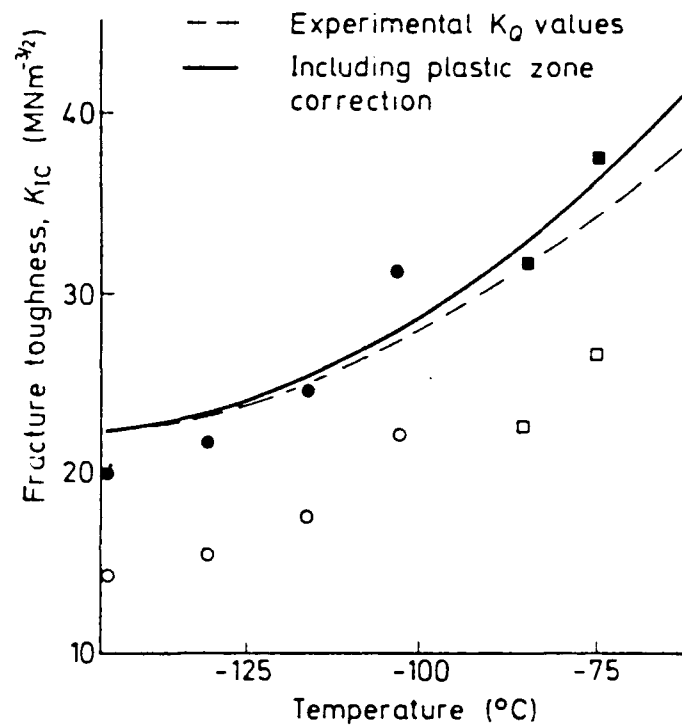
Fig. 12.   Experimental variation of fracture toughness with temperature
and theoretical predictions from Ritchie-Knott-Rice model [46].
Open symbols   – characteristic distance = 1 grain diameter
Closed symbols – characteristic distance = 2 grain diameter
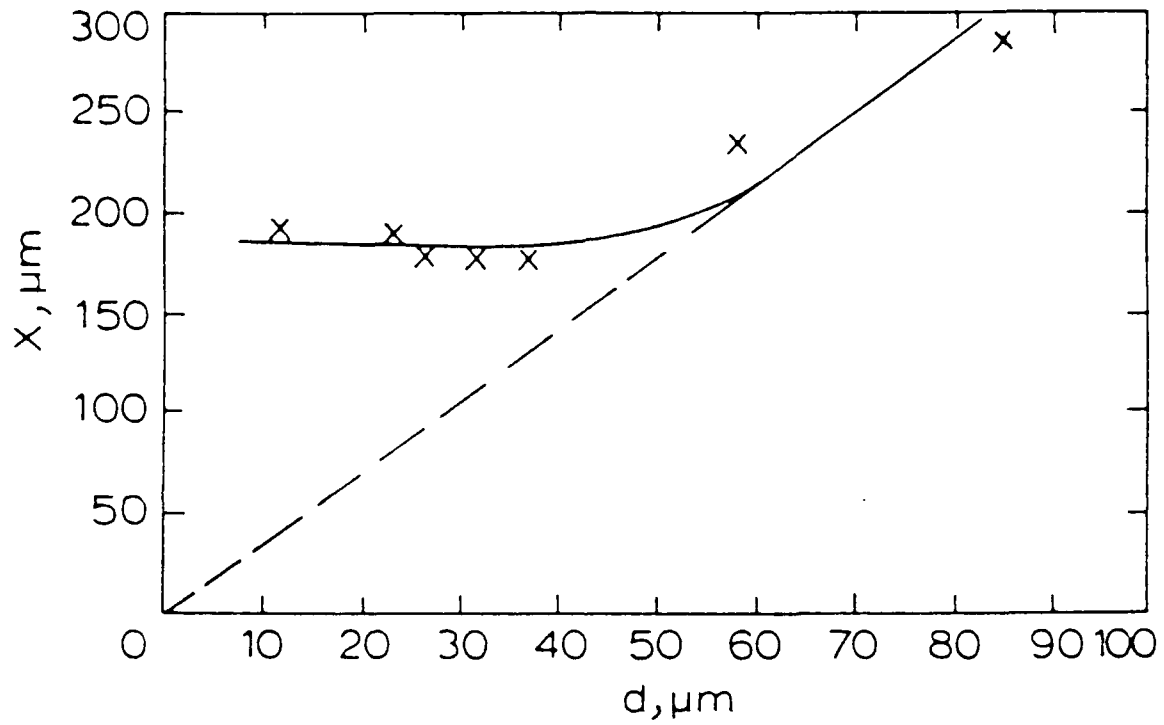
Fig. 13. Variation of characteristic distance (X) with grain size (d) for mild steel [49].
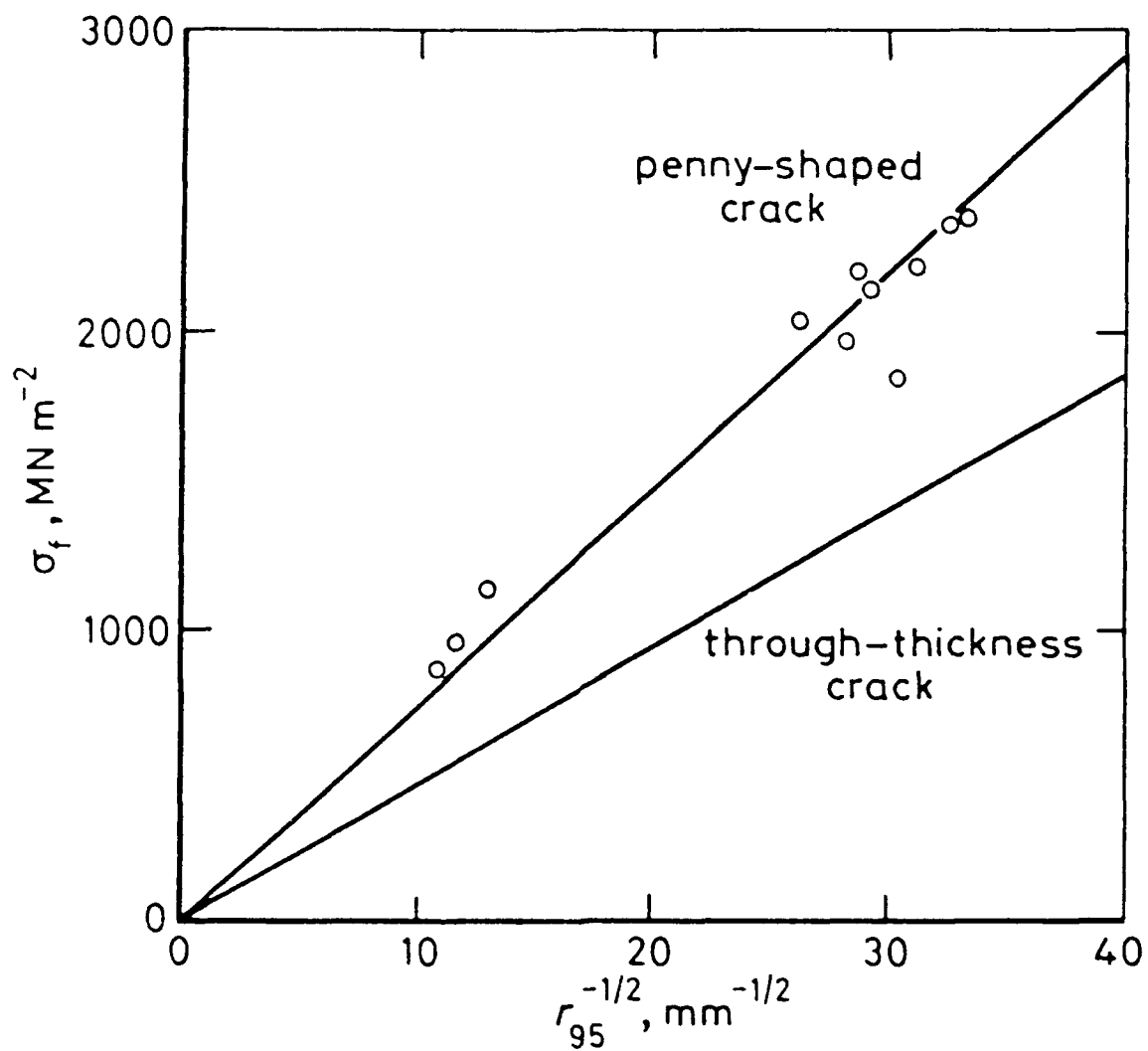
Fig. 14   Variation in critical fracture stress as a function of the 95th percentile carbide radius in mild steel [51].
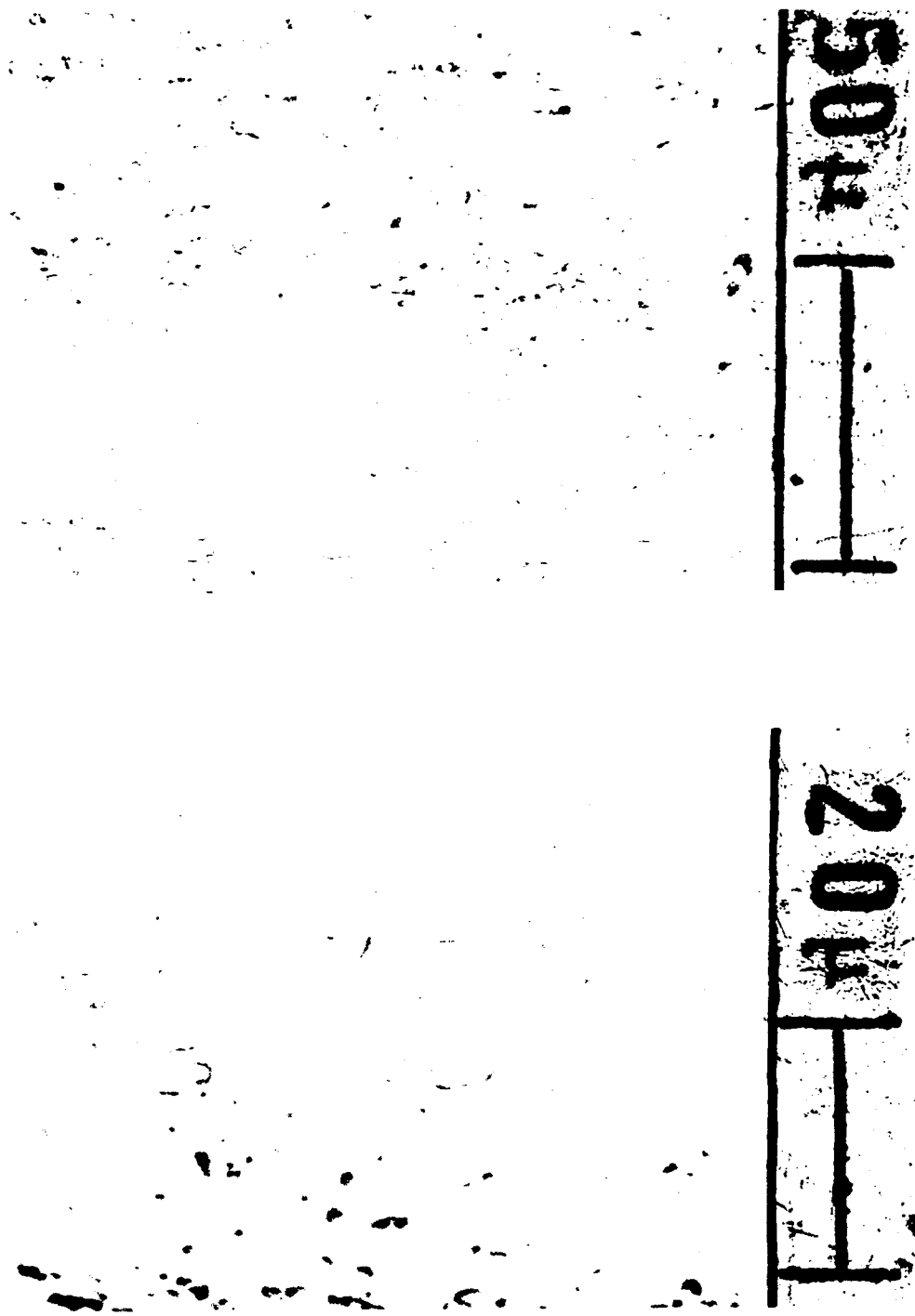
Fig. 15. Photomicrographs of 1.6 Mn–B–Ti steel material GEM. Etched with nital and picral.

100 µ

50 µ
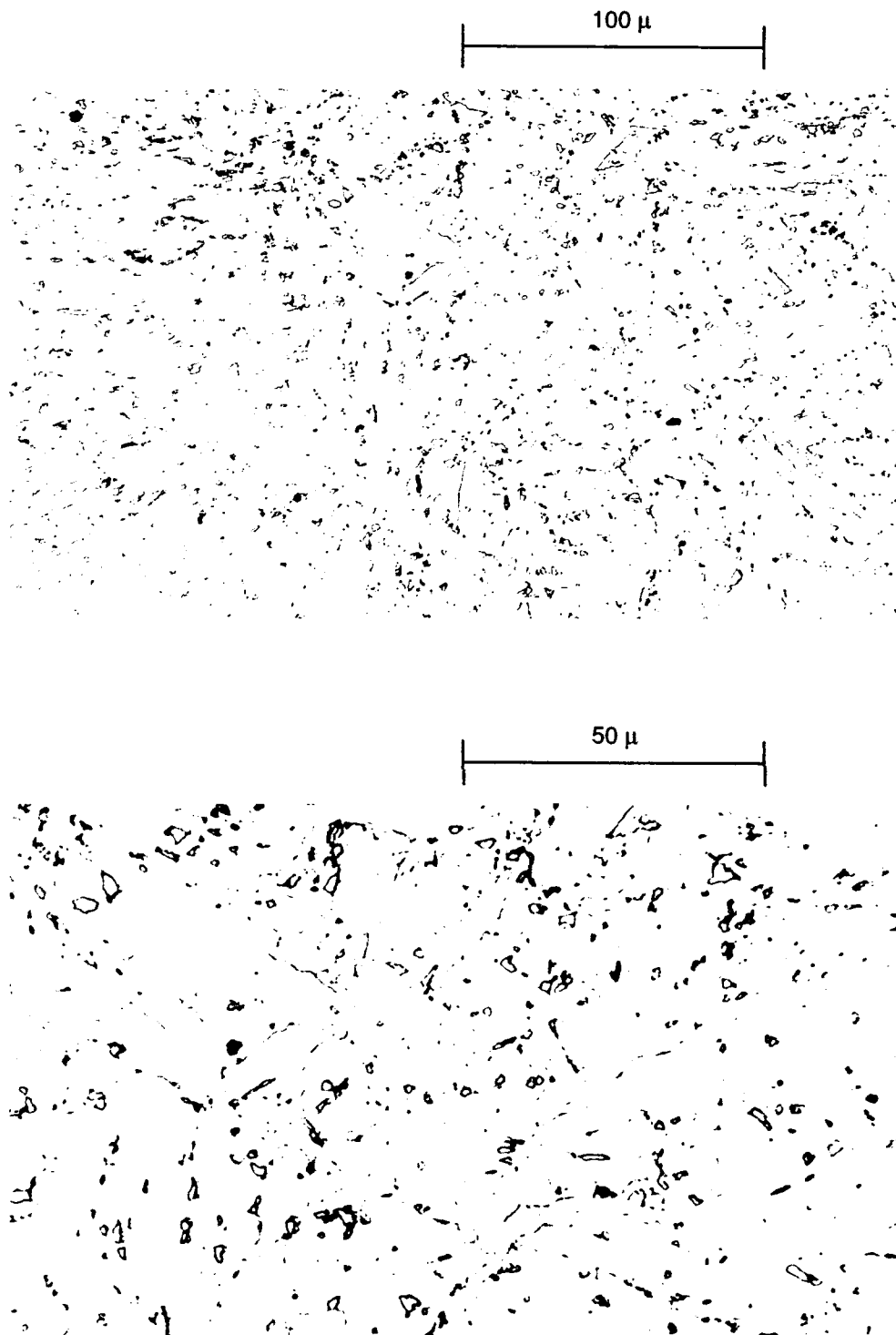
Fig. 16. Photomicrographs of 1.9 Mn–B–Ti material GCZ. Etch with 2% nital.
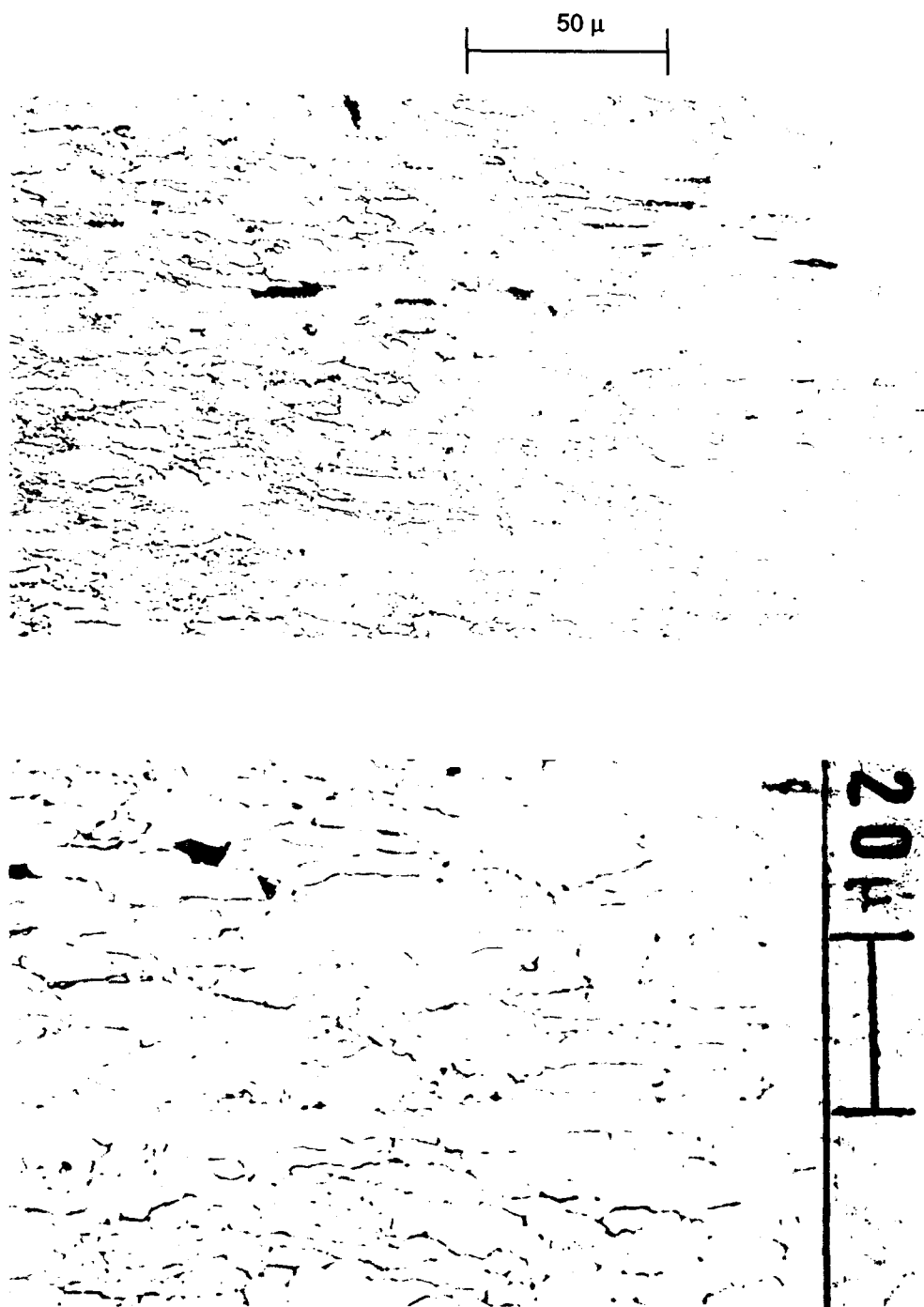
Fig. 17. Photomicrographs of 1 Mn–0.5 Mo–0.5 Ni steel material GHB. Etched with nital and picral.
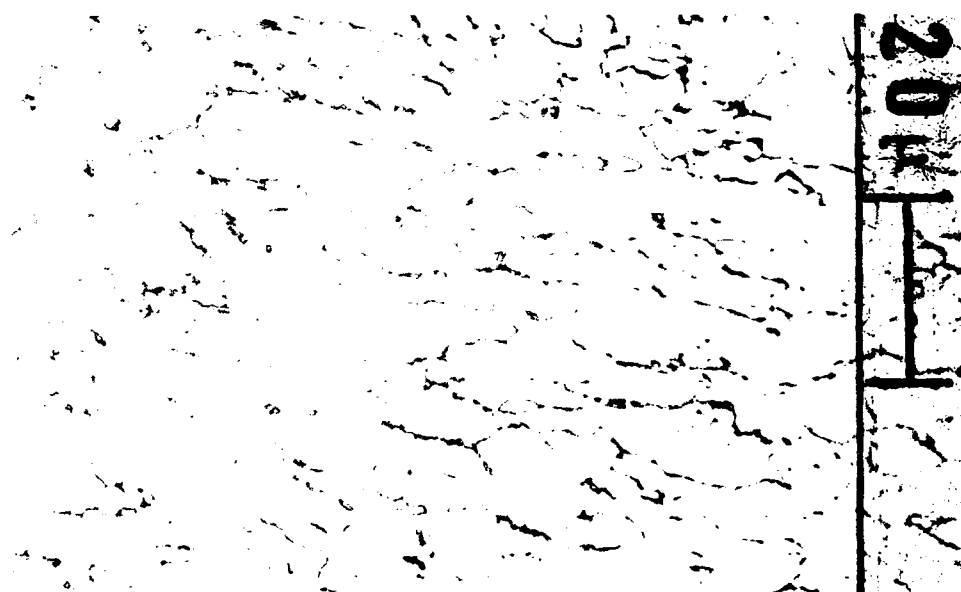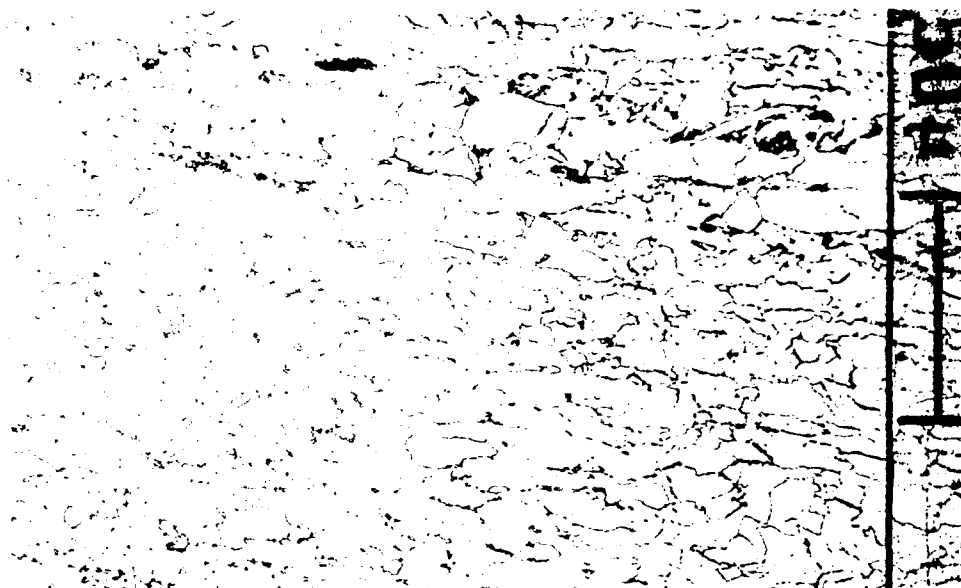
Fig. 18. Photomicrographs of 1 Mn–0.5 Mo–0.5 Ni material GHD. Etched with nital and picral.

Fig. 19.   Photomicrographs of 1 Mn–0.5 Mn–0.5 Ni material GHG. Etched with nital and picral.
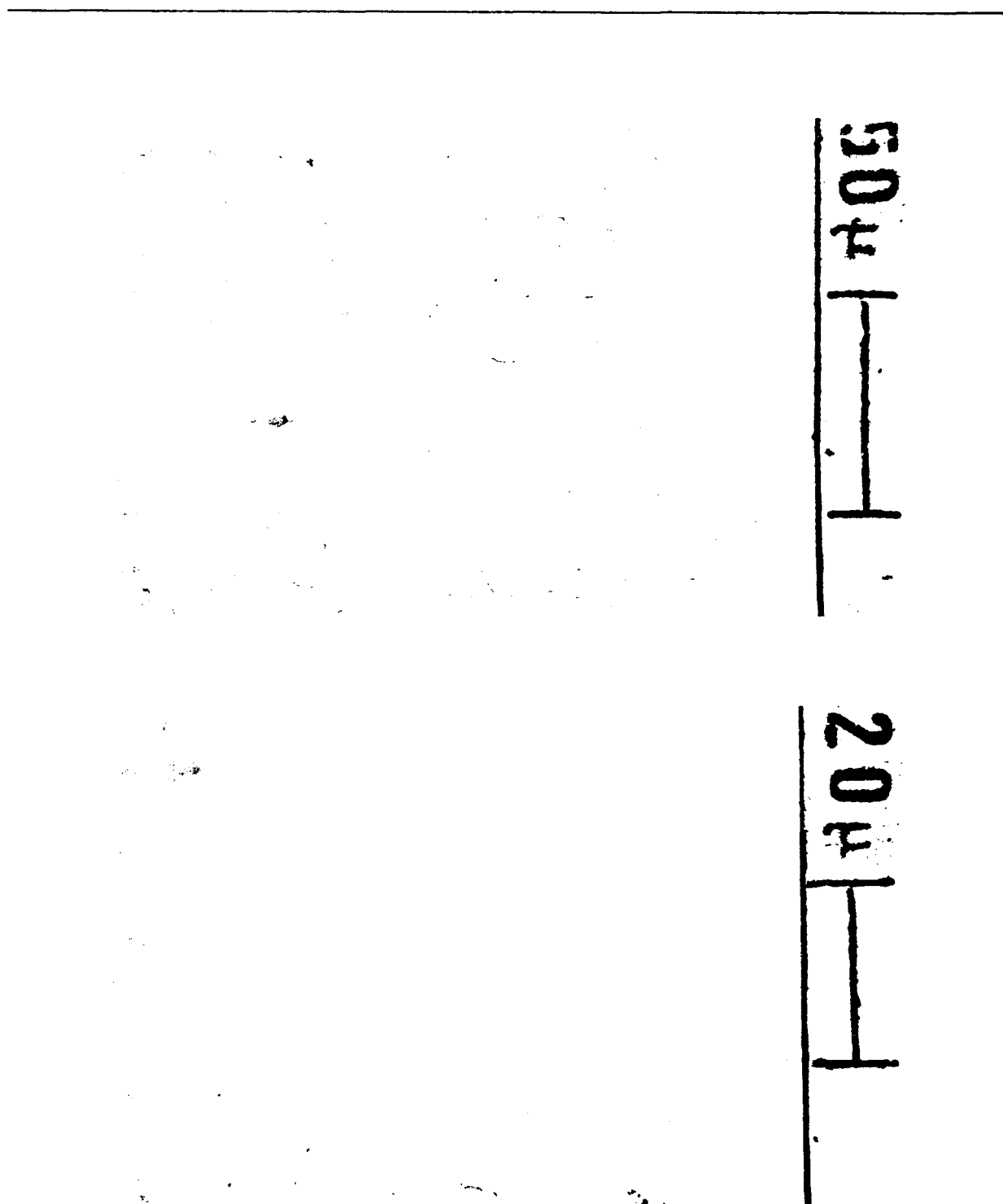
Fig. 20. Photomicrographs of 1 Mn–1 Mo–1 Ni material GHC. Etched with nital and picral.
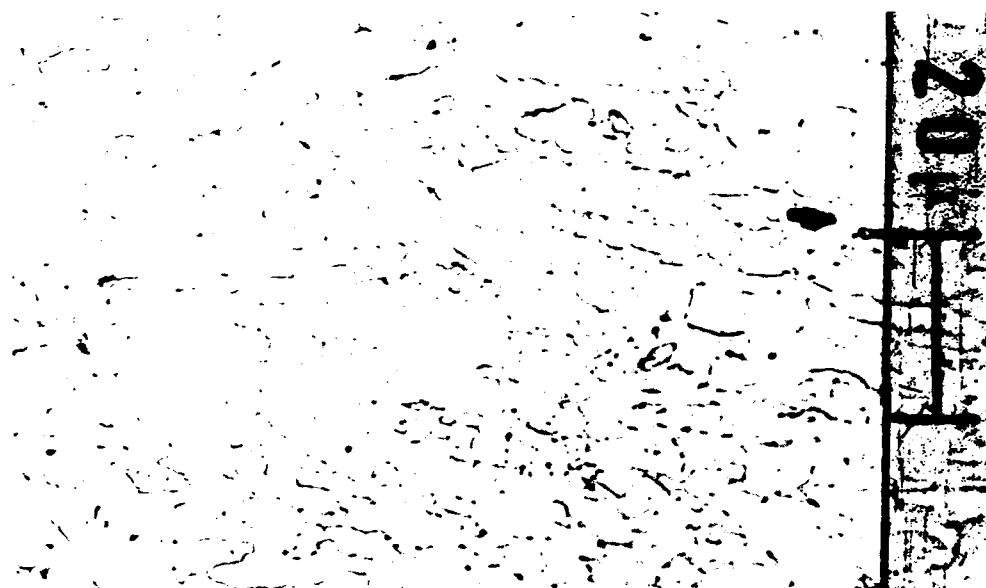
Fig. 21. Photomicrographs of 1 Mn–1 Mo–1 Ni material GHE. Etched with nital and picral.
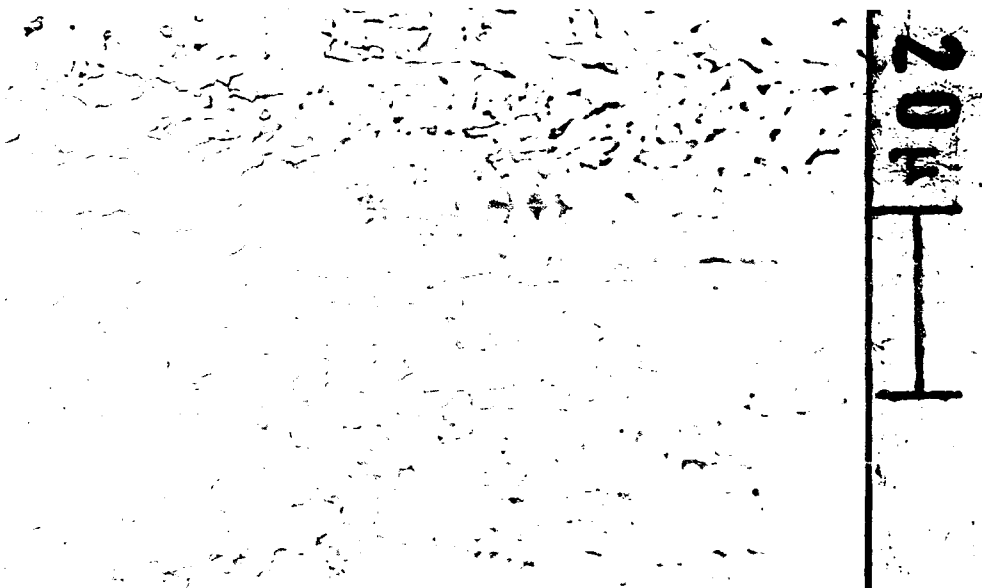
Fig. 22. Photomicrographs of 1 Mn–1 Mo–1 Ni steel material GHH. Etched with nital and picral.

12.7 mm   **> 80 mm**   **12.7 mm**

NOTCH BEND SPECIMEN

10 mm   **6.4 mm**   **22.7 mm**
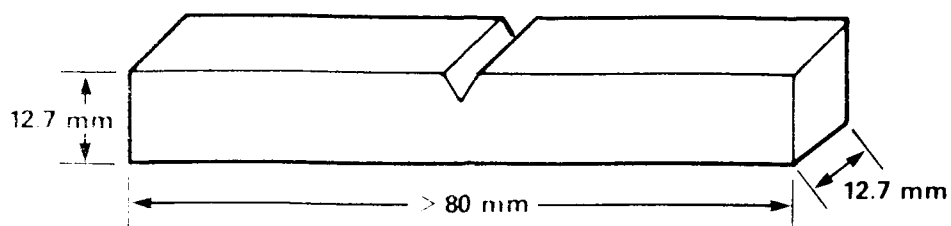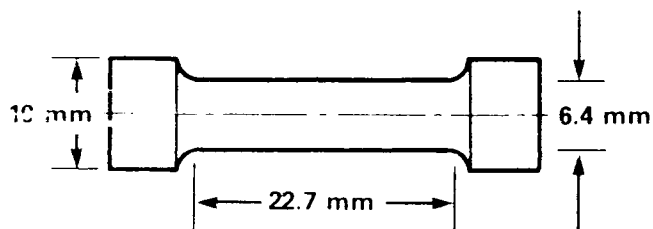
TENSILE SPECIMEN

DRAWING NOT TO SCALE

Fig. 23.   Specimen drawings. Notched bend specimen and tensile specimen.
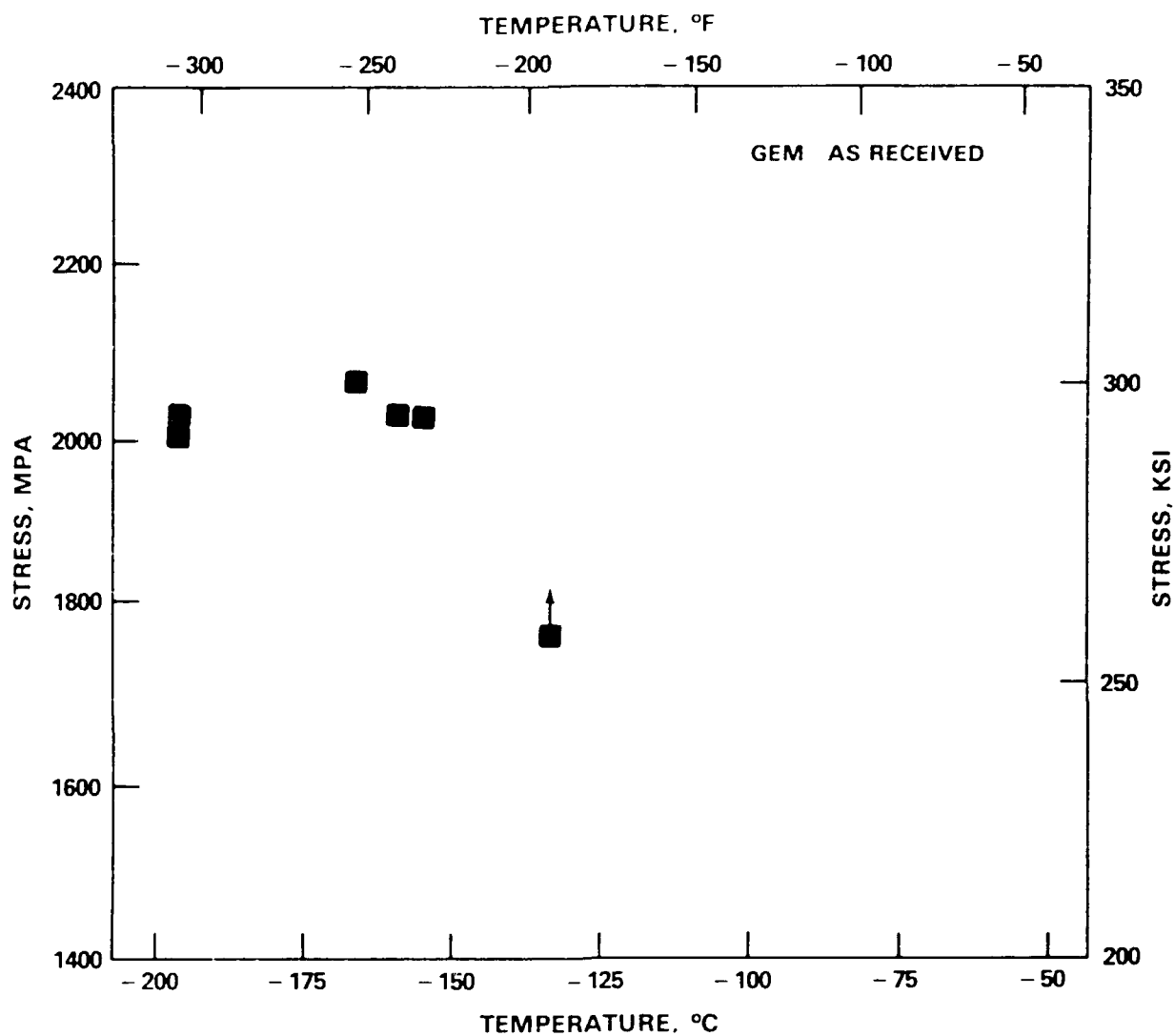
Fig. 24.   Critical fracture stress versus temperature for 1.6 Mn–B–Ti material GEM.

NOTE: Up-pointing arrows indicate
specimens which experienced
net section yielding
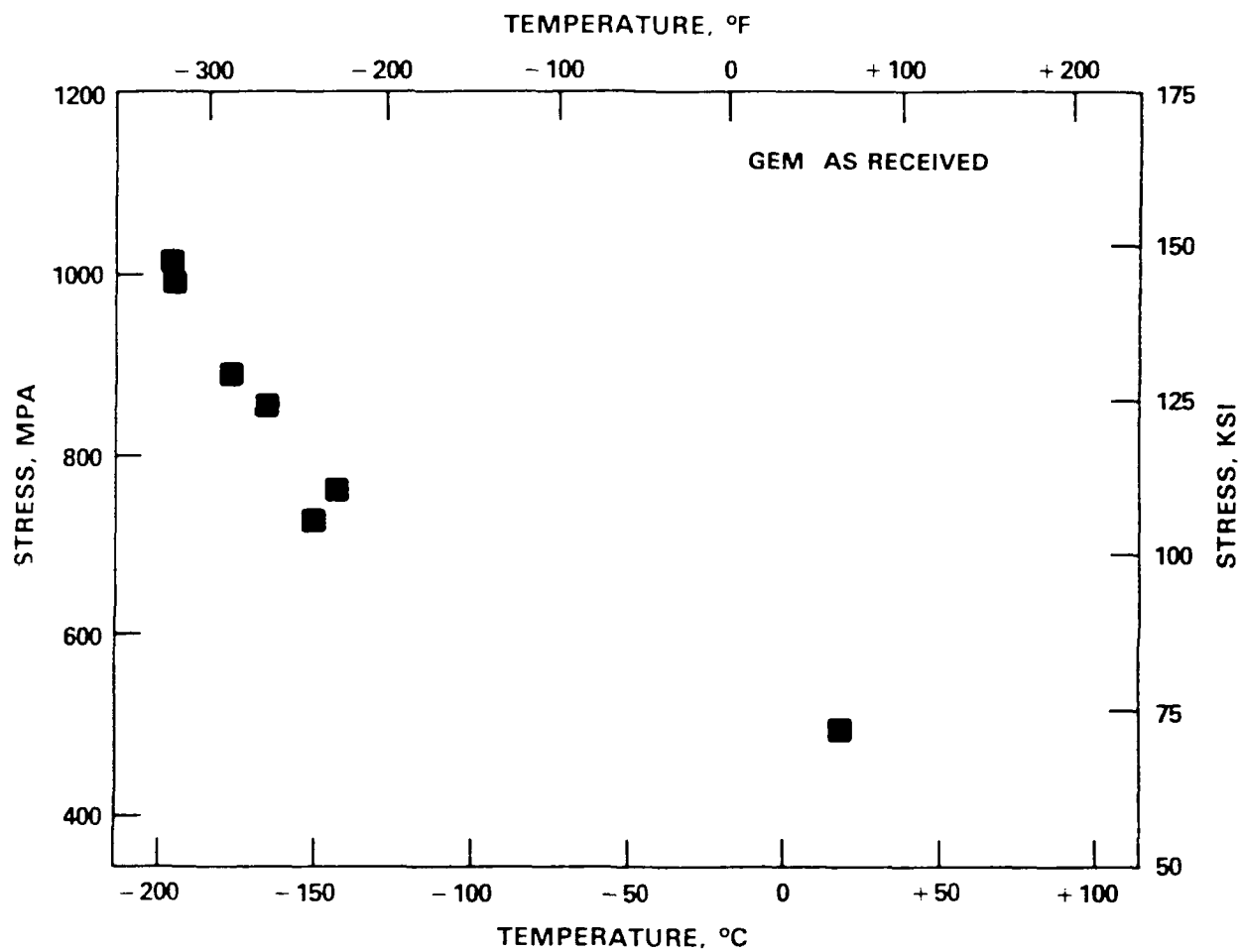
Fig. 25.   Tensile yield strength versus temperature for 1.6 Mn–B–Ti material GEM.
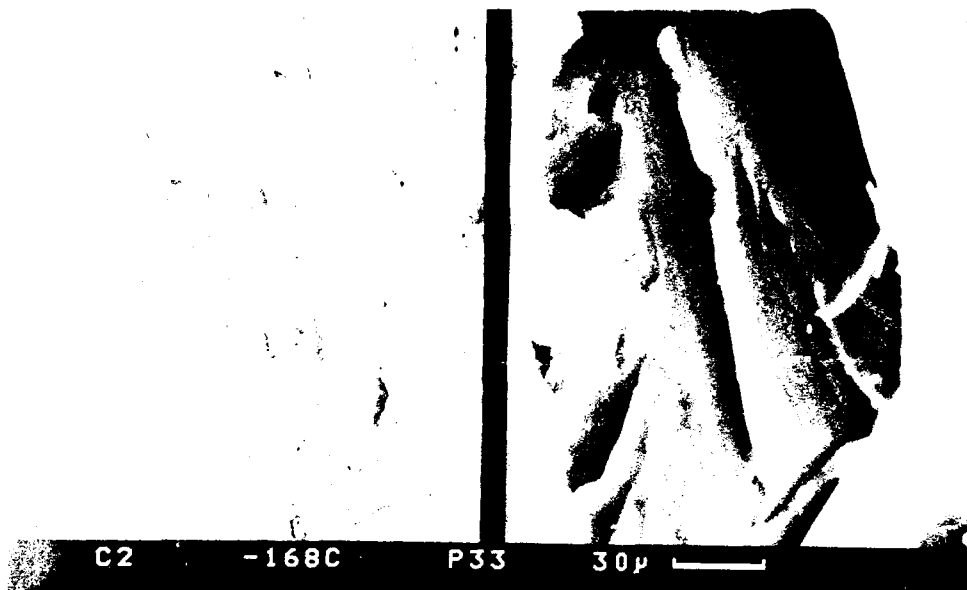
Fig. 26. SEM photograph of the fracture surface of 1.6 Mn–B–Ti material GEM. Photograph on right is area within block on left photograph.
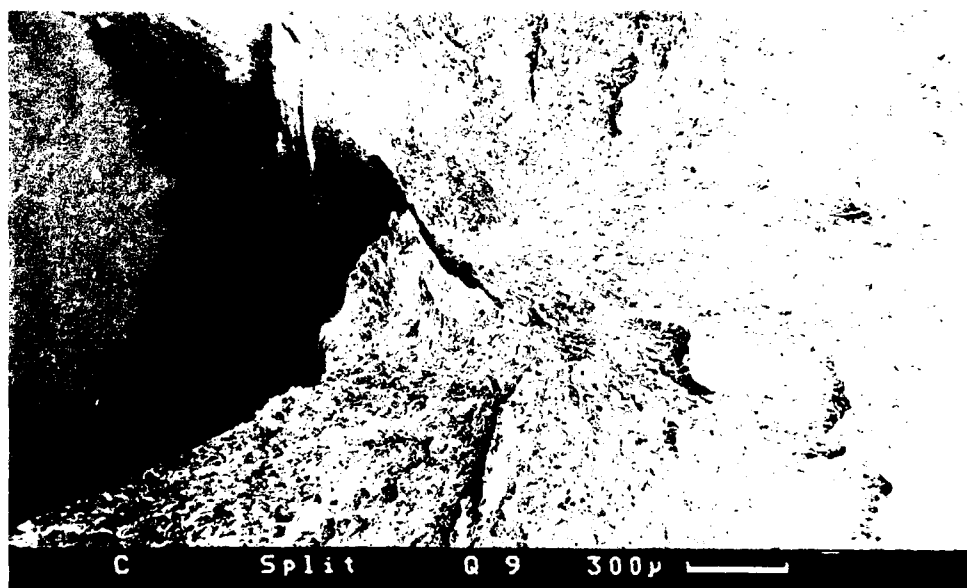
Fig. 27. SEM photograph of a 'split' fracture surface of 1.6 Mn–B–Ti material GEM.
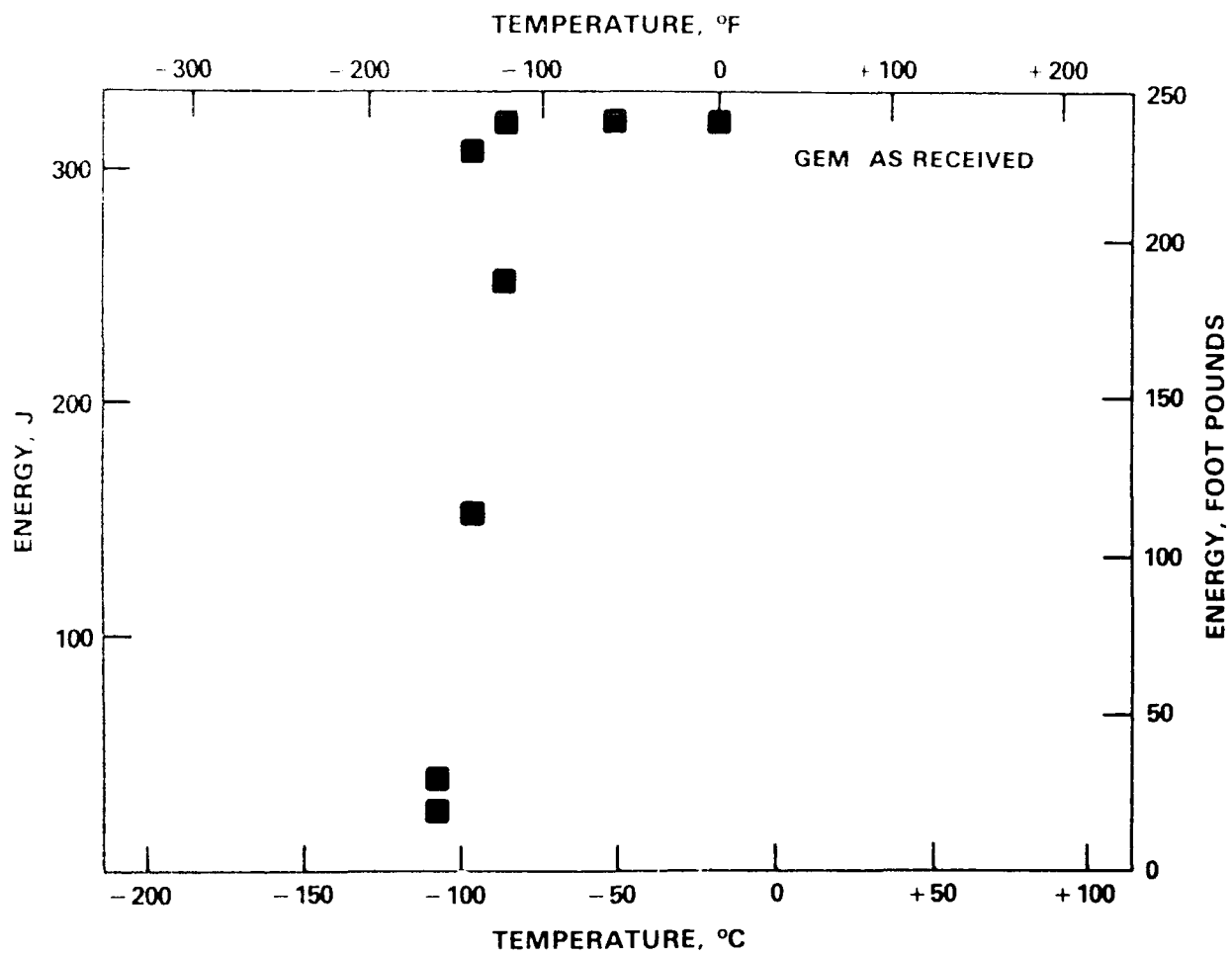
Fig. 28. Charpy impact toughness versus temperature for 1.6 Mn–B–Ti material GEM.

Fig. 29.   Charpy impact toughness versus temperature for 1.6 Mn–B–Ti material GEM
with Gleeble HAZ simulation. Square symbols = GEM as received. Round symbols = GEM
with Gleeble HAZ cycle.
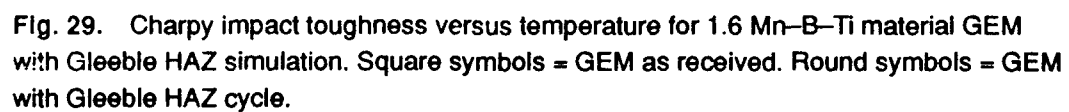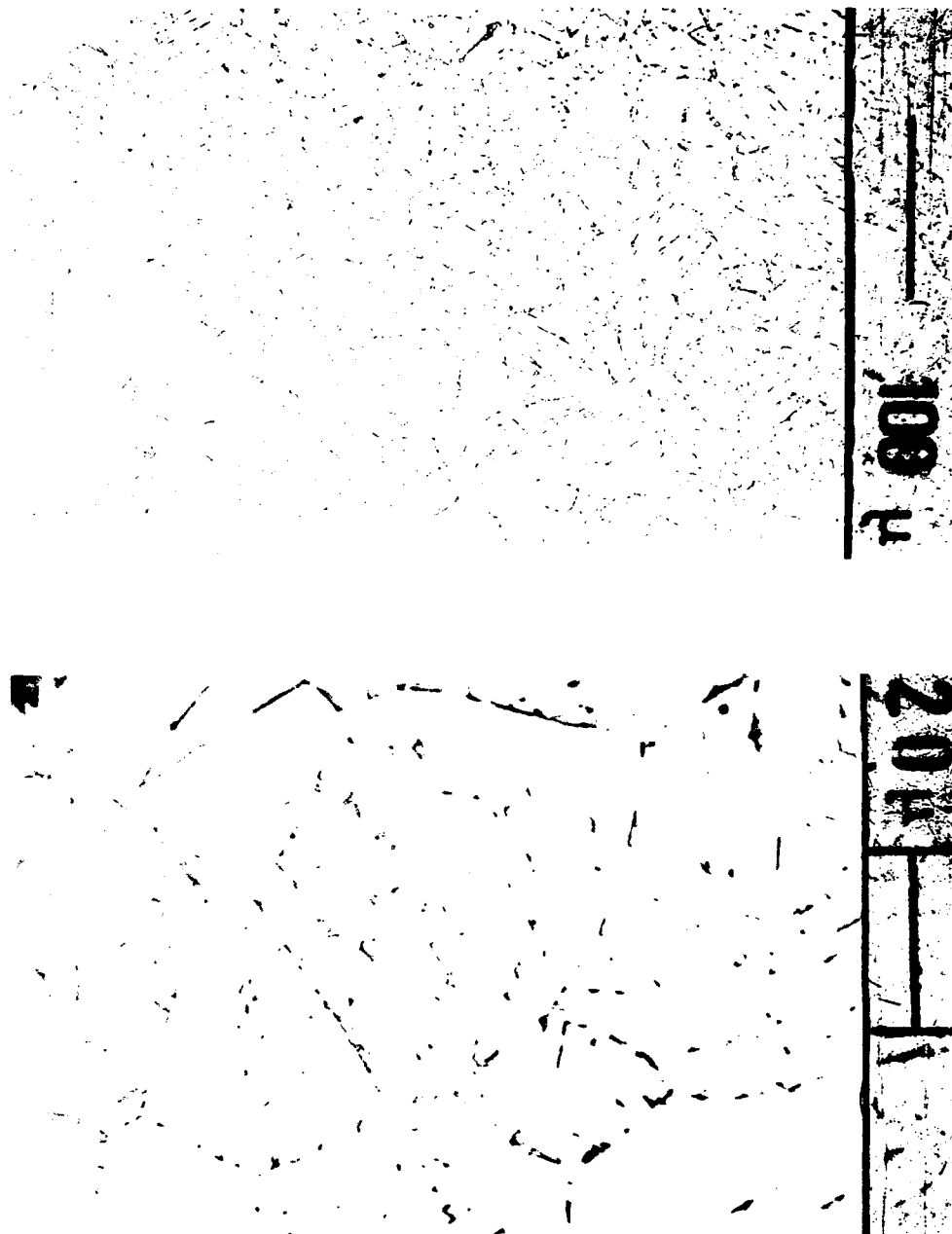
Fig. 30. Photomicrographs of 1.6 Mn–B–Ti material GEM with Gleeble HAZ simulation.
Etched with nital and picral.
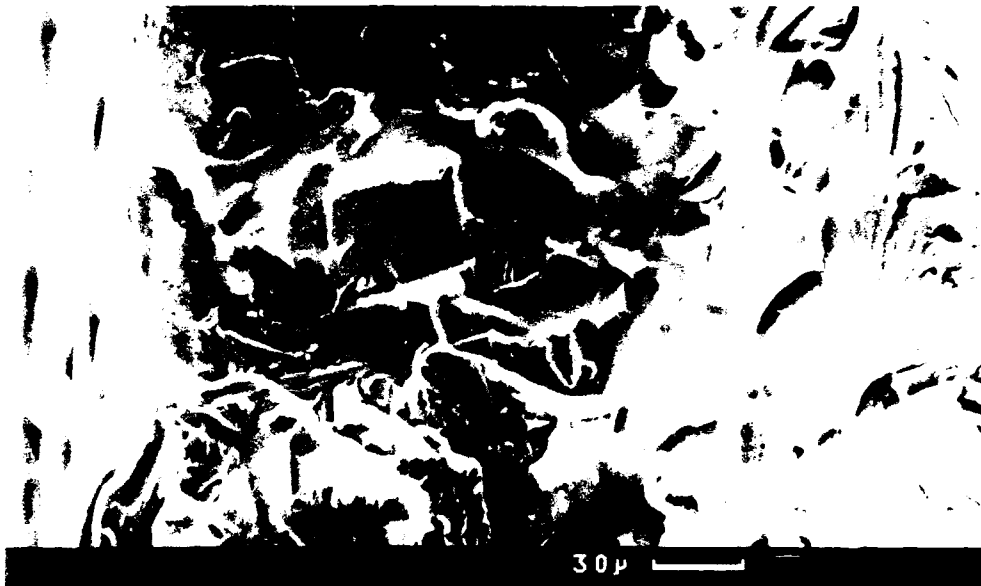
Fig. 31. SEM photograph of the fracture surface of 1.6 Mn–B–Ti material GEM with Gleeble HAZ simulation showing cleavage and secondary cracks.
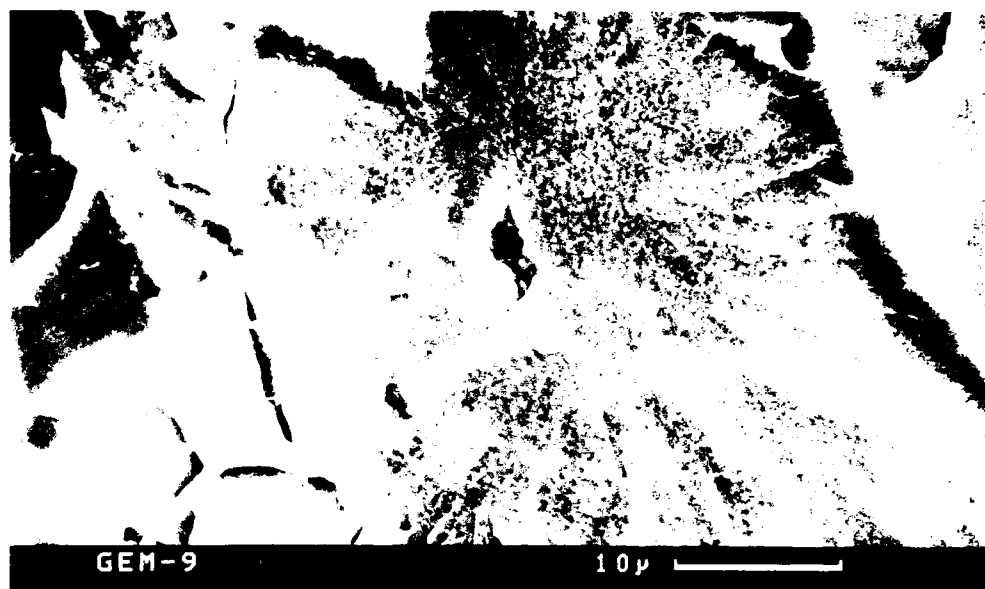
Fig. 32.   SEM photographs of the fracture surface of 1.6 Mn–B–Ti material GEM with
Gleeble HAZ simulation showing cleavage initiation site.
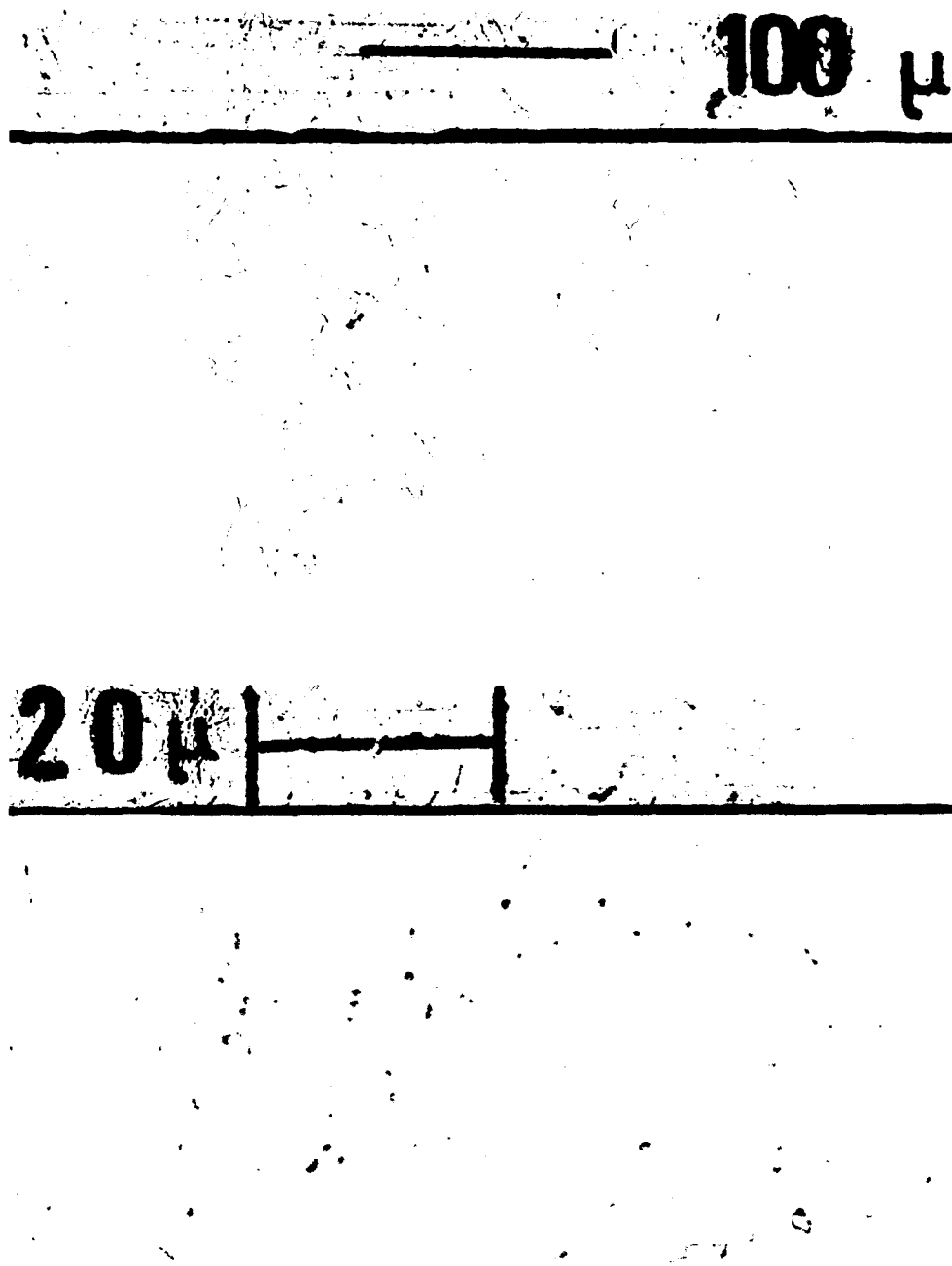
Fig. 33.   Photomicrographs of 1.6 Mn–B–Ti material GEM with a Heat treatment of 25 min. at 1000°C, oil quench, and aged 24 hrs. at 550°C. Etched with nital and picral.
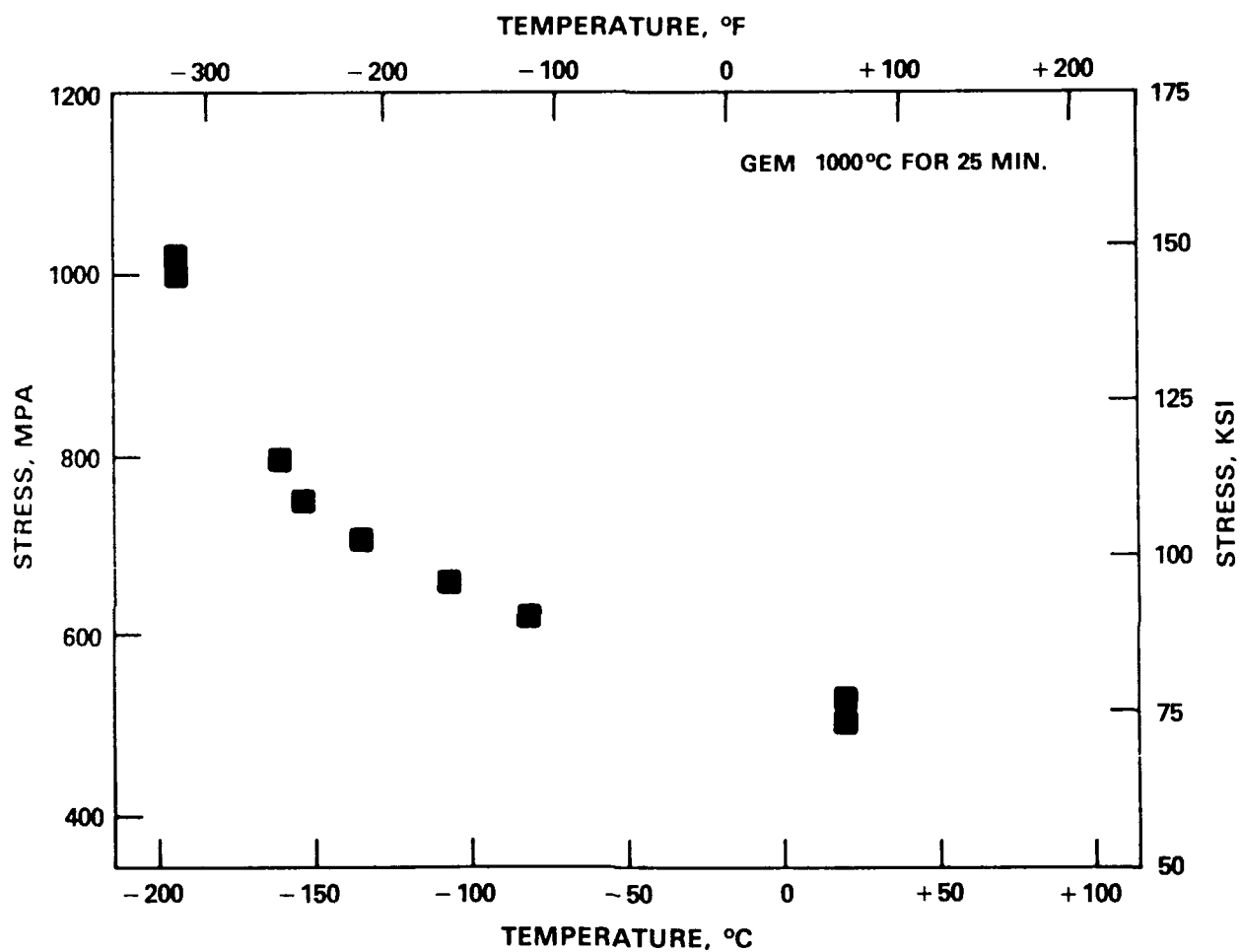
Fig. 34. Tensile yield strength versus temperature for 1.6 Mn–B–Ti material GEM with a heat treatment of 25 min. at 1000°C, oil quench, and aged 24 hrs. at 550°C.
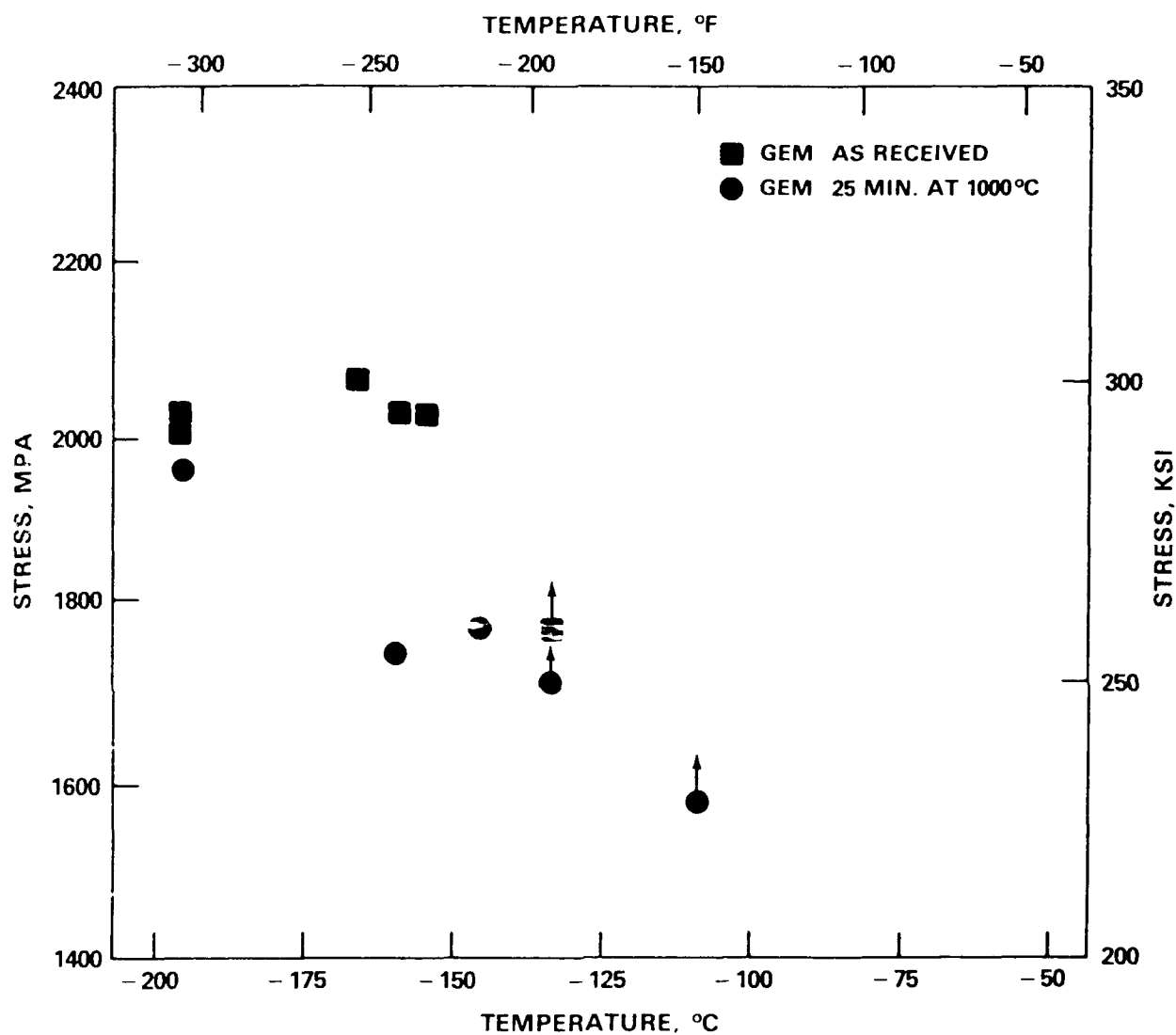
Fig. 35. Critical fracture stress versus temperature for 1.6 Mn–B–Ti material GEM with a heat treatment of 25 min. at 1000°C, oil quench, and aged 24 hrs. at 550°C.
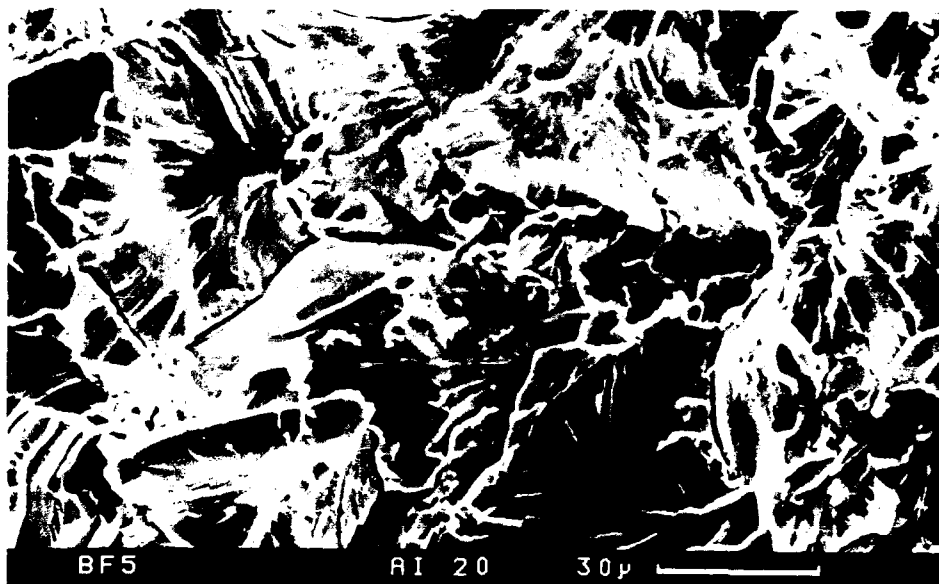
Fig. 36.   SEM photographs of 1.6 Mn–B–Ti material GEM with a heat treatment of
25 min. at 1000°C, showing cleavage fracture and secondary cracking.
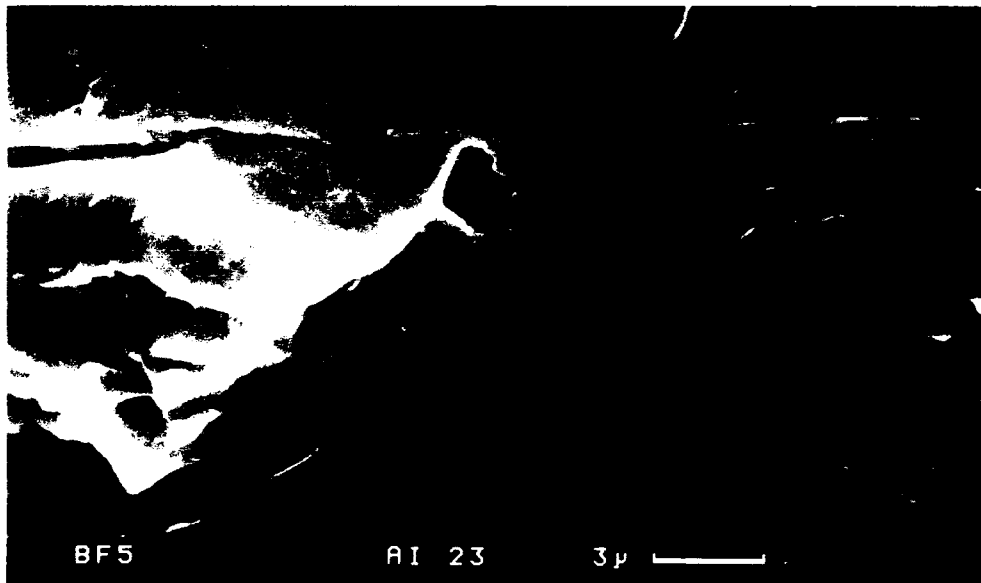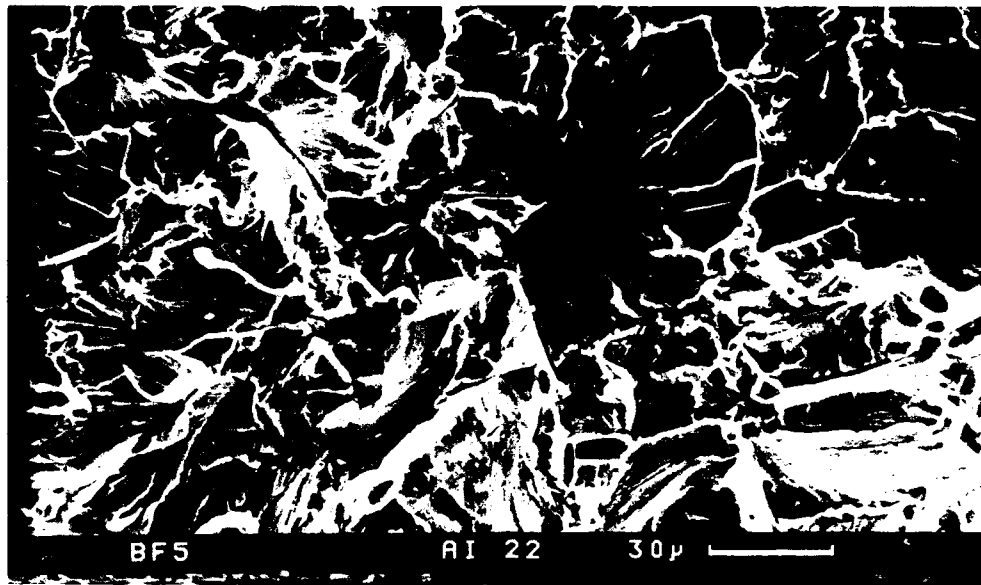
Fig. 37. SEM photographs of 1.6 Mn–B–Ti material GEM with a heat treatment of 25 min. at 1000°C, showing cleavage initiation site.
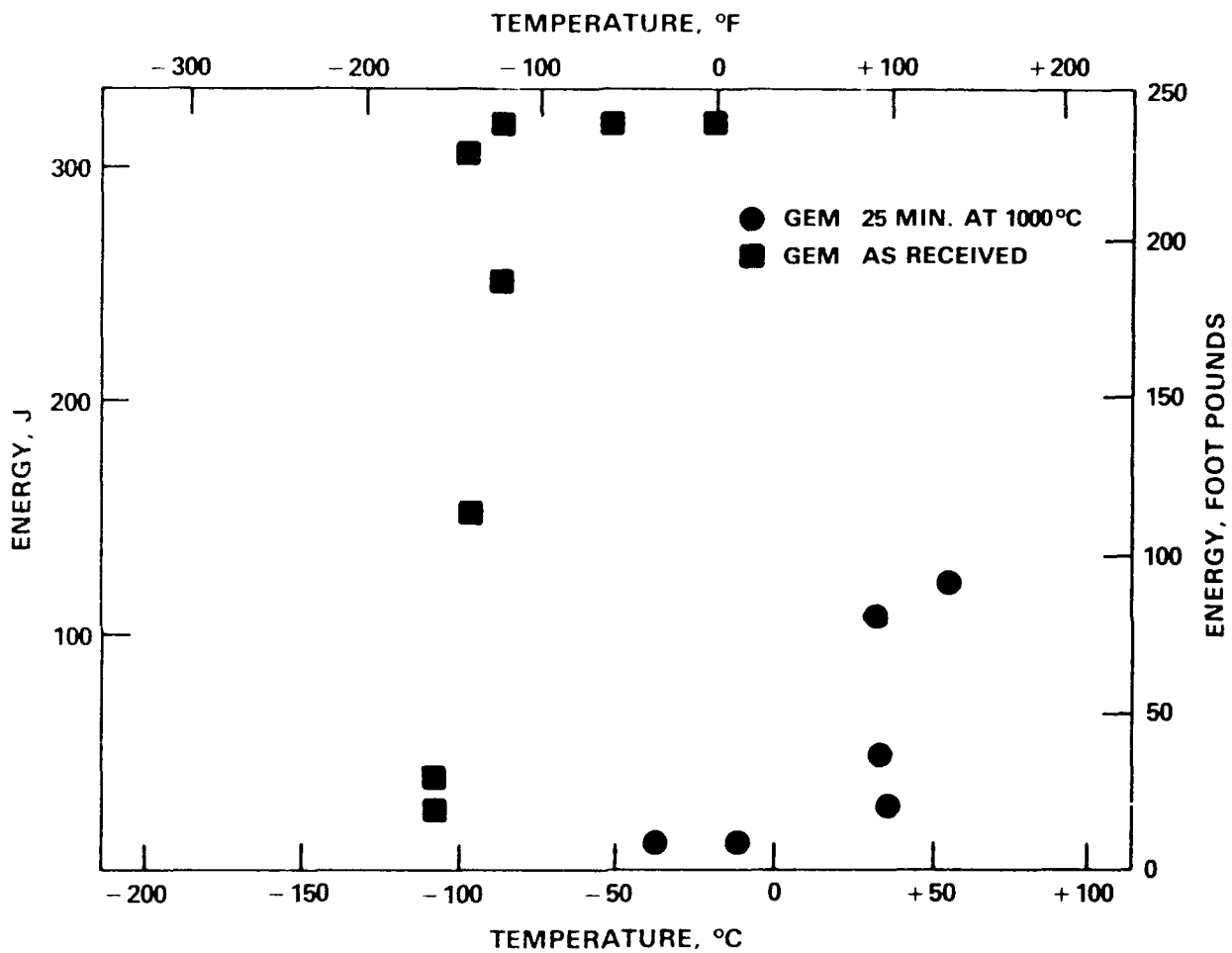
Fig. 38.   Charpy energy versus temperature for 1.6 Mn–B–Ti material GEM with a heat treatment of 25 min. at 1000°C, oil quench, and aged 24 hrs. at 550°C.
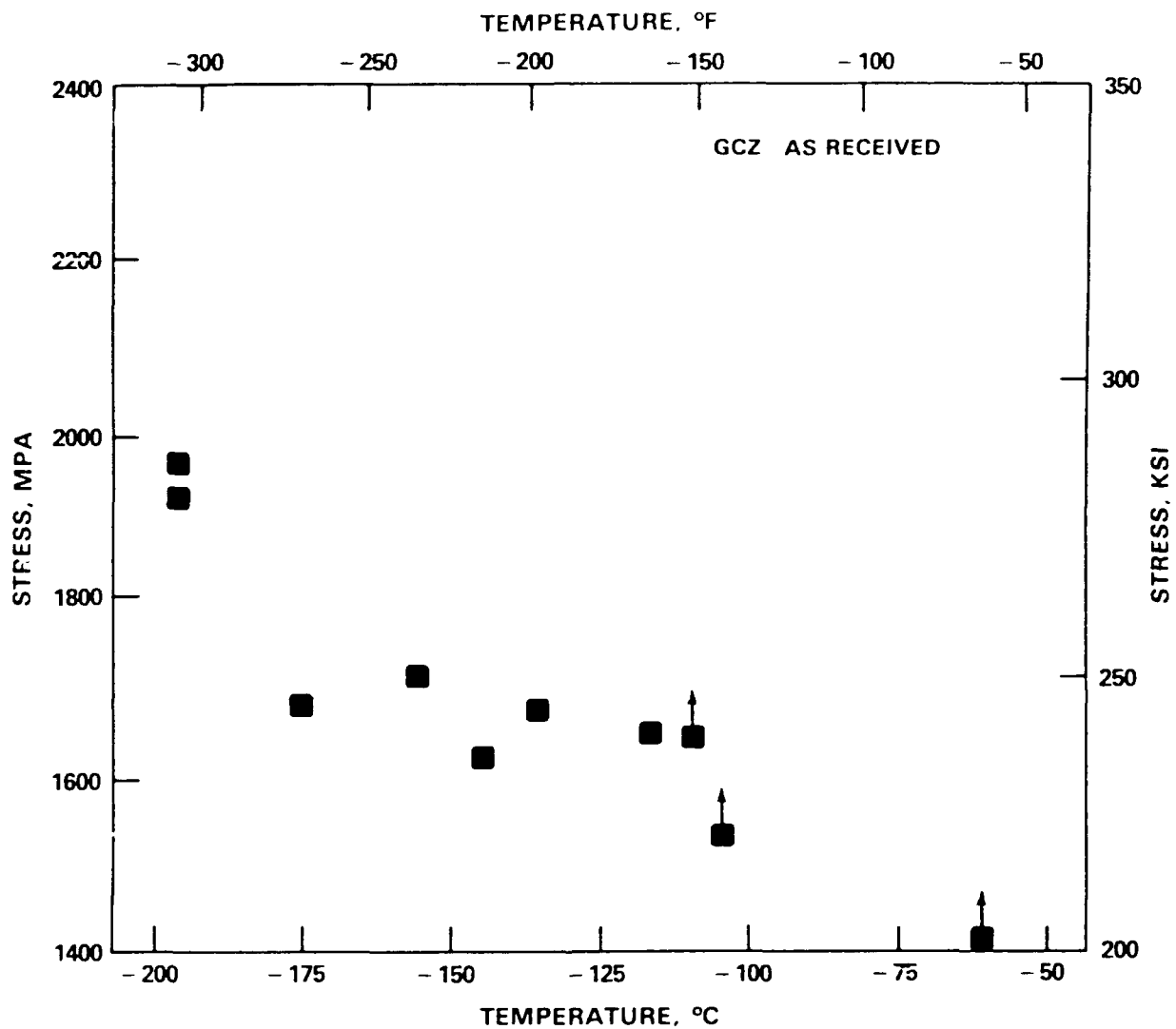
Fig. 39.   Fracture stress measurements versus temperature for 1.9 Mn–B–Ti material GCZ.

NOTE: Up-pointing arrows indicate
specimens which experienced
net section yielding
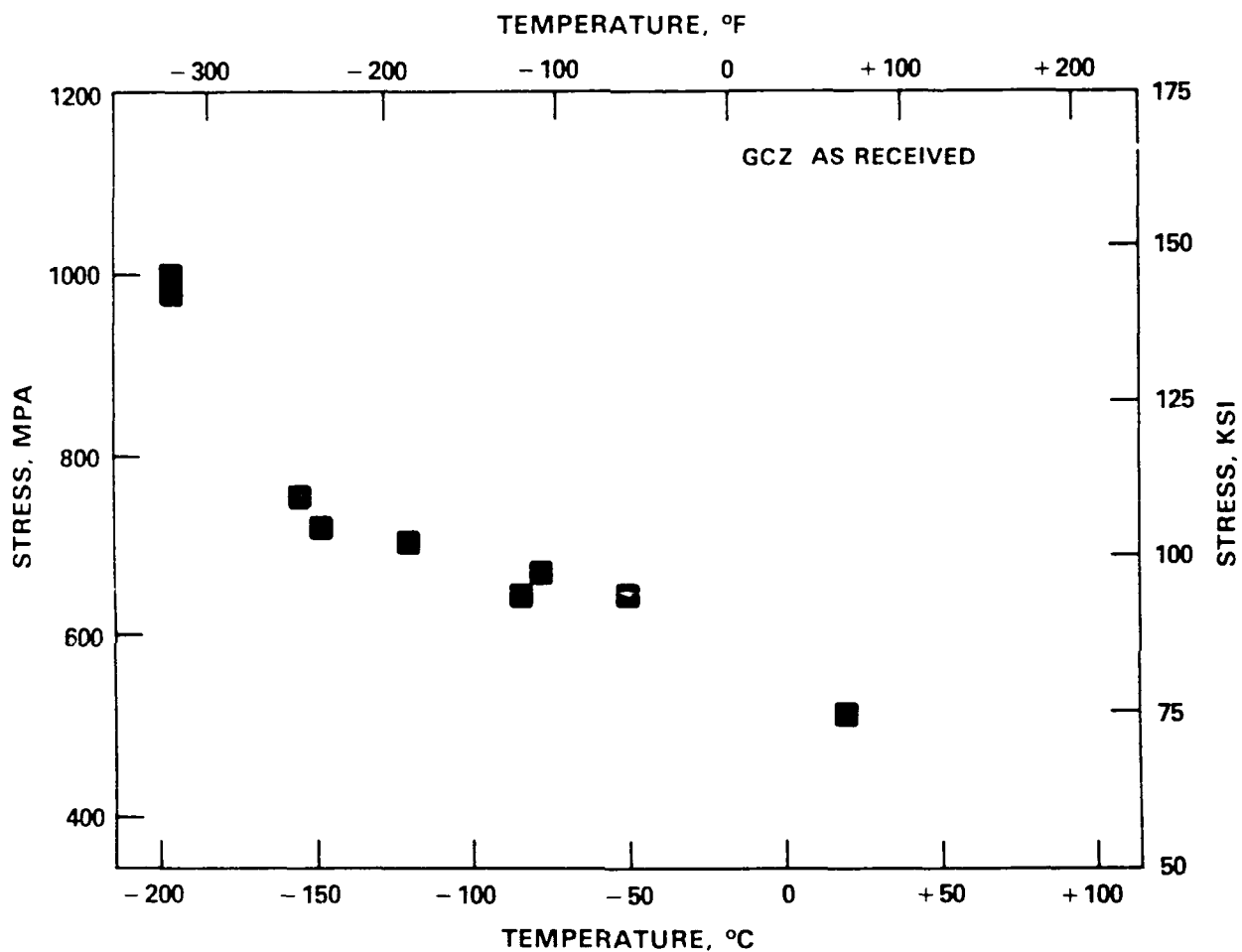
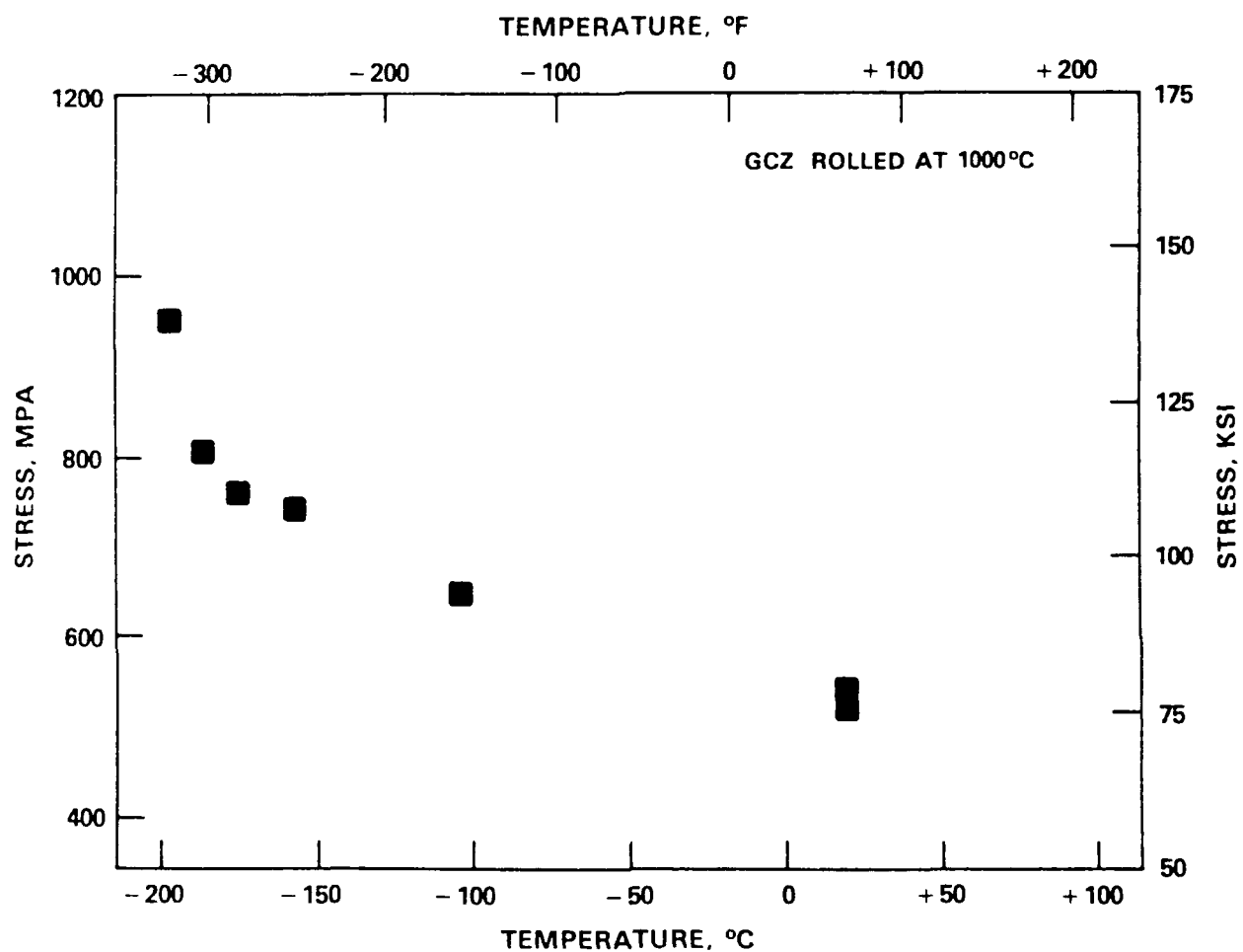Fig. 40.   Yield strength versus temperature results for 1.9 Mn–B–Ti material GCZ.

Fig. 41. Charpy impact energy versus temperature for 1.9 Mn–B–Ti material GCZ.

Fig. 42. Fracture stress measurements versus temperature for 1.9 Mn–B–Ti material GCZ.
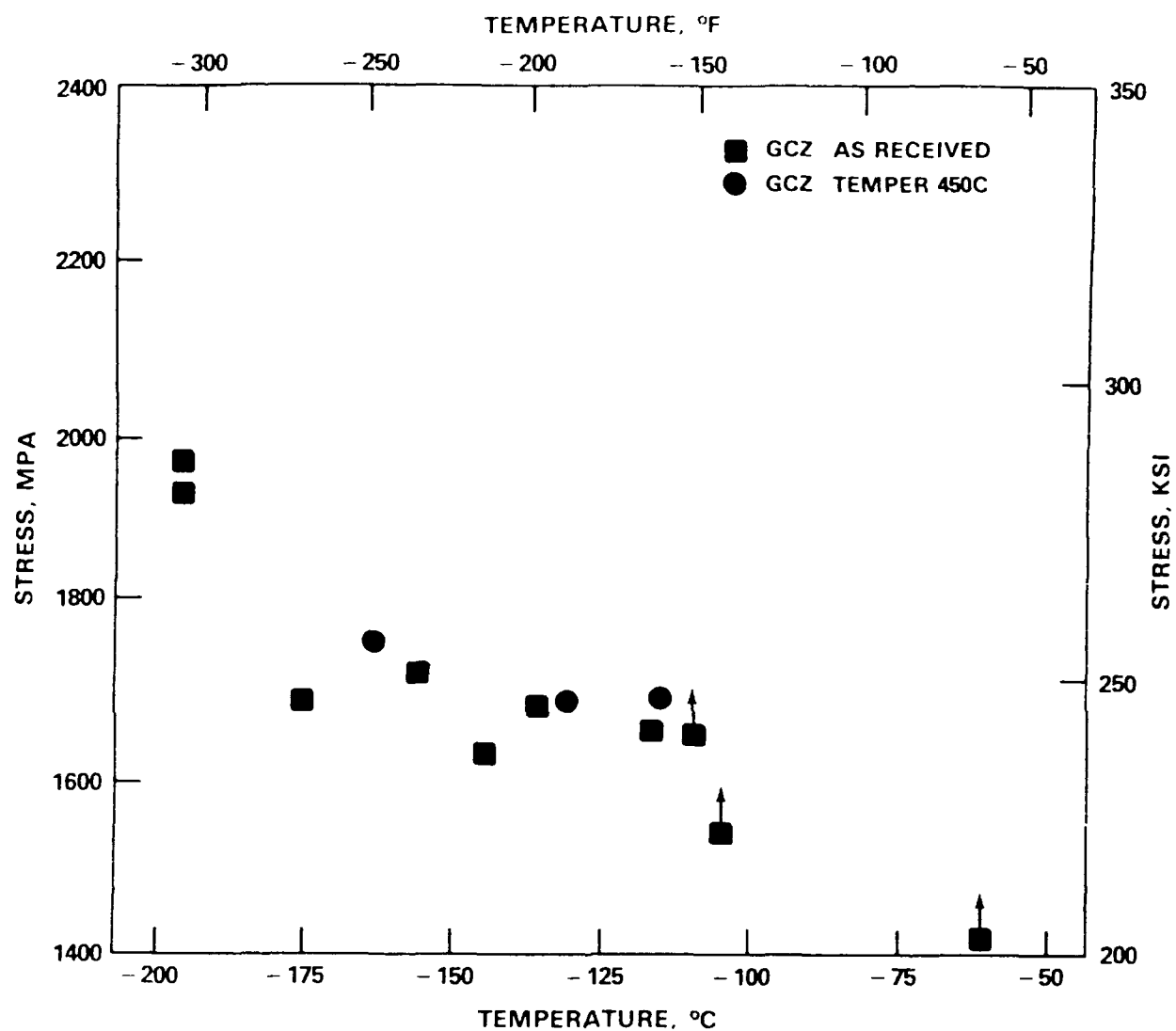
Fig. 43.   Fracture stress measurements versus temperature for 1.9 Mn–B–Ti material GZC.
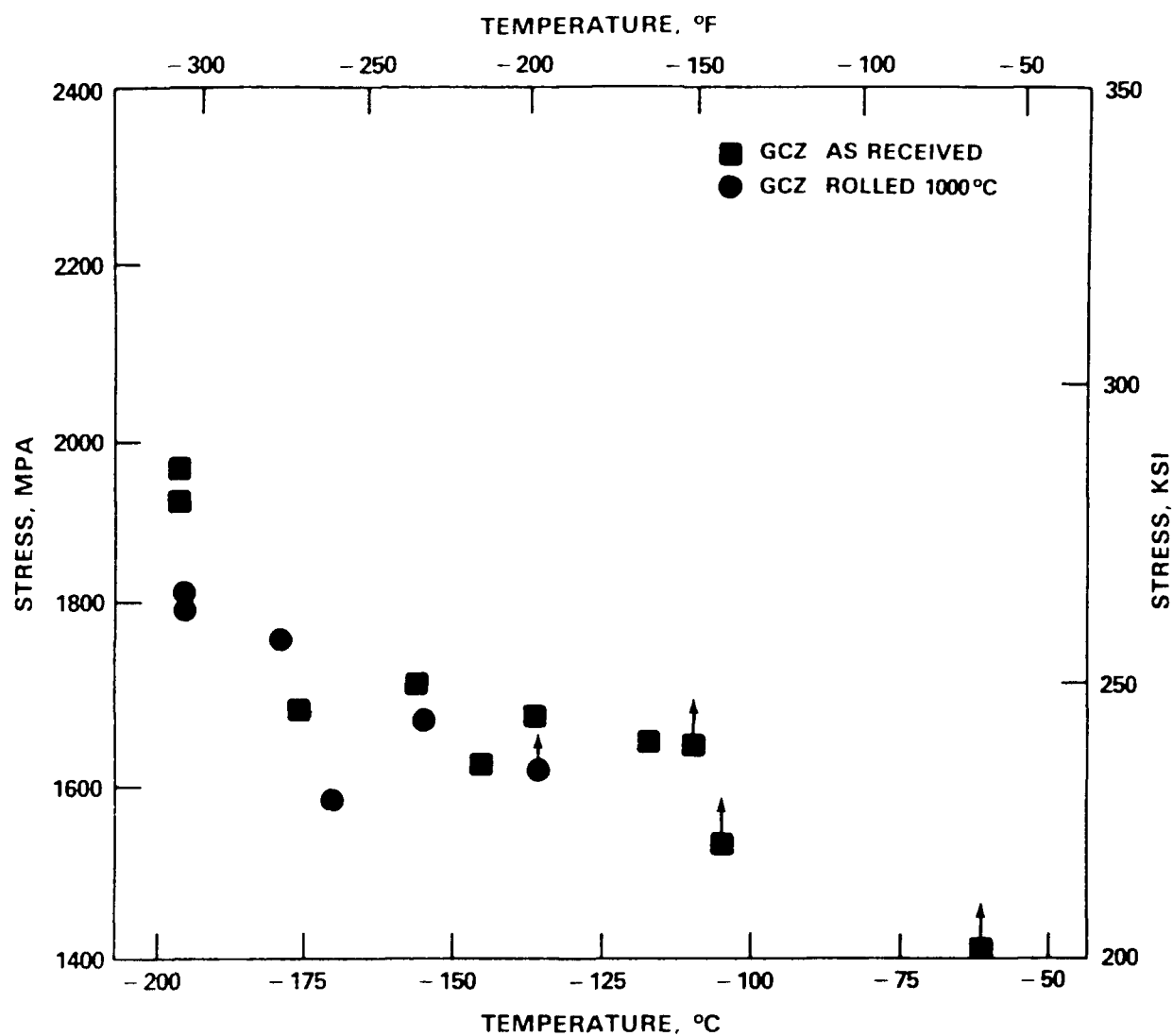
NOTE: Up-pointing arrows indicate
       specimens which experienced
       net section yielding

Fig. 44.   Fracture stress measurements versus temperature for 1.9 Mn–B–Ti material GZC.

Fig. 45. Yield strength versus temperature results for 1.9 Mn–B–Ti material GCZ rolled at 1000°C.
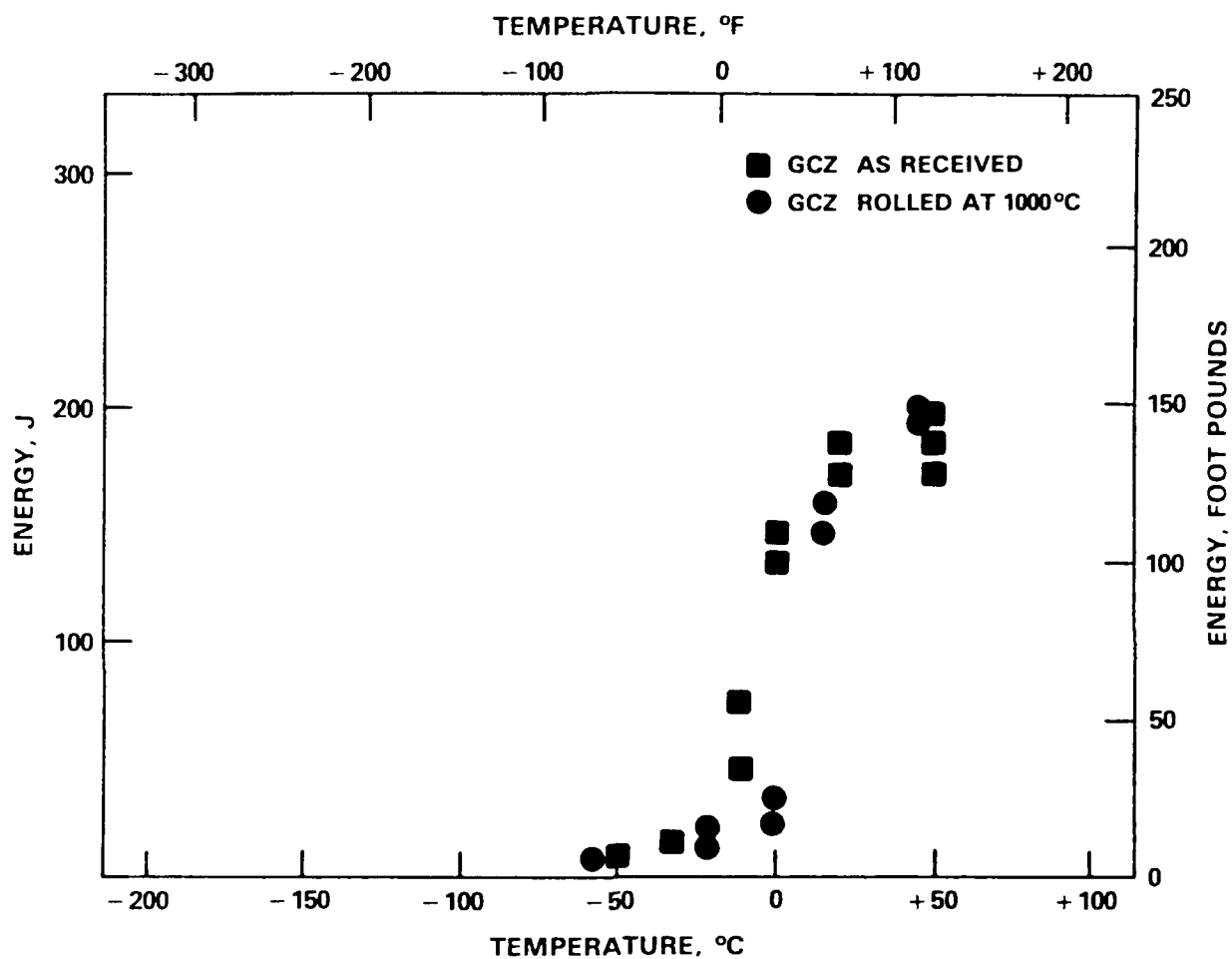
Fig. 46.   Charpy impact toughness results versus temperature for 1.9 Mn–B–Ti material GCZ.
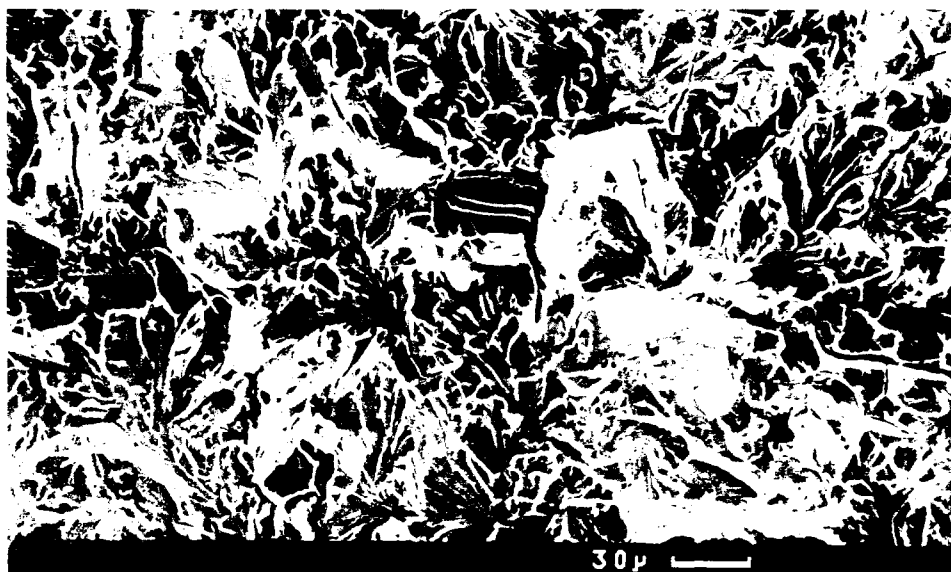
Fig. 47.   SEM photograph of the fracture surface of 1.9 Mn–B–Ti material GCZ showing cleavage facets and some intergranular cracking (arrows).
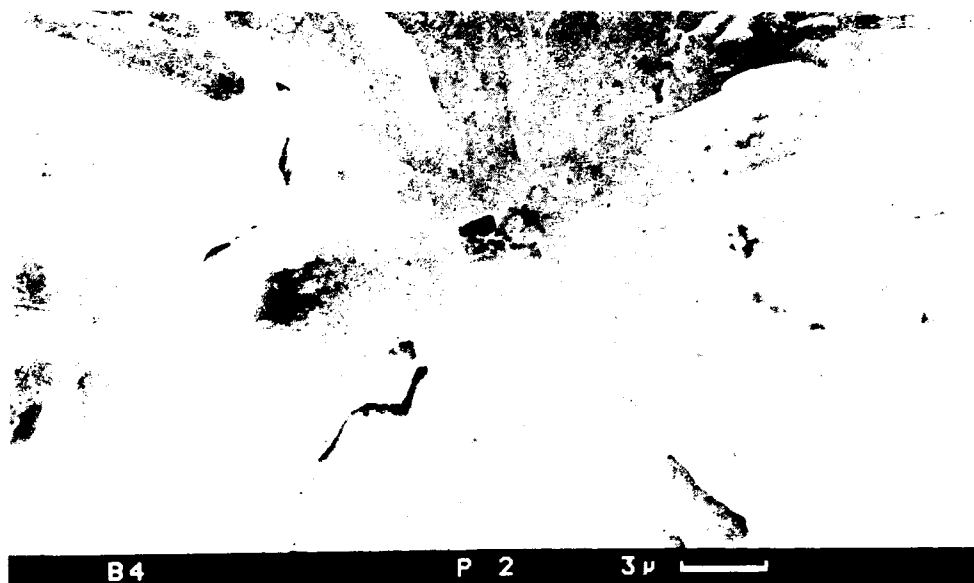
Fig. 48.   SEM photographs showing cleavage initiation site and TiN cube on fracture surface
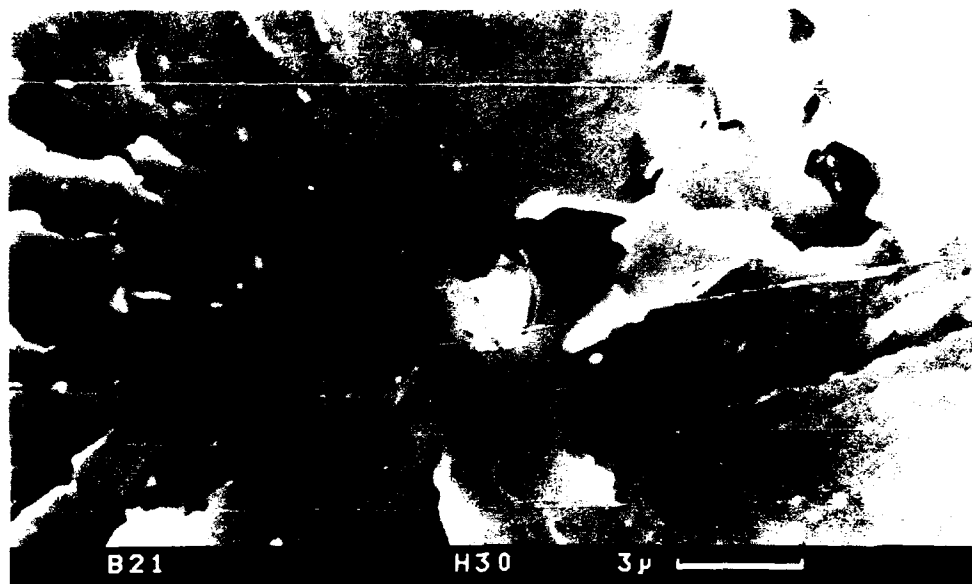of 1.9 Mn–B–Ti material GCZ.

Fig. 49.   SEM photograph of fracture surface of 1.9 Mn–B–Ti material GCZ showing
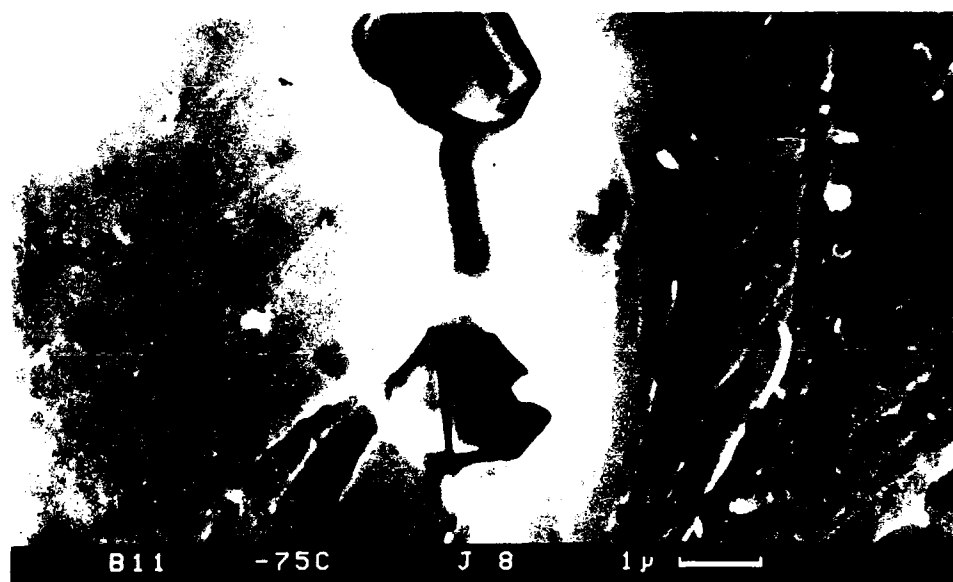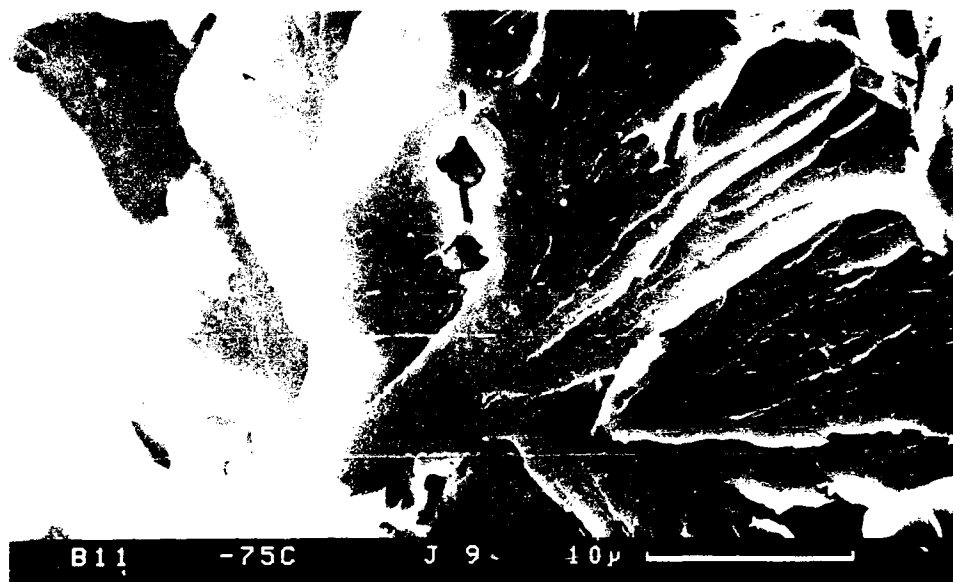a cubic hole and MnS inclusion.

Fig. 50.   SEM photographs of fracture surface of 1.9 Mn–B–Ti material GCZ showing inclusions.
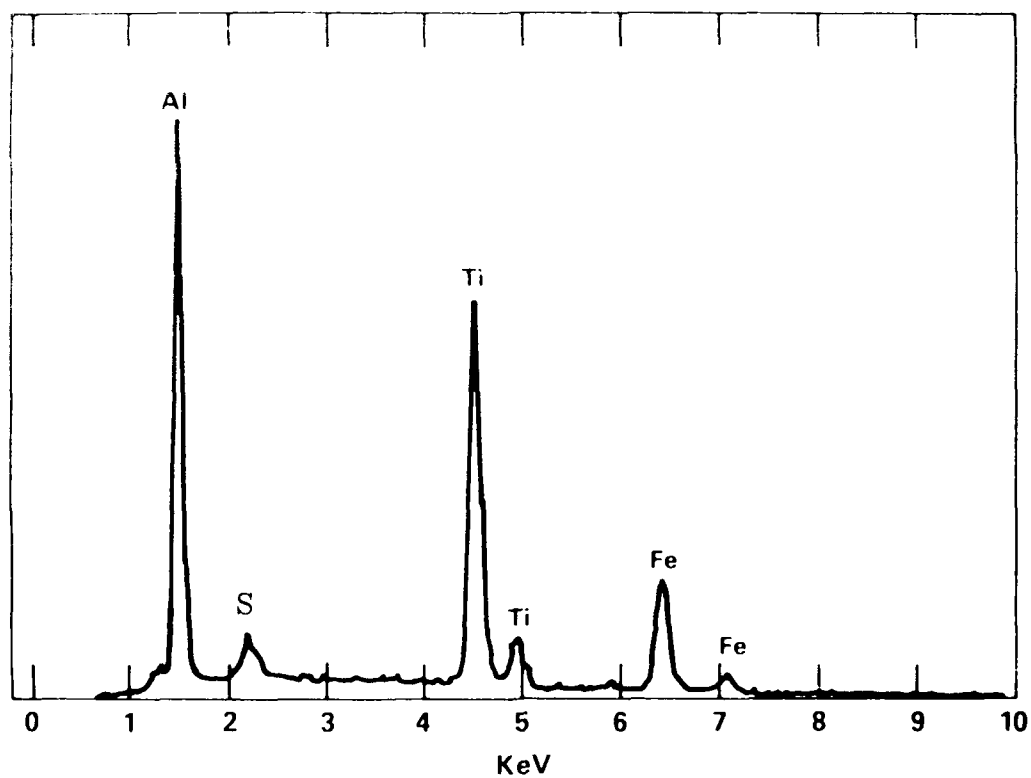
Fig. 51. SEM photograph and EDS results of TiN cube on fracture surface of 1.9 Mn–B–Ti material GCZ. Mating area to Fig. 52.
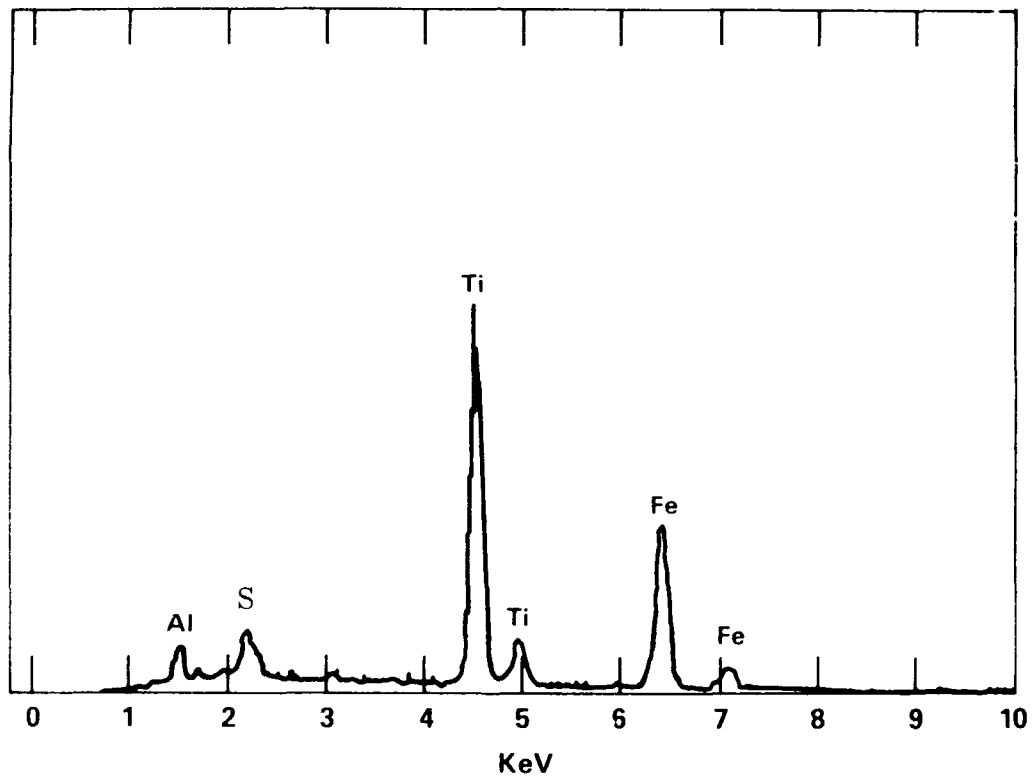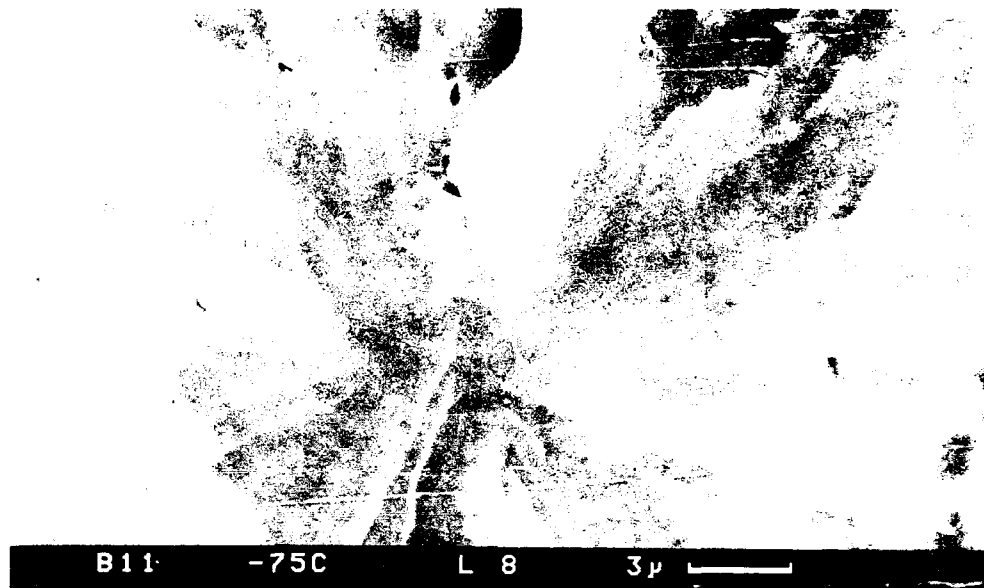
Fig. 52. SEM photograph and EDS results of TiN cube on fracture surface of 1.9 Mn–B–Ti material GCZ. Mating area to Fig. 51.

Fig. 53. SEM photograph using normal and back scattered mode of a TiN cube in a fracture surface of 1.9 Mn–B–Ti material GCZ.
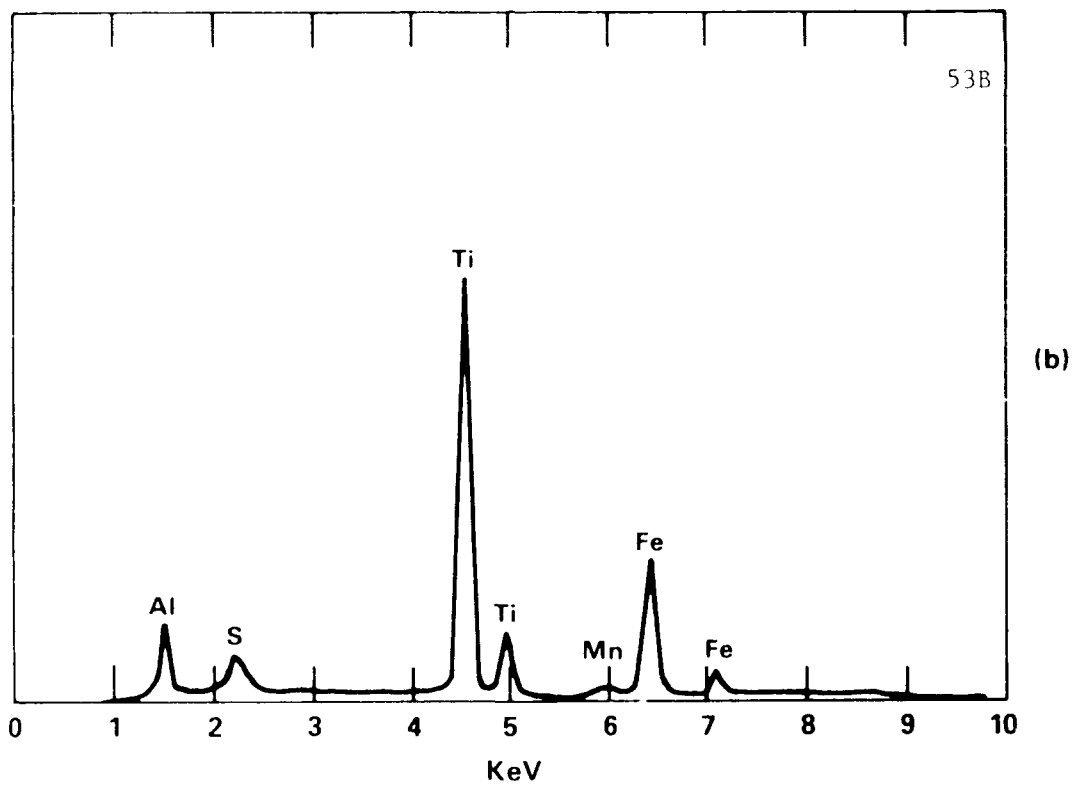
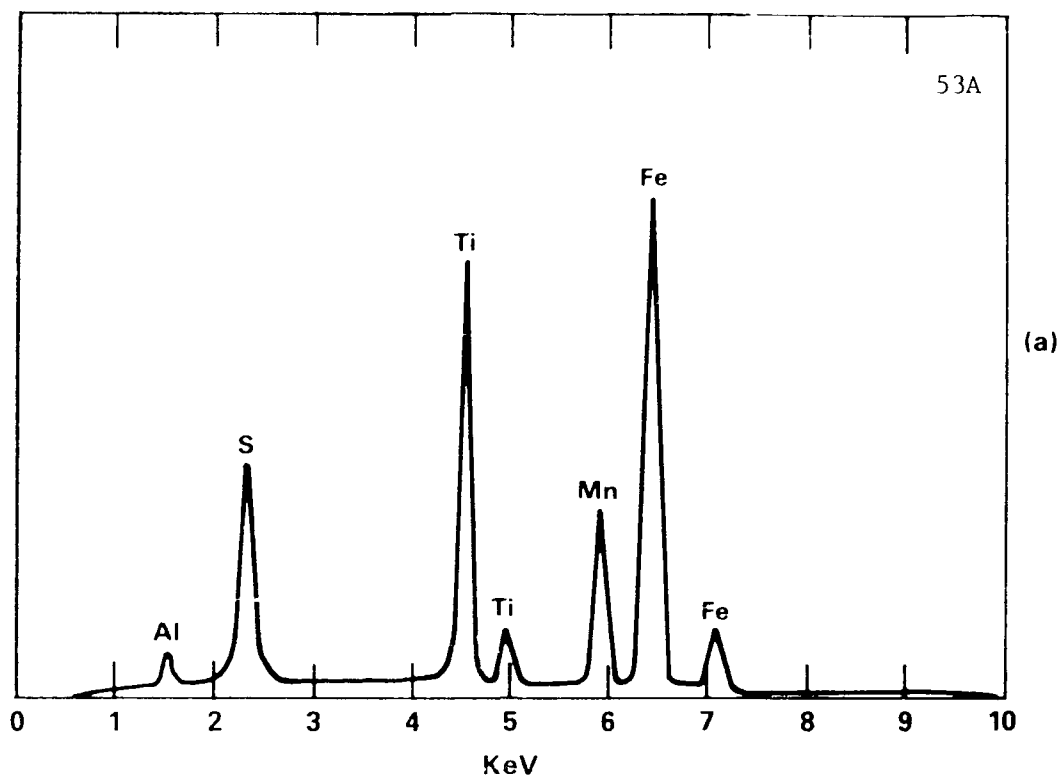Fig. 54.   EDS analysis of the inclusion shown in Fig. 53.
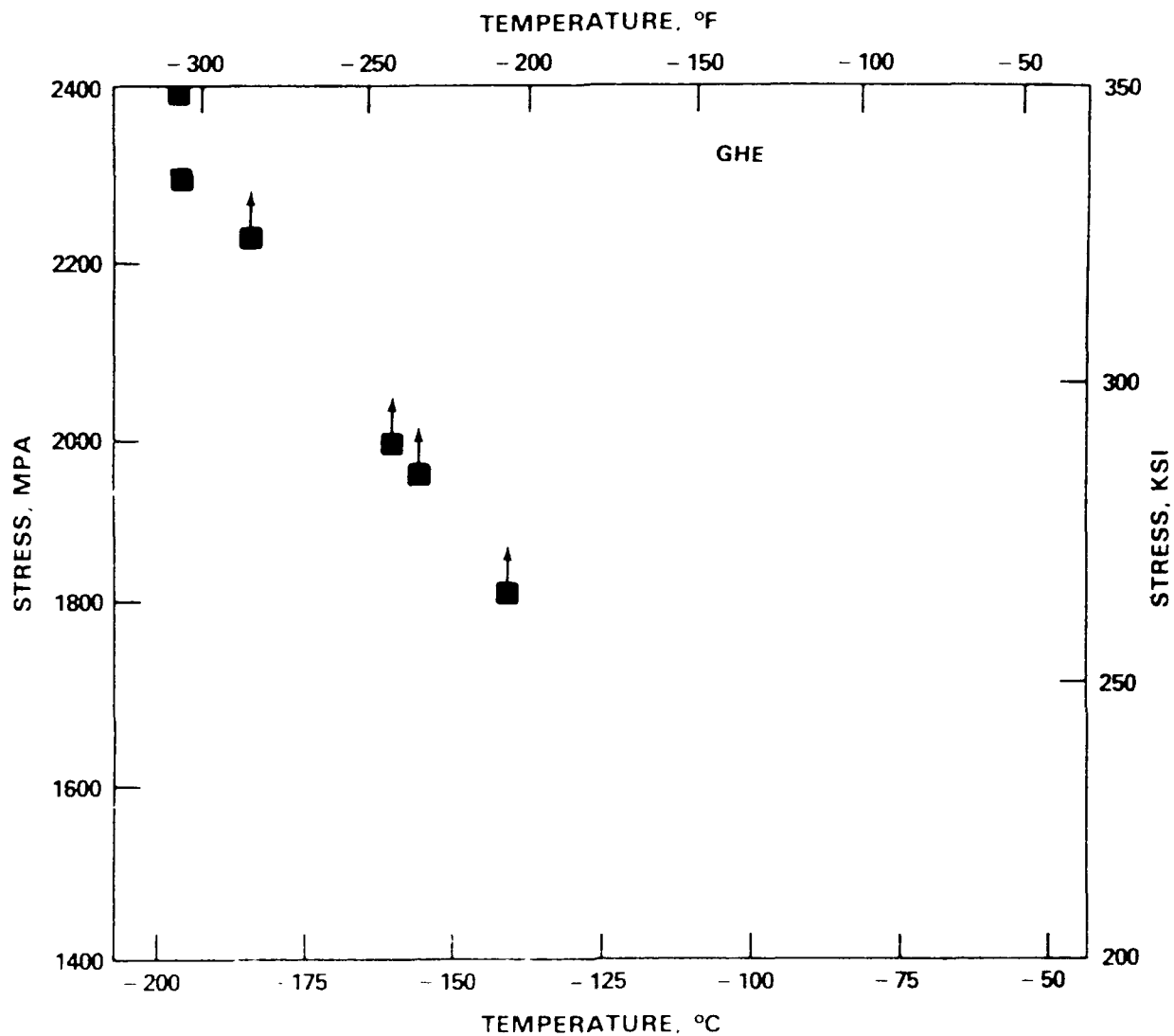
Fig. 55. Fracture stress results versus temperature for 1 Mn–1 Mo–1 Ni material GHE rolled at 1100°C.

Fig. 56.   Yield strength results versus temperature for 1 Mn–1 Mo–1 Ni material GHE rolled at 1100°C.
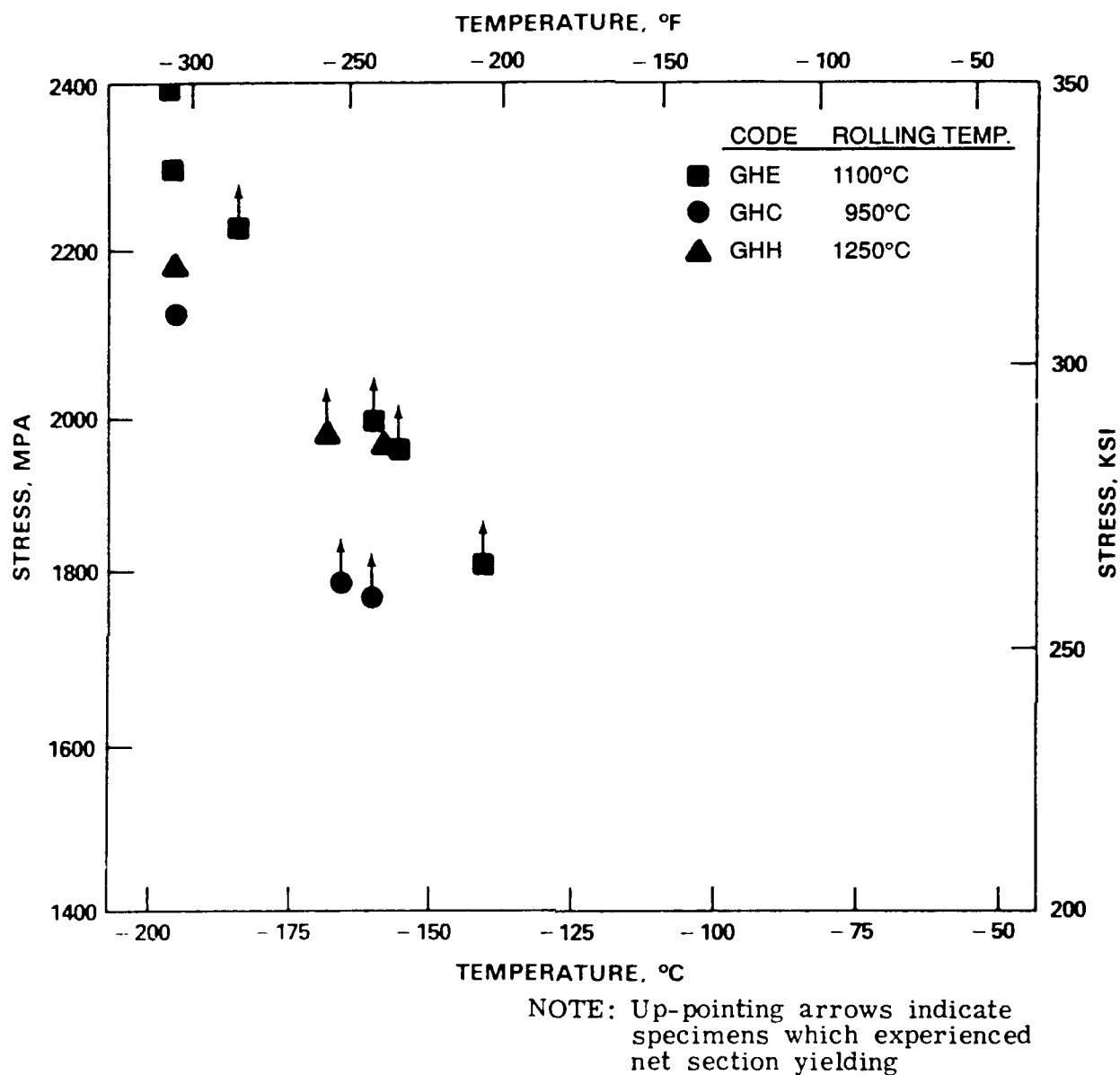
Fig. 57. Fracture stress results versus temperature for 1 Mn–1 Mo–1 Ni materials GHE, GHC, and GHH.
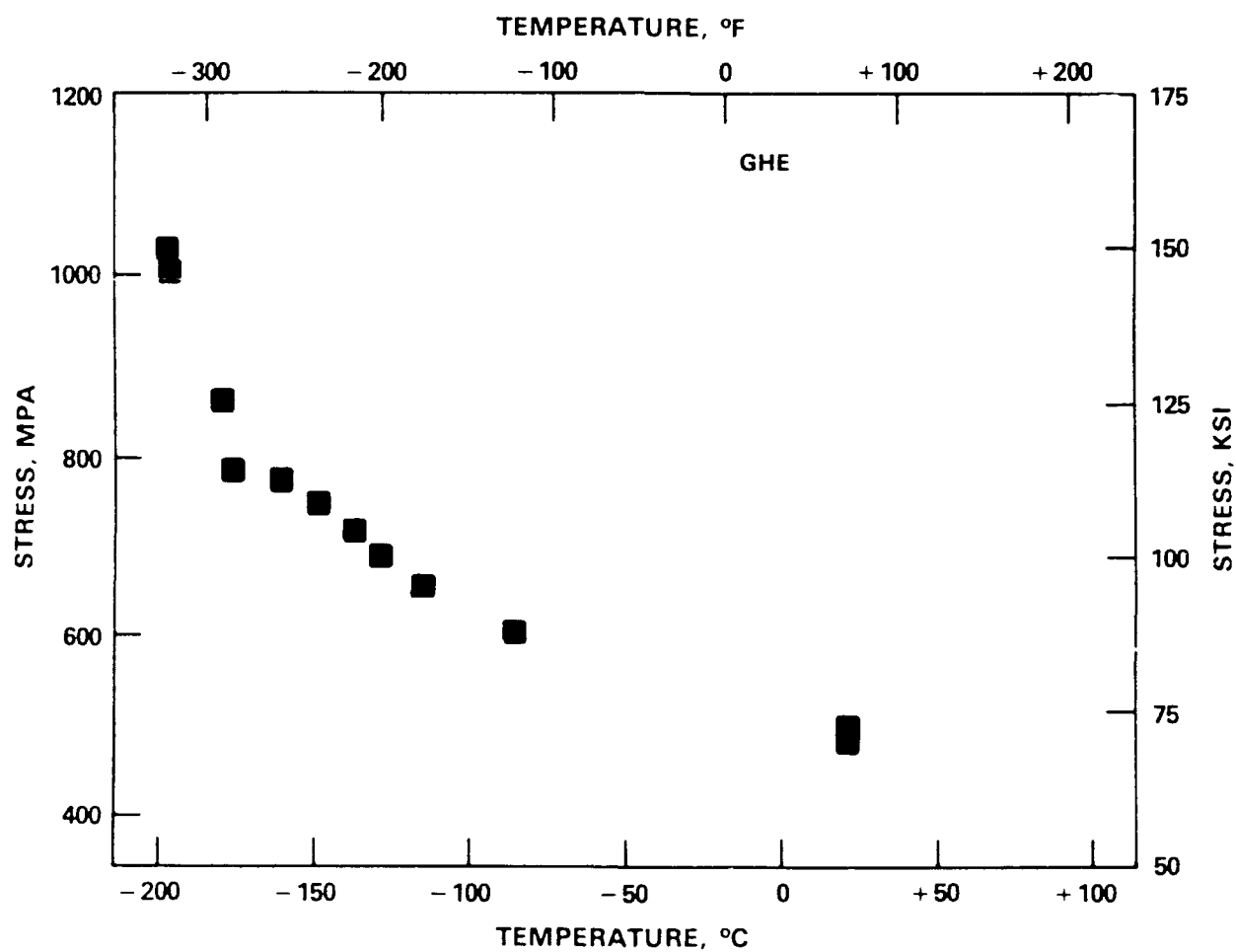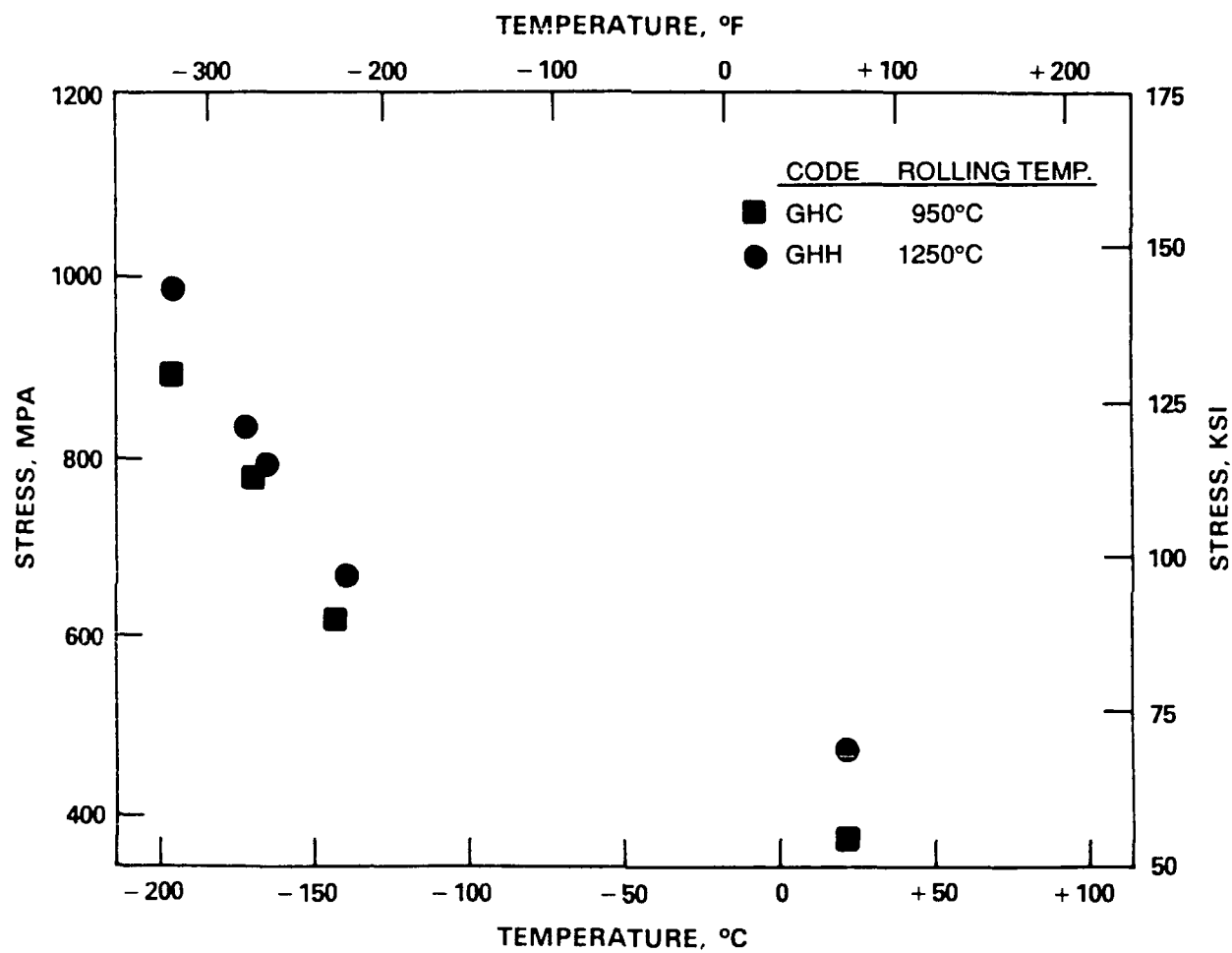
NOTE: Up-pointing arrows indicate
specimens which experienced
net section yielding

Fig. 58.   Yield strength results versus temperature for 1 Mn–1 Mo–1 Ni material GHC and GHH.

TEMPERATURE, °F

- 300   - 250   - 200   - 150   - 100   - 50

2400 ─   ─ 350

CODE   ROLLING TEMP.

▼ GHG   1250°C
▲ GHD   1100°C
■ GHE   1100°C
● GHB   950°C

2200 ─   ─ 300

STRESS, MPA

2000 ─

1800 ─

1600 ─   ─ 250

1400 ─   ─ 200

- 200   - 175   - 150   - 125   - 100   - 75   - 50

TEMPERATURE, °C

STRESS, KSI

NOTE: Up-pointing arrows indicate
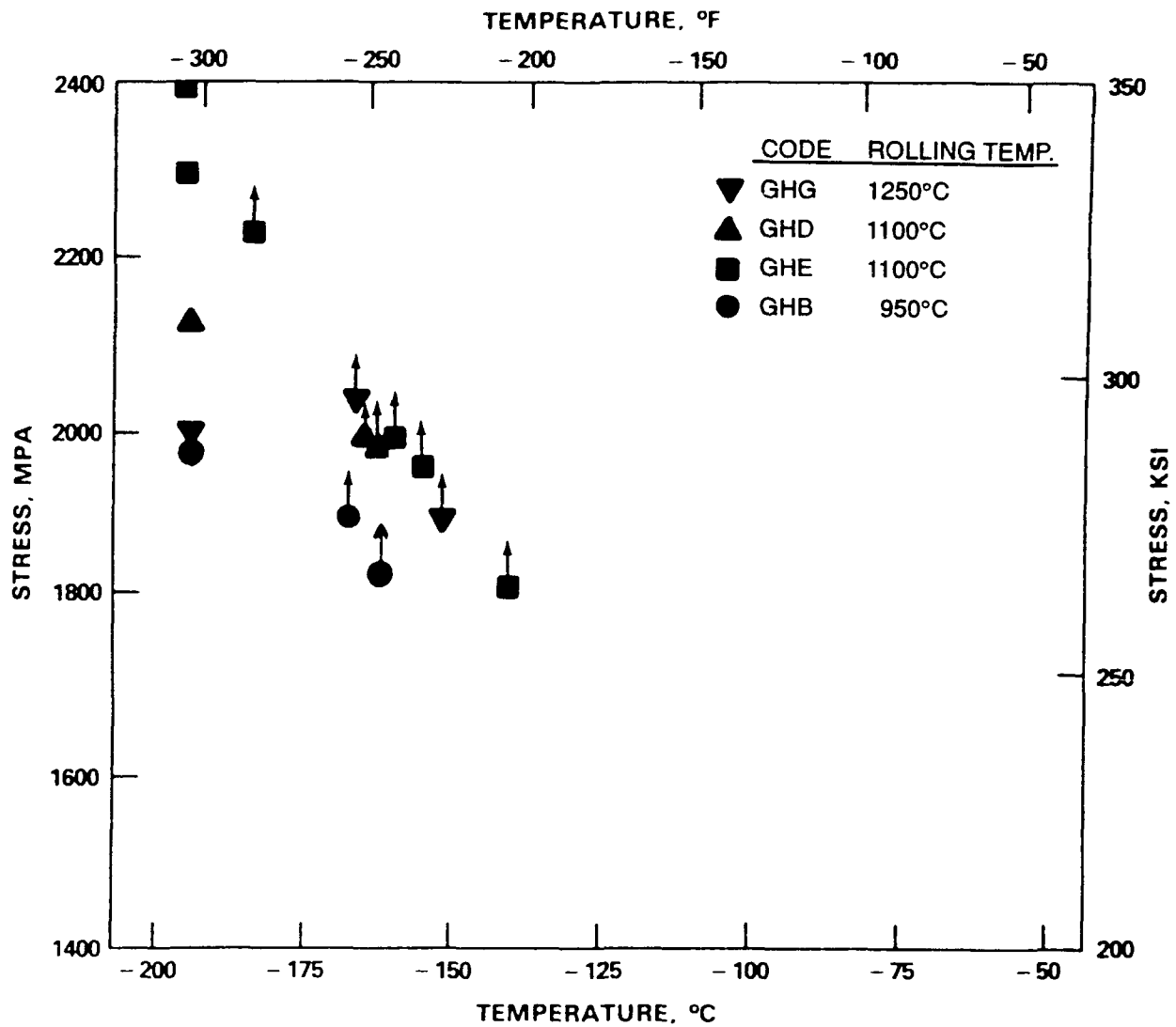specimens which experienced
net section yielding

Fig. 59.   Fracture stress measurements for materials GHE, GHB, GHD, and GHG.
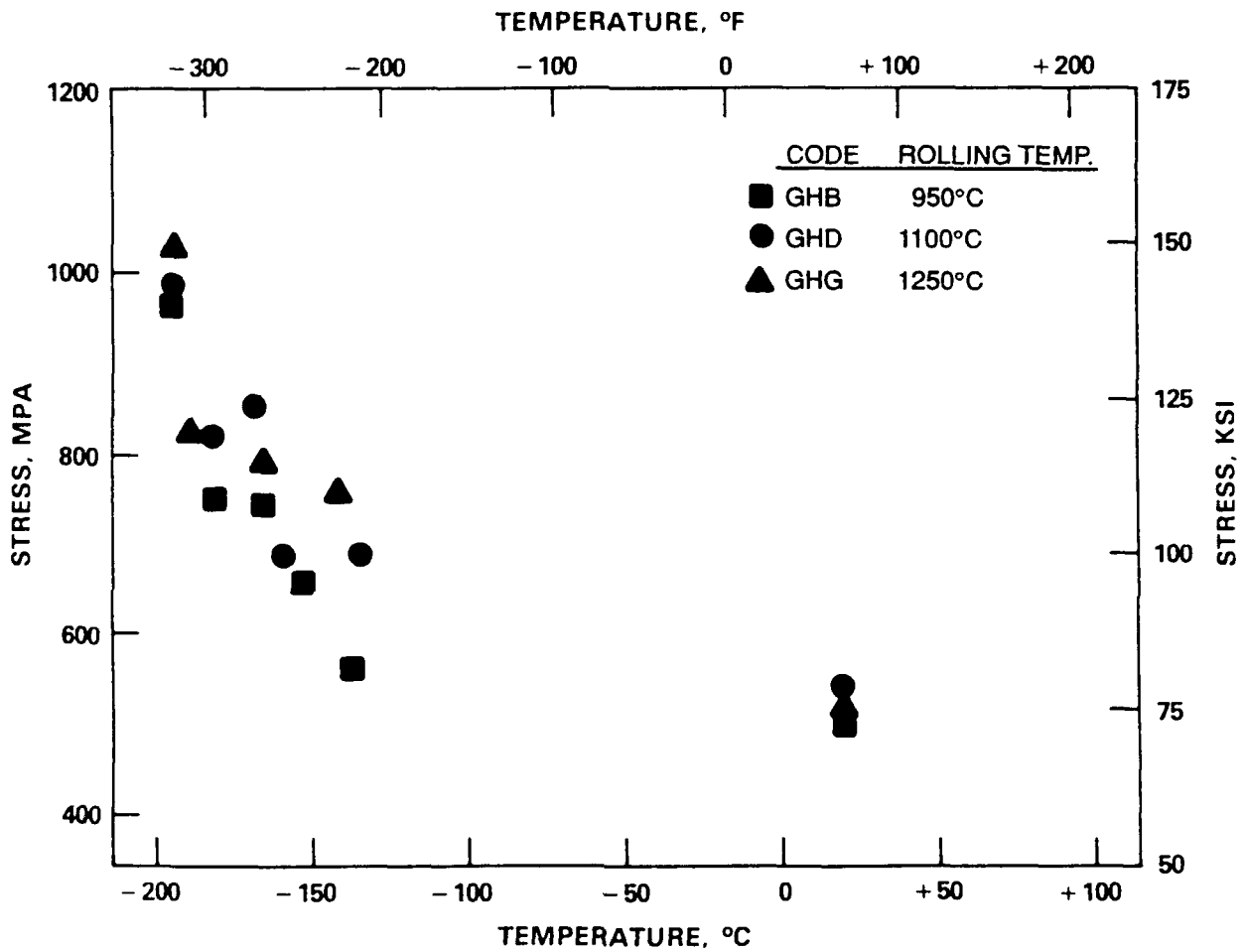
Fig. 60.   Yield strength versus temperature for 1 Mn–0.5 Mo–0.5 Ni material GHB, GHD, and GHG.

Fig. 61.   Charpy impact energy versus temperature for 1 Mn–1 Mo–1 Ni materials GHE, GHC, and GHH.
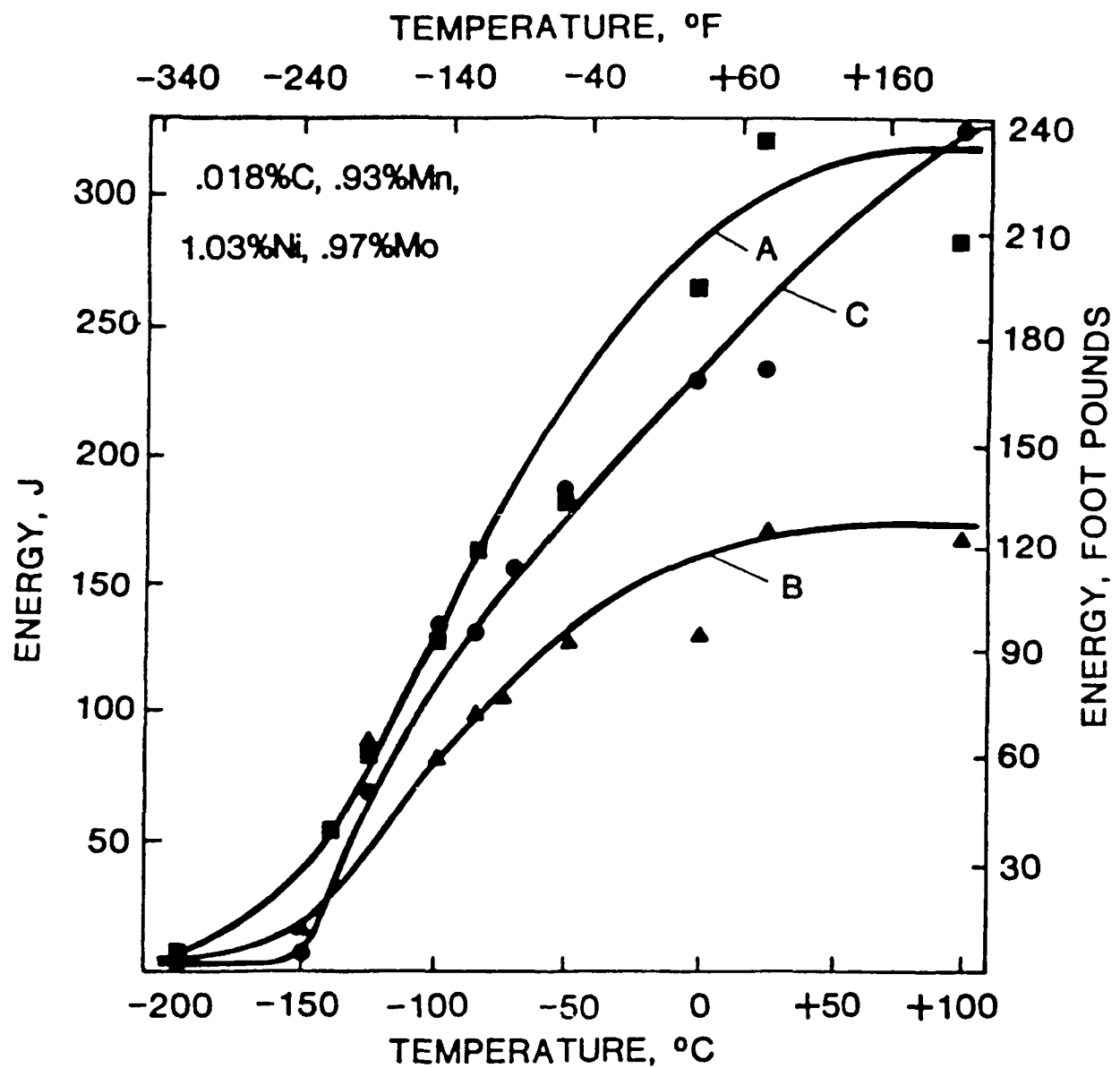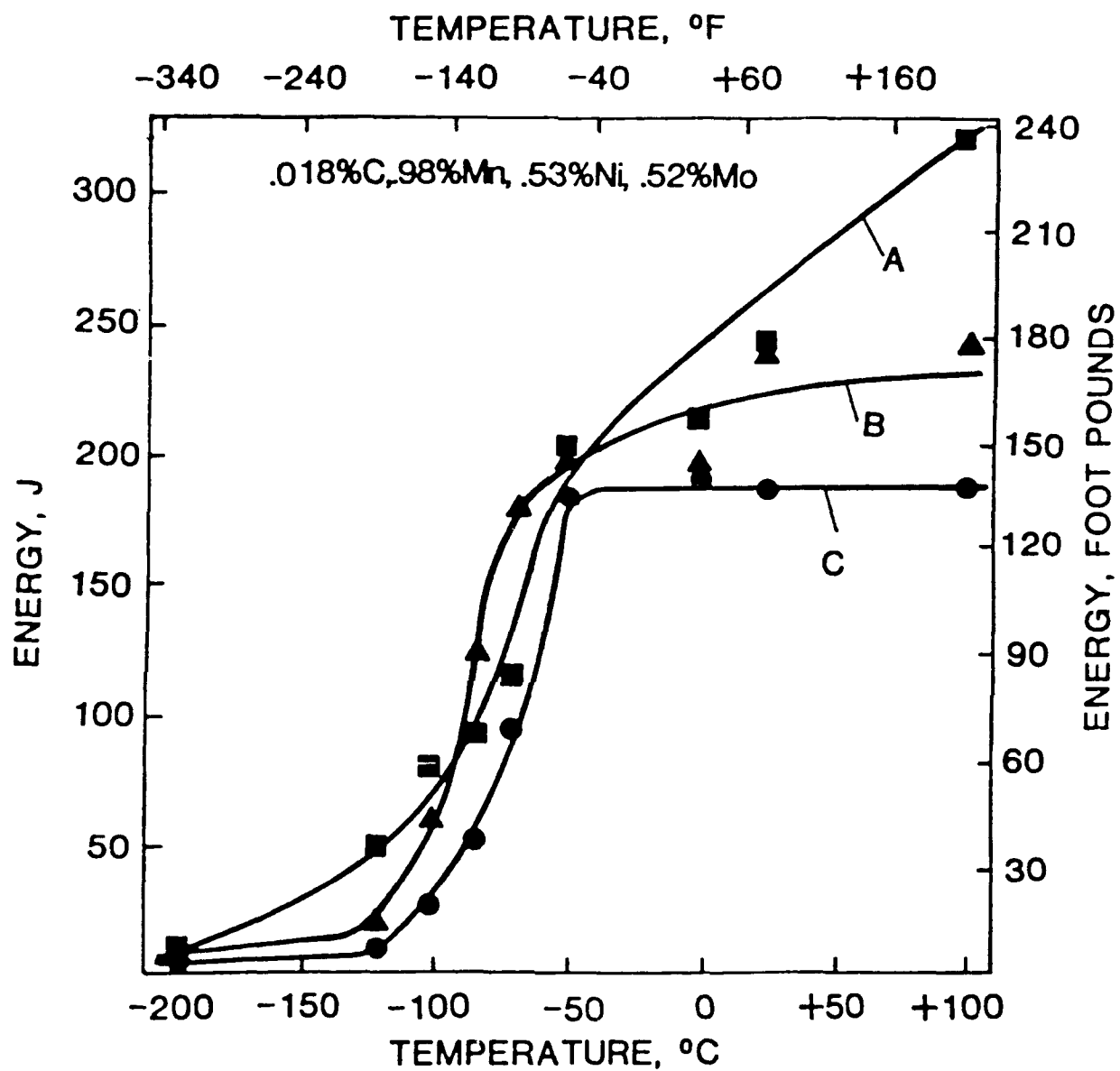A = GHC rolled at 950°C, B = GHE rolled at 1100°C, C = GHH rolled at 1250°C

Fig. 62.   Charpy impact energy versus temperature for 1 Mn–.5 Mo–.5 Ni materials GHB, GHD, and GHG.
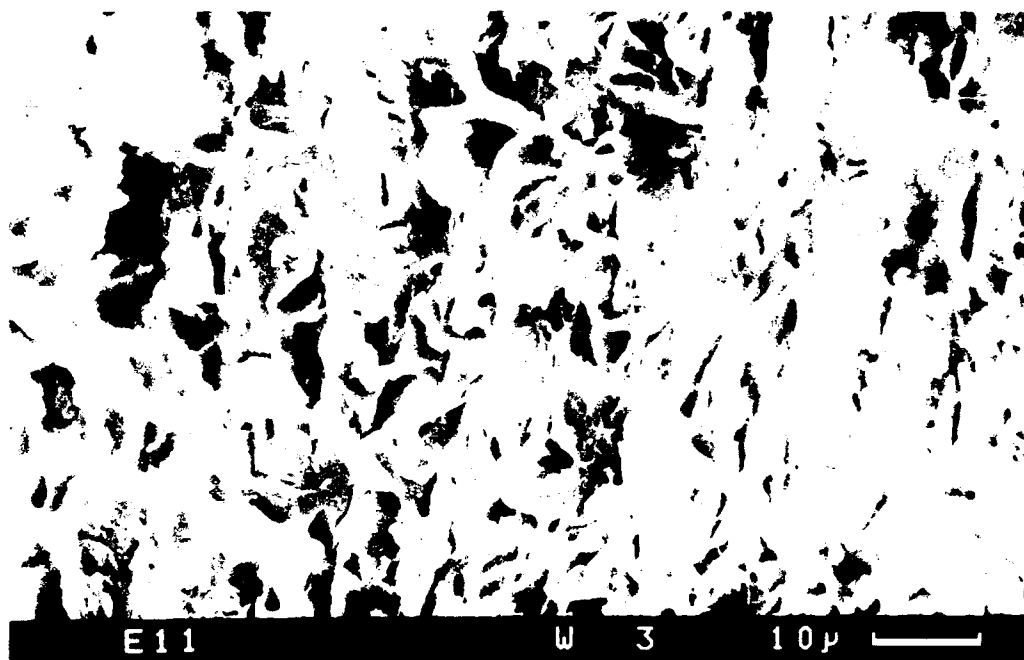A = GHB rolled at 950°C, B = GHD rolled at 1100°C, C = GHG rolled at 1250°C

Fig. 63. SEM photograph of the fracture surface of 1 Mn–1 Mo–1 Ni material GHE.

REFERENCES

1. Parker, E.R., Brittle Behavior of Engineering Structures, Hohn Wiley and Sons Inc., (1957).

2. Heller, S.R., Jr., et al., Naval Engineers Journal, Vol. 77, pp. 29–44 (1965).

3. Linnert, G.E., Welding Metallurgy, American Welding Society, Vol 1 (1965).

4. Welding Handbook, Section 4, American Welding Society, pp. 63–23 (1972).

5. Montemarano, T.W., et al., presented to Soc. of Naval Architecture and Marine Eng. (Chesapeake Chapter) (Sep 1984).

6. Hydrean, P.P., et al., Metall. Trans., Vol.2, 1971, pp. 2541–2548.

7. Irvine, K.J. and F.B. Pickering, Physical Properties of Martens e and Bainite, Iron, and Steel Institute, Report 193, London, pp. 110–125 (1965).

8. Irani, J.J. and G. Tither, Strong Tough Structural Steels, BISRA and IDI, pp. 135–14 (1967).

9. Irvine, K.J. and F.B. Pickering, Journal of the Iron and Steel Institute, Vol. 201, pp. 518–531 (1962).

10. McEvily, A.J., et al., Transformations and Hardenability in Steels, Climax Molybdenum Corp., pp. 179–191 (1967).

11. McEvily, A.J., and C.L. Magee, Low Alloy Steels, Iron and Steel Institute, London, pp. 111–117 (1968).

12. Gensamer, M. Trans. Metall. Soc. AIME, Vol. 215, pp. 2–8 (Feb 1959).

13. Jolley, W., Trans. Metall. Soc. AIME, Vol. 242, pp. 306–314 (Feb 1968).

14. Leslie, W.C., et al. Trans. ASM, Vol. 62, pp. 690–710 (1969).

15. Nostrom, L.A. and Vingsbo, O., Metals Science, Vol. 13, pp. 677–684 (Dec 1979).

16. Floreen, S., et al., Metallurgical Transactions, Vol. 2, pp. 1403–1406 (May 1971).

17. Hilderbrandt, U. and W. Dickernscheid, Acta Metall. Soc. AIME, Vol. 19, No. 1, pp. 49–55 (Jan 1971).

18. Graville, B.A., Welding of HSLA (Microalloyed) Structural Steels, ASM, pp. 85–99 (1978).

19. Coldren, A.R., R.L. Cryderman, and M. Semchyshen, Steel–Strengthening Mechanisms, Climax Molybdenum Corp., pp. 17–44 (1969).

20. Smith, Y.E., A.P. Coldren, and R.L. Cryderman, Towards Improved Ductility and Toughness, Climax Molybdenum Development Co., Ltd., pp. 119–142 (1971).

21. Bliss, V. and R.L. Cryderman, Metallurgical Transaction, Vol. 2, pp. 2267–2276. (Aug. 1971).

22. Josefsson, A., Journal of Metals, Trans. AIME, May pp. 652–659 (1954).

23. Allen, N.P., et al., Journal of the Iron and Steel Institute, Vol. 174, pp. 108–120 (Jun 1956).

24. Reinbolt, J.A. and W.J. Harris Jr., Transactions of the ASM, Vol. 43, pp. 1175–1201 (1951).

25. Roberts, M.J., Metallurgical Transactions, Vol. 1, pp. 3287–3294. (1979).

26. Helsop, J. and N.J. Petch, Phil. Mag., Vol. 3, pp. 1128 (1958).

27. Petch, N.J., Fracture, Wiley, New York, p. 54 (1959).

28. Low, J.R., Jr., Relation of Properties to Microstructure, ASM, Metals Park Ohio, p. 173 (1954).

29. Lesile, McCutcheon, D.B., et al., Revue de Metallurgie, J. pp. 143–174 (Feb 1976).

30. Tanaka, J., et al., Trans. of the Iron and Steel Institute of Japan, Vol. 15, pp. 19–26 (1975).

31. Lander, H.N., et al., Steel for Line Pipe and Pipeline Fittings, Metals Society, London, paper No. 14 (1983).

32. Nakasugi, H., et al., Alloys for the 80's, Climax Moly. Corp., pp. 213–224 (1980).

33. Nakasugi, H., et al., Steel for Line Pipe and Pipeline Fittings, Metals Society, London, pp. 90–99 (1983).

34. Orowan, E., Transactions of the Institute of Engineers and Shipbuilders in Scotland, Vo. 89, p. 165 (1945).

35. Griffith, A.A., Phil. Trans. Royal Society, A221, p. 163 (1920).

36. Irwin, G.R, Transactions of the American Society of Mechanical Engineers, Journal of Applied Mechanics, Vol. 24, p. 24 (1957).

37. Irwin, G.R, et al., Proceedings of the American Society of Testing and Materials, Vol. 58, p. 165 (1958).

38. Westergaard, H.M., Journal of Applied Mechanics, Vol. A, p. 49 (1939).

39. Knott, J.F. and Cottrell, A.H., Journal of the Iron and Steel Institute, Vol. 201, p. 249 (1963).

40. Hill, R., Mathematical Theory of Plasticity, Claredon Press, p. 248 (1950).

41. Knott, J.F., Journal of the Iron and Steel Institute, Vol. 205, p. 288 (1967).

42. Knott, J.F., Fundamentals of Fracture Mechanics, Butterworth, London, p. 182 (1973).

43. Griffiths, J.R. and Owen, R.D.J., Journal of the Mechanics and Physics of Solids, Vol. 19, p. 419 (1971).

44. McMahon, C.J. and Cohen, M., Acta Met., Vol. 13, p. 591 (1965).

45. Low, J.R., Jr., Symposium on the Relation of Properties to Microstructure, American Society for Metals, p. 163 (1954).

46. Smith, E., Proc. Conference Physical Basis of Yield and Fracture, Inst. Phys. Soc., Oxford, p. 36 (1966).

47. Ritchie, R.O., J.F. Knott, and J.R. Rice, Journal of the Mechanics and Physics of Solids, Vol. 21, p. 395 (1973).

48. Rice, J.R. and D.M. Tracy, Numerical and Computational Methods in Structural Mechanics, Academic Press, New York (1973).

49. Curry, D.A. and J.F. Knott, Metals Science, Vol. 10, pp. 1–6 (1976).

50. Curry, D.A. and J.F. Knott, Metals Science, Vol. 12, pp. 511–514 (1978).

51. Curry, D.A. and J.F. Knott, Metals Science, Vol. 13, pp. 341–345 (1979).

52. Tweed, J.H. and J.F. Knott, Proc. 5 th International Congress on Fracture, EMAS, p. 12 (1982).

53. Tweed, J.H. and J.F. Knott, Metals Science, Vol. 17, pp. 45–54 (1983).

54. McRobie, D.E. and J.F. Knott, Materials Science and Technology, Vol. 1, pp. 357–365 (1985).

55. Bliss, V. and R.L. Cryderman, Metall. Trans., Vol. V2, pp. 2267–2276 (1971).

56. Evensen, J.D., et al., TMS AIME, pp. 187–215 (1978).

57. Brozzo, P., et al., Metal Science, Vol. 11, pp. 123–129.

58. Baldi, G., and Buzzichelli, G., Metal Science, Vol. 12, pp. 459–471. (1978).

59. Houghton, D.C. et al., Thermomechanical Processing of Microalloyed Austenite, TMS–AiME, pp. 267–292 (1982).

60. Kanaznwa, S., Transactions of the Iron and Steel Institute of Japan, Vol. 16, pp. 486–495 (1976).

61. Oates, G., Journal of the Iron and Steel Institute, pp. 353–357 (1969).

62. Hendereckson, J.A., Transactions of the ASM, Vol. 50, pp. 656–681 (1958).

63. Speich, G.R., Trans. Metall. Soc. AIME., Vol. 245, pp. 2553–2564 (1969)

64. Marrison, T., Effect of Second–Phase Particles on the Mechanical Properties of Steel. ISI Publication 145, pp. 166–170 (1971).

65. McLean, A., and D.A.R. Kay, Microalloying 75, Union Carbide Corp., pp. 215–230 (1977).

66. Floreen, S., et al., Metallurgical Transactions, Vol. 2, , pp. 1403– 1406 (1971).

67. Brooksbank, D., and K.W. Andrews, Journal of Iron and Steel Institute, pp. 474–483 (1969).

REPORT DOCUMENTATION PAGE

Form Approved
OMB No 0704-0188

1. AGENCY USE ONLY (Leave blank)	2. REPORT DATE December 1990	3. REPORT TYPE AND DATES COVERED

4 TITLE AND SUBTITLE

Fracture Behavior of Ultra-Low-Carbone Steel Plate and Heat-Affected-Zone

5 FUNDING NUMBERS

6. AUTHOR(S)

M.G. Vassilaros

7. PERFORMING ORGANIZATION NAME(S) AND ADDRESS(ES)

David Taylor Research Center
Code 2814
Annapolis, MD 21402

8. PERFORMING ORGANIZATION REPORT NUMBER

DTRC-SME-90/39

9 SPONSORING / MONITORING AGENCY NAME(S) AND ADDRESS(ES)

Naval Sea Systems Command (SEA 05Z)

10. SPONSORING / MONITORING AGENCY REPORT NUMBER

11. SUPPLEMENTARY NOTES

12a. DISTRIBUTION / AVAILABILITY STATEMENT

Approved for public release; distribution is unlimited.

12b. DISTRIBUTION CODE

13 ABSTRACT (Maximum 200 words)

This report describes research carried out to investigate the fracture of ultra-low-carbon bainitic steels. Eight materials have been evaluated using notched-bar bend tests, tensile tests and Charpy V-notch impact tests, which were performed over a range of temperatures from −1965C to +1005C. These tests measured the cleavage fracture strength and the ductile-to-brittle transition temperature (DBTT) under impact loading. The materials evaluated had carbon levels of less than 0.03%, manganese level from 1% to 2%, and microalloys additions of niobium, titanium and boron. Some alloys also contained molybdenum and nickel. Some of the materials were subjected to simulated heat-affected-zone (HAZ) thermal cycle and other thermal-mechanical treatments. The fracture surfaces of the specimens were examined using the scanning electron microscope (SEM) and energy dispersive x-ray analysis. The results of the fracture tests and analyses indicate that the cleavage fracture strength of these materials can vary from 1650 to 2300 MPa. High cleavage fracture strength may be achieved with either a polygonal ferrite or an acicular/bainitic structure, but the high cleavage fracture strength of the polygonal ferrite structure material was reduced of a simulated thermal HAZ cycle.

14 SUBJECT TERMS

15. NUMBER OF PAGES

16. PRICE CODE

17. SECURITY CLASSIFICATION OF REPORT UNCLASSIFIED	18. SECURITY CLASSIFICATION OF THIS PAGE UNCLASSIFIED	19. SECURITY CLASSIFICATION OF ABSTRACT UNCLASSIFIED	20 LIMITATION OF ABSTRACT

NSN 7540-01-280-5500

Standard Form 298 (Rev. 2 89)
Prescribed by ANSI Std. Z39-18

END